
**Emergent states in
active fluids:
From bulk to confinement**

Inaugural-Dissertation

zur Erlangung des Doktorgrades
der Mathematisch-Naturwissenschaftlichen Fakultät
der Heinrich-Heine-Universität Düsseldorf

vorgelegt von

Andreas Kaiser

aus Köln

Düsseldorf, Dezember 2014

aus dem Institut für Theoretische Physik II: Weiche Materie
der Heinrich-Heine-Universität Düsseldorf

Gedruckt mit der Genehmigung der
Mathematisch-Naturwissenschaftlichen Fakultät der
Heinrich-Heine-Universität Düsseldorf

Referent: Prof. Dr. Hartmut Löwen
1. Korreferent: Prof. Dr. Jan Karel George Dhont
2. Korreferent: Prof. Dr. Christian Holm

Tag der mündlichen Prüfung: 12. Dezember 2014

Preface

This work has been developed during the last years (since May 2012) at the department for *Theoretical Physics II: Soft Matter* at the *Heinrich Heine University Düsseldorf*. Most results of this work have already been published in academic journals and the resulting publications are listed in the following. In addition, I give a statement about my personal contribution to every article to avoid plagiarism, because these publications have been written in cooperation with other scientists and departments. This thesis is based on the first four publications listed below and gives a selection of the main results of the projects where I have been mainly responsible.

List of published works

[1] Vortex arrays as emergent collective phenomena for circle swimmers

Andreas Kaiser and Hartmut Löwen, *Phys. Rev. E* **87**, 032712 (2013).

Abstract:

Collective properties of many rodlike circle swimmers are explored by computer simulations in two spatial dimensions. In the model considered, the center of mass of a single swimmer moves on a circle with radius R . Therefore, the model provides an interpolation between an interacting self-propelled-rod model for linear swimmers ($R \rightarrow \infty$) and that of interacting passive rotors ($R = 0$). We map out the state diagram for various swimmer densities and radii R . For increasing density, the dilute state is followed by vortices consisting of single particles (singlet-vortex state), where neighboring particles are perpendicularly oriented, and vortices of swimmer pairs (doublet-vortex state). The vortices exhibit strong structural ordering on an array. At higher densities, a slowed rotor fluid with a significant degree of mutual rotation hindrance occurs. The single-particle vortex structure becomes unstable above a threshold in the circling radius R , while pair vortices are stable only for intermediate radii R . A simple theory is proposed to predict the topology of the state diagram. Our results are verifiable for bacterial and artificial rodlike circle swimmers.

Statement of the author: This paper was written together with Hartmut Löwen who was involved in many discussions, while I performed the simulations and data analysis. It will be presented in Chapter 2.

[2] Capturing self-propelled particles in a moving microwedge

Andreas Kaiser, Katarina Popowa, Henricus H. Wensink, and Hartmut Löwen, Phys. Rev. E **88**, 022311 (2013).

Abstract:

Catching fish with a fishing net is typically done either by dragging a fishing net through quiescent water or by placing a stationary basket trap into a stream. We transfer these general concepts to micron-sized self-motile particles moving in a solvent at low Reynolds number and study their collective trapping behavior by means of computer simulations of a two-dimensional system of self-propelled rods. A chevron-shaped obstacle is dragged through the active suspension with a constant speed v and acts as a trapping “net”. Three trapping states can be identified corresponding to no trapping, partial trapping, and complete trapping and their relative stability is studied as a function of the apex angle of the wedge, the swimmer density and the drag speed v . When the net is dragged along the inner wedge, complete trapping is facilitated and a partially trapped state changes into a complete trapping state if the drag speed exceeds a certain value. Reversing the drag direction leads to a reentrant transition from no trapping to complete trapping and then back to no trapping upon increasing the drag speed along the outer wedge contour. The transition to complete trapping is marked by a templated self-assembly of rods forming polar smectic structures anchored onto the inner contour of the wedge. Our predictions can be verified in experiments of artificial or microbial swimmers confined in microfluidic trapping devices.

Statement of the author: This paper is the result of the work of Katarina Popowa and myself. In her Bachelor thesis, which I supervised, Katarina performed simulations to analyse the trapping efficiency of multiple particles in a moving trap. Her findings align with my simulation and theoretical prediction of the single particle case. Henricus H. Wensink contributed the basic source code, while Hartmut Löwen once again provided valuable input, especially concerning the theoretical predictions. Chapter 3 will deal with this work.

[3] Transport powered by bacterial turbulence

Andreas Kaiser, Anton Peshkov, Andrey Sokolov, Borge ten Hagen, Hartmut Löwen, and Igor S. Aranson, Phys. Rev. Lett. **112**, 158101 (2014).

Abstract:

We demonstrate that collective turbulentlike motion in a bacterial bath can power and steer the directed transport of mesoscopic carriers through the suspension. In our experiments and simulations, a microwedgelike “bulldozer” draws energy from a bacterial bath of varied density. We obtain that an optimal transport speed is achieved in the turbulent state of the bacterial suspension. This apparent rectification of random motion of bacteria is caused by polar ordered bacteria inside the cusp region of the carrier, which is shielded from the outside turbulent fluctuations.

Statement of the author: This paper is the result of a collaboration with experimental physicists from Chicago. While all experiments were performed by Anton Peshkov, Andrey Sokolov evaluated the respective data. Numerical results are based on my work. Borge ten Hagen was part of several helpful discussions on this matter. He also calculated the friction coefficients for the wedgelike carrier. Hartmut Löwen helped to initiate this collaboration, providing both supervision and guidance through many discussions. Igor S. Aranson was the initiator of the cooperation and was included in several discussions to merge experimental and numerical results. The according results will be shown in Chapter 4.

[4] Unusual swelling of a polymer in a bacterial bath

Andreas Kaiser and Hartmut Löwen, *J. Chem. Phys.* **141**, 044903 (2014).

Abstract:

The equilibrium structure and dynamics of a single polymer chain in a thermal solvent is by now well-understood in terms of scaling laws. Here, we consider a polymer in a bacterial bath, i.e. in a solvent consisting of active particles which bring in nonequilibrium fluctuations. Using computer simulations of a self-avoiding polymer chain in two dimensions which is exposed to a dilute bath of active particles, we show that the Flory-scaling exponent is unaffected by the bath activity provided the chain is very long. Conversely, for shorter chains, there is a nontrivial coupling between the bacteria intruding into the chain which may stiffen and expand the chain in a nonuniversal way. As a function of the molecular weight, the swelling first scales faster than described by the Flory exponent, then an unusual plateau-like behavior is reached and finally a crossover to the universal Flory behavior is observed. As a function of bacterial activity, the chain end-to-end distance exhibits a pronounced non-monotonicity. Moreover, the mean-square displacement of the center of mass of the chain shows a ballistic behavior at intermediate times as induced by the active solvent. Our predictions are verifiable in two-dimensional bacterial suspensions and for colloidal model chains exposed to artificial colloidal microswimmers.

Statement of the author: This paper was co-authored with Hartmut Löwen. The resulting findings are based on my simulations, and will be presented in Chapter 5.

[5] How to Capture Active Particles

Andreas Kaiser, Henricus H. Wensink, and Hartmut Löwen, Phys. Rev. Lett. **108**, 268307 (2012).

Abstract:

In many applications, it is important to catch collections of autonomously navigating microbes and man-made microswimmers in a controlled way. Using computer simulation of a two-dimensional system of self-propelled rods we show that a static chevron-shaped wall represents an excellent trapping device for self-motile particles. Its catching efficiency can be controlled by varying the apex angle of the trap which defines the sharpness of the cusp. Upon decreasing the angle we find a sequence of three emergent states: no trapping at wide angles followed by a sharp transition towards complete trapping at medium angles and a crossover to partial trapping at small cusp angles. A generic trapping “phase diagram” maps out the conditions at which the capture of active particles at a given density is rendered optimal.

Statement of the author: This paper includes the most important results of my Master thesis, which was produced under the supervision of Henricus H. Wensink and Hartmut Löwen. All presented results are based on my simulations, which are based on a basic source code provided by Henricus H. Wensink.

[6] Non-Gaussian statistics for the motion of self-propelled Janus particles: experiment versus theory

Xu Zheng, Borge ten Hagen, Andreas Kaiser, Meiling Wu, Haihang Cui, Zhanhua Silber-Li, and Hartmut Löwen, Phys. Rev. E **88**, 032304 (2013).

Abstract:

Spherical Janus particles are one of the most prominent examples for active Brownian objects. Here, we study the diffusiophoretic motion of such microswimmers in experiment and in theory. Three stages are found: simple Brownian motion at short times, superdiffusion at intermediate times, and finally diffusive behavior again at long times. These three regimes observed in the experiments are compared with a theoretical model for the Langevin dynamics of self-propelled particles with coupled translational and rotational motion. Besides the mean square displacement also higher displacement moments are addressed. In particular, theoretical predictions regarding the non-Gaussian behavior of self-propelled particles are verified in the experiments. Furthermore, the full displacement probability distribution is analyzed, where in agreement with Brownian dynamics simulations either an extremely broadened peak or a pronounced double-peak structure is found, depending on the experimental conditions.

Statement of the author: The paper has been written in collaboration with experimental groups from Beijing (Xu Zheng and Zhanhua Silber-Li) and Xi’an (Meiling Wu and Haihang Cui). I performed the simulations, while Borge ten Hagen was able to predict the experimental results

theoretically. Hartmut Löwen helped to merge theoretical and experimental results. The main results are briefly summarized in the Appendix.

[7] Differently Shaped Hard Body Colloids in Confinement: From passive to active particles

Henricus H. Wensink, Hartmut Löwen, Matthieu Marechal, Andreas Härtel, Raphael Wittkowski, Urs Zimmermann, Andreas Kaiser, and Andreas M. Menzel, *Eur. Phys. J. Special Topics* **222**, 3023 (2013).

Abstract:

We review recent progress in the theoretical description of anisotropic hard colloidal particles. The shapes considered range from rods and dumbbells to rounded cubes, polyhedra and to biaxial particles with arbitrary shape. Our focus is on both static and dynamical density functional theory and on computer simulations. We describe recent results for the structure, dynamics and phase behavior in the bulk and in various confining geometries, e.g. established by two parallel walls which reduce the dimensionality of the system to two dimensions. We also include recent theoretical modelling for active particles, which are autonomously driven by some intrinsic motor, and highlight their fascinating nonequilibrium dynamics and collective behavior.

Statement of the author: This review presents the results of the whole project D3 from the SFB TR6 ("Physics of Colloidal Dispersions in External Fields"), which have been published in the last four years. In this review my contribution are the results from [1, 2, 5].

[8] Mechanisms of carrier transport induced by a microswimmer bath

Andreas Kaiser, Andrey Sokolov, Igor S. Aranson and Hartmut Löwen, (*submitted to IEEE Transactions on Nanobioscience*).

Abstract:

Recently, it was found that a wedgelike microparticle (referred to as "carrier") which is only allowed to translate but not to rotate exhibits a directed translational motion along the wedge cusp if it is exposed to a bath of microswimmers. Here we model this effect in detail by resolving the microswimmers explicitly using interaction models with different degrees of mutual alignment. Using computer simulations we study the impact of these interactions on the transport efficiency of a V-shaped carrier. We show that the transport mechanisms itself strongly depends on the degree of alignment embodied in the modelling of the individual swimmer dynamics. For weak alignment, optimal carrier transport occurs in the turbulent microswimmer state and is induced by swirl depletion inside the carrier. For strong aligning interactions, optimal transport occurs already in the dilute regime and is mediated by a polar cloud of swimmers in the carrier wake pushing the wedge-particle forward. We also demonstrate that the optimal shape of the carrier leading to maximal transport speed depends on the kind of interaction model used.

Statement of the author: This work is an extension of Reference [3] and is based on my numerical results and the experimental data has been evaluated by Andrey Sokolov. Igor S. Aranson and Hartmut Löwen have been involved by many discussions and initiated the cooperation.

Abstract

This work is about *emergent states in active fluids*, meaning fluids consisting of self-propelled units. The collective behavior of such units with spherical and rodlike shape is investigated in bulk as well as in systems with confinements of various characteristics. These emerging states will be mainly analysed by Brownian dynamics simulations and the results can be applied to various domains of science: self-propelled particles can be manufactured synthetically (chemistry and even robotics) or are present in nature, e.g. in form of bacteria, fish, and birds, (biology) and the study of their statistical properties and collective behavior has emerged as a popular topic in physics over the past years.

Chapter 1 provides an introduction to active fluids. An explanation why the particles within these fluids objects are called “active” will be given alongside examples for living and artificial colloidal active particles. Furthermore, the theory behind the dynamics of these particles will be described, including a detailed explanation of the corresponding simulation routine and the particle model employed throughout this thesis. Moreover, a brief summary on statistical properties of polymers in equilibrium will be given.

Chapter 2 considers self-propelled particles propagating on circular paths in bulk. Collective properties of such circle swimmers will be investigated and a state diagram will be mapped out for varying particle density and swimming path radii. The four emerging distinctive states will be quantified by suitable order parameters. A simple theory will be proposed to predict the found state diagram.

Beginning with Chapter 3 we will include an obstacle in the considered system of active particles. From there on out, we will study active particles which propagate on straight lines. For such particles a stiff wedgelike obstacle represents an excellent trapping device and its efficiency can be controlled by varying the apex angle. Adopting an established technique from the fishing industry, the wedge will be dragged through the system of colloidal microswimmers. The collective trapping regimes will be investigated as well as the probability of trapping a single swimmer in relation to the apex angle and the dragging velocity. For the single swimmer case a theoretical prediction will be given, which will explain an unexpected reentrant effect in the trapping state diagram for both cases.

Chapter 4 will show the possibility of extracting directed motion, in other words useable kinetic energy, out of a bacterial bath. Here a carrier (a wedgelike object) is submersed in active fluids of varied bacterial concentrations. The transport efficiency will be studied in experiments on living bacteria and compared to numerical results. As the explanation for the directed motion of the carrier, the concept of swirl shielding will be introduced. This will clarify why the transport velocity is maximal in a state which is known as bacterial turbulence.

A deformable obstacle is considered in Chapter 5. It will be modeled as a semiflexible chain (like a polymer) and its statistical properties will be analysed for the case that it is submersed in a bacterial bath and compared to the well known case of the exposure to a thermal bath. Therefore, the length of the chain as well as the density and the activity of the active fluid will

be varied. While the static properties for long chains are unaffected, there is a faster swelling of the polymer than described by the Flory exponent for short chains.

Chapter 6 provides a conclusion and gives an outlook on problems that remain unanswered and need to be addressed in the future.

In the Appendix the statistical properties of the motion of an active particle will be briefly summarized with respect to the mean square displacement and even higher displacement moments. Theoretical predictions, based on the used model in this thesis, are confirmed by experiments with artificial microswimmers.

Zusammenfassung

In dieser Arbeit über *auf tretende Zustände in aktiven Flüssigkeiten* werden die kollektiven Verhalten von sowohl kugel- als auch stäbchenförmigen selbstgetriebenen Teilchen in Systemen ohne sowie mit unterschiedlichen Hindernissen untersucht. Dies geschieht hauptsächlich aufgrund von Computersimulationen der Brownschen Dynamik. Die erzielten Ergebnisse sind für verschiedene Disziplinen der Naturwissenschaften relevant: Selbstgetriebene Teilchen können einerseits synthetisch hergestellt werden, wodurch die Chemie und die Robotik einbezogen werden. Andererseits sind aber auch in der Natur (Biologie) aktive Teilchen zu finden – Beispiele sind unter anderem Bakterien, Fische und Vögel. Darüber hinaus ist die Analyse der statistischen Eigenschaften der oben genannten Systeme sowie die Beschreibung der auftretenden kollektiven Verhalten in den letzten Jahren ein verbreiteter Forschungsbereich in der Physik geworden.

Zu Beginn wird in Kapitel 1 eine Einleitung zu aktiven Flüssigkeiten gegeben. Beispiele hierfür werden genauer beschrieben und es wird erklärt, warum man die Objekte, die von einer solche Flüssigkeiten beinhaltet werden, „aktiv“ genannt werden. Außerdem werden die grundlegende Simulationsmethodik und das genutzte Teilchenmodell detailliert beschrieben. Abschließend wird eine kurze Einführung in die Polymerphysik gegeben.

Kapitel 2 befasst sich mit selbstgetriebenen Teilchen („Schwimmern“) die sich auf kreisförmigen Trajektorien bewegen. Ihr kollektives Verhalten wird untersucht und ein Diagramm ausgearbeitet, das die auftretenden Strukturen zeigt. Hierbei werden sowohl die Teilchendichte als auch der Radius der Teilchentrajektorien variiert. Die vier auftretenden Strukturen werden dabei durch geeignete Ordnungsparameter charakterisiert. Basierend auf geometrischen Überlegungen, wird eine einfache Theorie vorgestellt, mit der sich das gefundene Diagramm qualitativ vorhersagen lassen kann.

Ab Kapitel 3 werden aktive Flüssigkeiten analysiert denen ein Hindernis hinzugefügt wird. Außerdem werden von nun an selbstgetriebene Teilchen betrachtet, die sich auf geraden und nicht mehr gekrümmten Bahnen fortbewegen. Ein steifer statischer Keil repräsentiert eine ausgezeichnete Vorrichtung um solche aktiven Teilchen einzufangen. Die Effizienz dieser Falle lässt sich durch den Öffnungswinkel des Keils kontrollieren. Beim industriellen Fischfang werden Netze durch Flüsse, Seen und Meere gezogen. Diese Idee soll nun aufgegriffen werden um Teilchen auf mikroskopischer Größenskala einzufangen. Deswegen ziehen wir den festen Keil durch eine aktive Flüssigkeit und untersuchen sowohl die Fangstadien für viele aktive Teilchen als auch die Wahrscheinlichkeit einen einzelnen Schwimmer einzufangen. Dies hängt sowohl vom Öffnungswinkel des Keils wie auch der Zuggeschwindigkeit (und deren Richtung) ab. In Abhängigkeit der Zuggeschwindigkeit wird der kritische Öffnungswinkel, der noch ein Einfangen eines einzelnen Schwimmers ermöglicht, berechnet werden.

In Kapitel 4 wird gezeigt, dass es möglich ist eine gerichtete Bewegung und damit nutzbare kinetische Energie aus einem Bakterienbad zu extrahieren. Dafür wird ein Keil in ein solches Bad eingetaucht, welcher durch die Bakterien entlang der Keilachse transportiert wird. Die zugehörige durch Simulationen erhaltene Effizienz wird durch experimentelle Ergebnisse bestätigt. Die Erklärung für die gerichtete Bewegung des Keils beruht auf dem Konzept der

Wirbelabschirmung des Keils. Bakterien zeigen ein kollektives Verhalten, das als *bakterielle Turbulenz* bezeichnet wird. Diese Turbulenz ist dadurch charakterisiert, dass das Bad eine Vielzahl von Wirbeln aufzeigt, die in unterschiedliche Richtungen rotieren. Diese Wirbel liefern letztendlich die Erklärung, warum die erreichte Transporteffizienz im Bereich der bakteriellen Turbulenz am höchsten ist.

Als nächstes betrachten wir in Kapitel 5 ein deformierbares Hindernis in einer aktiven Flüssigkeit. Dieses Hindernis wird eine Kette sein und wie typischerweise ein Polymer als halbstarre Kette modelliert werden. Die statistischen Eigenschaften von Polymeren in einem thermalen Bad sind seit langem bekannt und werden nun hier verglichen mit dem Fall, dass ein solches Polymer einem bakteriellen Bad ausgesetzt ist. Dazu werden sowohl die Länge der Polymerkette wie auch die Konzentration und die Aktivität des Bades variiert werden. Hierbei ist signifikant, dass der End-zu-End-Abstand für kurze Ketten in einer aktiven Flüssigkeit schneller anwächst als im Falle eines thermalen Bades, in dem der Flory-Exponent gilt.

Abschließend werden alle Ergebnisse nochmals kurz zusammengefasst und ein Ausblick wird gegeben, welche unbeantworteten Fragen immer noch bleiben, die es in Zukunft jedoch zu beantworten gilt, siehe Kapitel 6.

Zusätzlich werden im Anhang die statistischen Eigenschaften der Bewegung von einzelnen aktiven Teilchen, ausgehend vom mittleren Verschiebungsquadrat und höheren Momenten, untersucht. Experimentelle Ergebnisse für künstliche Schwimmer zeigen, dass die verwendete theoretische Modellierung der Schwimmerbewegung, basierend auf den Langevin Gleichungen, in dieser Arbeit gerechtfertigt ist.

Contents

Preface	i
List of published works	i
Abstract	vii
Zusammenfassung	ix
1. Introduction	1
1.1. Active and passive particles	1
1.2. Living and synthetic active colloidal particles	1
1.3. Dynamics of active colloidal particles	5
1.4. The Yukawa segment model	8
1.5. Polymer physics	10
2. Vortex arrays as emergent collective phenomena for circle swimmers	15
2.1. Frictional dynamics of a self-propelled-rod model	17
2.2. Simulation results	19
2.3. Simple Theory	24
2.4. Conclusions	27
3. Capturing self-propelled particles in a moving microwedge	29
3.1. Model	31
3.2. Trapping a single swimmer in a mobile microwedge	33
3.3. Collective trapping	36
3.3.1. Static microwedge	36
3.3.2. Mobile microwedge	37
3.4. Conclusions	41
4. Transport powered by bacterial turbulence	45
4.1. Experiment	46
4.2. Model	48
4.3. Transport of a wedgelike carrier	49
4.4. Direction of transport	53
4.5. Conclusion	54
5. Unusual swelling of a polymer in a bacterial bath	57
5.1. Model	58
5.2. Results	61

5.3. Polymer dynamics	64
5.4. Conclusions	67
6. Conclusion	69
A. Appendix: Non-Gaussian statistics for the motion of self-propelled Janus particles: Experiment versus theory	73
Bibliography	80



Introduction

1.1. Active and passive particles

Every existing object can be classified as either *passive* or *active*. While the motion of passive particles is restricted to external forces and torques, active particles also move due to an internal propulsion mechanism. Consequently, non-living (dead) organisms as well as various synthetically produced materials are *passive* particles and most living organisms (independent of their size) can be categorized as *active*, e.g. birds [9], fish [10], insects like locusts [11] or ants [12], and human beings [13–15]. Furthermore, in recent years several realizations of artificial self-propelled particles have been established, see the recent review [16]. These man-made swimmers are based on various self-propulsion mechanisms and can be manufactured with arbitrary shapes.

1.2. Living and synthetic active colloidal particles

In this work we will concentrate on colloidal systems. Colloidal particles are small particles, in the range of 10^{-9} m – 10^{-6} m dispersed in another continuous medium like a liquid [17]. Therefore, in nature living colloidal particles are microorganisms such as bacteria, sperm and algae. Due to their small size and low velocity¹ colloidal microswimmers move in the low Reynolds number regime². The Reynolds number is defined by the relation of non-linear inertia forces and viscous forces [19]. Hence, small Reynolds numbers lead to a quasi inertia free and overdamped motion.

Let us start with the basic requirements for self-propulsion in the low Reynolds number regime established by body-deformations before we concentrate on actual self-propulsion mechanisms used by living and artificial microswimmers. Non-reciprocal periodic changes of the body shape of microswimmers are essential for a non-zero time averaged propulsion force (internally created) and a resulting drag-based (i.e. frictional based) propulsion. Here I want

¹Bacteria move with a high velocity compared to their own size. The propulsion velocity is up to ten times their body length per second, although the absolute value ($v \sim 20$ $\mu\text{m/s}$) is quite small [18].

²Typically the Reynolds number for swimming microorganisms is in the order of 10^{-4} while macroscopic living organisms it is in the range of 10^3 – 10^8 .

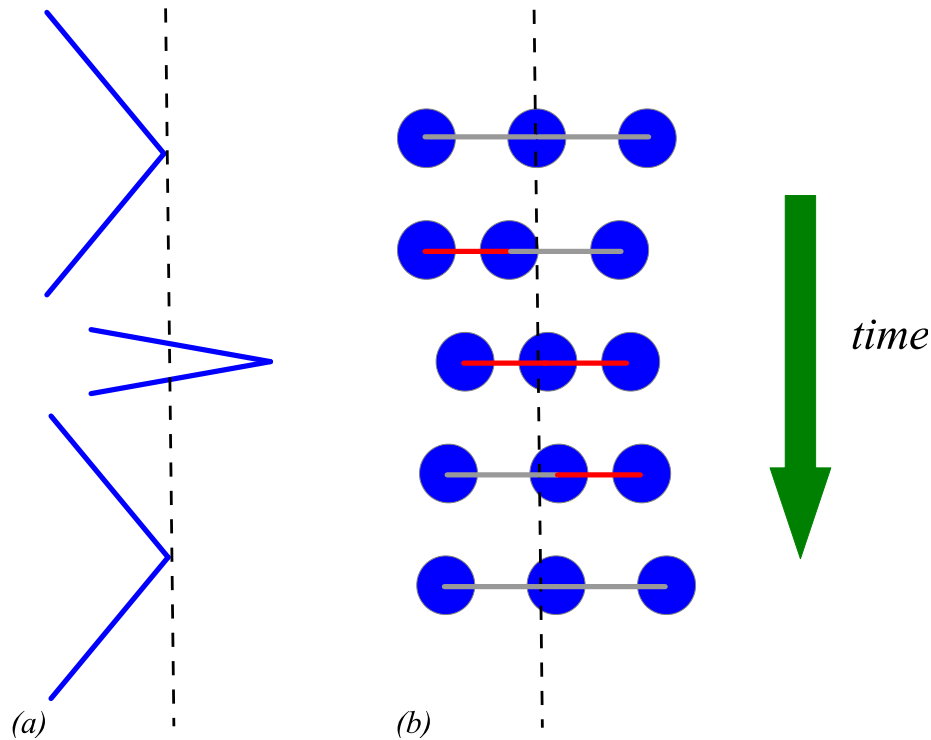


Figure 1.1.: *Representation of the scallop theorem. (a) While a scallop with a single hinge is not able to perform a total net propulsion after one cycle of body deformations, (b) a swimmer consisting of three linked spheres can achieve this. Compressed links are drawn in red. Vertical dashed lines are a guide to the eye to visualize the resulting displacement due to a sequence of body deformations. The time course is indicated by an arrow.*

to stress that these forces do not contradict the fact that a swimmer is force-free. The quasi inertia free motion in the low Reynolds number regime requires a force balance (actio = reactio). There are no external forces and torques acting on a microswimmer. Nevertheless they are able to perform a directed motion. Let us consider an active particle which is capable of creating a thrust force \mathbf{F} , e.g. by clever body deformations³, acting on the surrounding fluid and pushing the particle forward. This motion induces a force $-\mathbf{F}$ onto the fluid. Hence, the total force on a microswimmer is zero. In our modeling for the dynamics of microswimmers we will concentrate on the fact that a swimmer has a self-propulsion velocity, which can be related via friction to an effective self-propulsion force [20].

A necessary condition for such a net propulsion of a microswimmer after one cycle of body shape deformations is that the sequence of shapes during one of these cycles is different when viewed in a time-reversed way, which is then called a non-reciprocal sequence. This has been

³This will be specified in the following paragraph.

stated in the well known *scallop theorem* by Edward Purcell [21]. Here Purcell shows that a scallop, consisting out of two stiff rods connected by a hinge, cannot move just by changing its apex angle, since this motion is reciprocal, see Figure 1.1(a). If a scallop reduces the angle at its hinge, it is able to move forward. But due to the restriction to the low Reynolds number regime the scallop moves back to its original position when the angle increases again. At least two or more parametric deformations are necessary for a propulsion of a single particle [22–24]. The most famous simple microswimmer is the three sphere swimmer [25]. To achieve a directed propulsion three spheres are connected with two arms whose lengths are varied in a non-reciprocal way. The deformation cycle is composed of four consecutive time-reversal breaking stages, as shown in Figure 1.1(b). This swimmer can be treated theoretically much more easily than a simple Purcell swimmer with two hinges. For the three sphere swimmer, many properties can be analysed in detail or even calculated analytically [25–27].

Common living colloidal microswimmers, such as bacteria, sperm and algae use techniques other than deformation of the main body. All of the mentioned examples have thin flagella attached to their body⁴. A screwlike rotational motion of the flagella is used by bacteria as *Escherichia coli* and *Bacillus subtilis* [3, 18], which fulfills the scallop theorem mentioned above [28]. Sperm, however, perform a wavelike beating motion with their flagellum to propel themselves [29–33], see Figure 1.2. Obviously, a wavelike motion of the main body of a microorganisms leads to a directed self-propulsion, too [34].

All of these living microswimmers can be classified as *pushers* since they repel the surrounding fluid from the body along the long axis [28], commonly achieved by propelling flagella in the rear relative to the direction of propulsion (see again Figure 1.2). A *puller* draws fluid in along the elongated direction [28]. Usually, it has the flagella in front of the main body during the propulsion. Here *Chlamydomonas reinhardtii*, a biflagelled alga, is the best known representative [35, 36]. The two flagella beat synchronized in a “breast-stroke” pattern [33], see Figure 1.2.

Self-propulsion, induced by the motion of attached flagella or by rotation of a screwlike body has also been adopted for artificial microswimmers [37–39], but it is not the most common propulsion mechanism for such synthetic swimmers. The majority of these particles move by converting chemical energy into kinetic energy, see recent reviews [16, 40] as well as references herein and Figure 1.3.

The self-propulsion of most manmade swimmers is due to *self-phoresis*, where *phoresis* refers in general to an effective transport of colloidal particles due to boundary layer forces induced by external fields [41]. A drift experienced by a particle which is subject to a concentration gradient across its interface is known as diffusiophoresis [42–46]. Self-phoresis describes the phenomenon that the change in the environment – in this case the existence of a concentration gradient – is induced by the particle itself and not by any externally applied field. As a consequence, the ability to catalyze fuel substance on the particle surface in an asymmetric fashion will lead to a robust self-propulsion of the particle.

⁴Typically the body of a bacterium has a length and thickness of several micrometers, while the flagella are of the same length scale but very thin (nanometer scale).

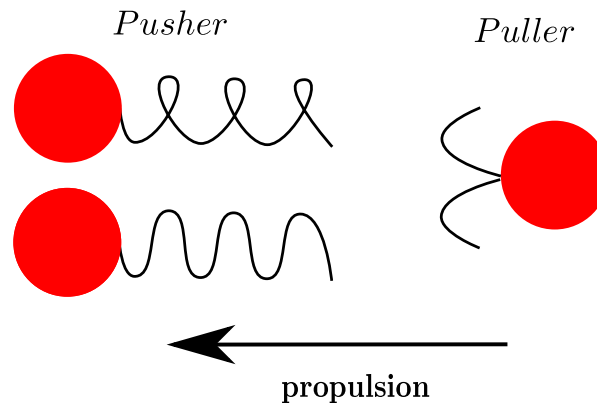


Figure 1.2.: Sketches of living microswimmers, all propagating to the left in this picture. Left: Representation of common pushers like bacteria (top) and sperm (bottom) which are propelled by either a rotating flagella bundle or a wave-like motion of the flagellum. Right: A typical puller, propelled by a “breast-stroke” motion of flagella in front of the main body, as done by *Chlamydomonas reinhardtii*.

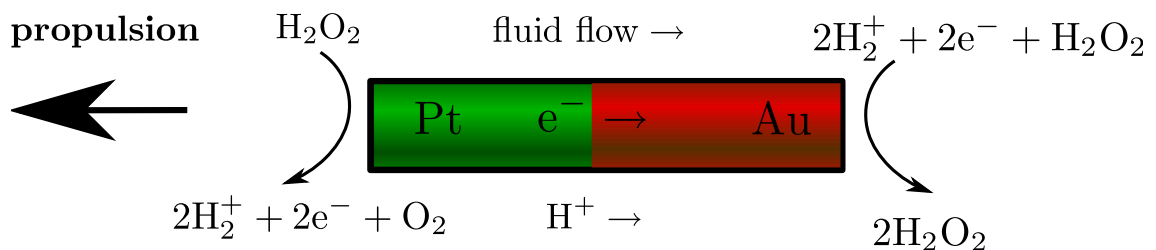


Figure 1.3.: Sketch of an artificial microswimmer, here a rodlike Janus particle. A robust directed propulsion is generated by the decomposition of hydrogen peroxide (H_2O_2) at the platinum coated half, see text for details. The same principle can be applied to spherical particles as well.

As a widespread system Janus particles⁵, i.e. particles which are differently coated, therefore leading to a symmetry breaking, are used. A typical example for the realization of artificial swimmers are Janus particles half coated with platinum and gold. Thereby, spherical as well as rodlike particles are used, see e.g. [6, 47–50]. Platinum (Pt) is a catalyst for the decomposition of hydrogen peroxide (H_2O_2) into water and oxygen [51]. Here, the strength of the self-propulsion, and thereby the velocity of the particle, can be tuned by the H_2O_2 concentration [6, 52–54], since the hydrogen peroxide is oxidized to generate protons in solution and electrons within the platinum coated side. On the other side of the particle, the gold (Au) coated side, the protons and electrons are consumed in the reduction of hydrogen peroxide. The resulting ion flux along the particle induces its motion relative to the fluid, propelling the

⁵The origin of the name is the Roman god *Janus* who is usually represented with two faces, one looking ahead and one behind.

particle towards the platinum-coated side, see Figure 1.3. This propulsion mechanism can be slightly changed by building rolled-up conelike microtubes, which are then propelled by the formed oxygen bubbles [55, 56].

Since this self-phoresis is based on diffusiophoresis, it has a big disadvantage for long time studies, as the mobility depends on the fuel concentration and the necessary fuel is consumed after some time. This is not the case if the effect of *self-thermophoresis* is used to generate a directed motion. By exposing silica particles, coated with either gold or carbon, to a laser which heats up the coated side a reversible temperature gradient is generated, which leads to a propulsion [57]. Alternatively, suspending the particles in a water-lutidine mixture a local demixing at the heated cap settles the motion of such swimmers. This has been realized in experiments for isotropic and even anisotropic particles [58, 59]. However, for this propulsion mechanism the demixing zone has to be sufficiently small.

1.3. Dynamics of active colloidal particles

Let us start with the description of a simple passive spherical colloidal particle in a liquid before we introduce the important feature of the directed propulsion of the swimmers. Such passive particles undergo a non-vanishing and undirected motion, which was observed by the botanist Robert Brown in 1827 [60]. His initial observation had been on small pollen grains and his first clue was that the erratic motion should be based on some kind of living properties of the biological material. But in further experiments, this time on granular and glassy material, he saw the same phenomenon and concluded that the origin of this motion had to be physical.

Although this observed motion is named after Robert Brown, it should be mentioned here that he was not the first one who observed this phenomenon. Already in 1784 Jan Ingen-Housz made this discovery on coal particles immersed in a fluid [61]. The origin of this non-vanishing motion was experimentally traced back to the motion of the molecules of the surrounding fluid by Christian Wiener in 1863 [62]. Later on Albert Einstein [63, 64], Marian von Smoluchowski [65] and Paul Langevin [66] were able to describe theoretically the behavior of a Brownian particle and its motion due to molecular impacts from the liquid on the particle.

Following Langevin's description, the dynamics of a single spherical passive colloidal particle under continuous bombardment by the solvent can be determined by its position \mathbf{r} using the following equation of motion

$$m \frac{d^2 \mathbf{r}}{dt^2} = -f \frac{d\mathbf{r}}{dt} + \mathcal{F}(t), \quad (1.1)$$

A statistical analysis of the motion of a single active particle, considering the mean square displacement and even higher displacement moments is given in the Appendix, following Reference [6].

where m is the mass of the particle, f corresponds to the friction coefficient due to the solvent and $\mathcal{F}(t)$ to a random force, which is supposed to describe the kicks by the solvent molecules. While Langevin assumed temporally short correlated random forces, Uhlenbeck and Ornstein pointed out that the stochastic forces are supposed to be Gaussian distributed with independent components and δ -correlated time dependence [67]

$$\langle \mathcal{F}(t) \rangle = 0 \quad (1.2)$$

$$\langle \mathcal{F}_i(t) \mathcal{F}_j(t') \rangle = 2k_B T f \delta_{ij} \delta(t - t'), \quad i, j = x, y, z. \quad (1.3)$$

The components of $\mathcal{F}(t)$ are referred to as Gaussian white noise with zero mean and intensity $2k_B T f$, where k_B is the Boltzmann constant and T is the temperature. According to the *Stokes-Einstein relation* $D = k_B T / f$ is the diffusion coefficient of a spherical particle⁶ with $f = 3\pi\eta\sigma$, where η is the viscosity of the solvent and σ the diameter of the spherical particle [63, 68].

Analogously, we can consider the orientation of the particle. The respective Langevin equation can be written as

$$I \frac{d\boldsymbol{\omega}}{dt} = -f_r \boldsymbol{\omega} + \mathcal{T}(t), \quad (1.4)$$

where I is the moment of inertia, f_r is the rotational friction coefficient and $\mathcal{T}(t)$ a random torque according to

$$\langle \mathcal{T}(t) \rangle = 0 \quad (1.5)$$

$$\langle \mathcal{T}_i(t) \mathcal{T}_j(t') \rangle = 2k_B T f_r \delta_{ij} \delta(t - t'), \quad i, j = x, y, z, \quad (1.6)$$

with $f_r = \pi\eta\sigma^3 = f\sigma^2/3$. This leads to the rotational diffusion coefficient $D_r = 3D/\sigma^2$. The angular velocity $\boldsymbol{\omega}$ is responsible for the reorientation of the swimmer

$$\frac{d\hat{\mathbf{u}}}{dt} = \boldsymbol{\omega} \times \hat{\mathbf{u}}, \quad (1.7)$$

where $\hat{\mathbf{u}}$ is the unit vector defining the particle orientation, which will be confined to the unit circle throughout this thesis.

In order to tailor this description to an active colloidal microswimmer, the low-Reynolds number regime has to be considered as previously described in Section 1.2. The motion of such a

⁶This is an example for the *fluctuation-dissipation theorem*.

particle is overdamped and inertia free, leading to a vanishing left hand side of equations (1.1) and (1.4) and the self-propulsion of active particles requires further modification. The propagation velocity can be included though an effective self-propulsion force F_0 which is directed along the direction $\hat{\mathbf{u}}^7$. Hereby, we will not account for details of the self-propulsion mechanism of the active particles and just rely on the fact that a particle migrates in the direction $\hat{\mathbf{u}}$. To consider the effect of an external potential, $U(\mathbf{r}, t)$ can be included easily⁸.

Consequently, the Langevin equation for the translational motion of an active colloidal particle⁹ can be written as the following

$$\frac{d\mathbf{r}}{dt} = \frac{D}{k_B T} [-\nabla_{\mathbf{r}} U(\mathbf{r}) + F_0 \hat{\mathbf{u}}] + \boldsymbol{\xi}(t), \quad (1.8)$$

where $\boldsymbol{\xi}_i$ is Gaussian white noise with zero mean and correlations $\langle \boldsymbol{\xi}_i(t) \otimes \boldsymbol{\xi}_j(t') \rangle = 2D\delta(t - t')\mathbb{1}$ with the unit tensor $\mathbb{1}$.

The rotational Langevin equation can be written analogously for an active Brownian particle

$$\frac{d\hat{\mathbf{u}}}{dt} = \frac{D_r}{k_B T} [-\nabla_{\hat{\mathbf{u}}} U(\mathbf{r}) + \mathbf{M}] + \boldsymbol{\zeta}(t) \times \hat{\mathbf{u}}. \quad (1.9)$$

Here $\nabla_{\hat{\mathbf{u}}}$ denotes the gradient on the unit circle and $\boldsymbol{\zeta}$ is as well a Gaussian-distributed noise with zero mean and variance $\langle \boldsymbol{\zeta}_i(t) \otimes \boldsymbol{\zeta}_j(t') \rangle = 2D_r\delta(t - t')\mathbb{1}$. The term \mathbf{M} is an additional constant torque. If it is non-vanishing, it leads to a circular motion of an active particle with a constant radius [1, 69, 70].

The stochastic noise term for the rotation of a particle is sensitive to the system which is described. While artificial microswimmers are modeled properly by equations (1.8) and (1.9), living active particles have to be modeled slightly different. For *Bacillus subtilis* any fluctuations can be neglected [3, 71] and for *Escherichia coli* the rotational noise has to be modeled more carefully, since these bacteria perform a *run-and-tumble motion* [72, 73], which means that they change direction randomly after straight swimming paths of various lengths due to chemotaxis [18]. Here the bacteria check, after each run, the concentration gradient of either an attractant or a repellent in the surrounding fluid.

If we neglect all kind of fluctuations we can rewrite the Langevin equations (1.8) and (1.9) like the following

⁷This effective self-propulsion force F_0 does not contradict the condition that a swimmer is force free.

⁸In this thesis this additional potential will be caused by steric interactions between several particles.

⁹Another term for an *active colloidal particle* would be “active Brownian particle”, which is also often used in literature.

$$\mathbf{f}_{\mathcal{T}} \frac{d\mathbf{r}}{dt} = -\nabla_{\mathbf{r}} U(\mathbf{r}) + F_0 \hat{\mathbf{u}}, \quad (1.10)$$

$$\mathbf{f}_{\mathcal{R}} \frac{d\hat{\mathbf{u}}}{dt} = -\nabla_{\hat{\mathbf{u}}} U(\mathbf{r}) + \mathbf{M}, \quad (1.11)$$

using friction tensors for the translational $\mathbf{f}_{\mathcal{T}}$ and rotational motion $\mathbf{f}_{\mathcal{R}}$. These friction tensors depend on the actual particle geometry. In each chapter the exact representation of the Langevin equations will be given and possible changes will be explained.

All computer simulation results presented in this thesis have been performed via *Brownian dynamics simulations* in two spatial dimensions. This technique uses the Langevin equations, which have been discussed above, ergo stochastic differential equations which are integrated forward in time to create trajectories of particle motion. Hence it is a perfect tool to study the temporal evolution and dynamics of active fluids [74].

1.4. The Yukawa segment model

For the numerical study of active fluids we chose the Yukawa segment model to build self-propelled units of any shape. We will concentrate in this work on stiff spherical and rodlike active particles and introduce the particle aspect ratio $a = \ell/\lambda$ which is a dimensionless number representing the quotient of the particle length ℓ and width λ . Accordingly, a spherical particle corresponds to the case of $a = 1$, while rodlike particles will be considered in a range up to $a = 10$. The position of an active particle α will be described by its center of mass position \mathbf{r}_{α} and the orientation by the unit vector $\hat{\mathbf{u}}_{\alpha} = (\cos \varphi_{\alpha}, \sin \varphi_{\alpha})$.

A rodlike particle is discretized into n spherical segments. The number n obviously depends on the aspect ratio of the particle and is given by [75]

$$n = \lfloor 9a/8 \rfloor, \quad (1.12)$$

with $\lfloor \cdot \rfloor$ denoting the nearest integer. These n segments are placed along the main particle axis, which corresponds to the orientation $\hat{\mathbf{u}}$. The distance d between individual segments is

$$d = \ell / [(n+1)(n-1)]^{1/2}, \quad (1.13)$$

which means that the distance $d \leq \lambda$ is always valid.

The total pair potential between two swimmers α and β is modeled by a repulsive Yukawa potential and given by

$$U_{\alpha\beta} = \frac{U_0}{n^2} \sum_{i=1}^n \sum_{j=1}^n \frac{\exp[-(r_{ij}^{\alpha\beta}/\lambda)]}{r_{ij}^{\alpha\beta}}, \quad (1.14)$$

where $U_0 > 0$ is a prefactor¹⁰ and

$$r_{ij}^{\alpha\beta} = |\Delta\mathbf{r}_{\alpha\beta} + (l_i\hat{\mathbf{u}}_\alpha - l_j\hat{\mathbf{u}}_\beta)| \quad (1.15)$$

is the distance between the i th segment of rod α and the j th segment of rod β , with $l_i \in [-(\ell - \lambda)/2, (\ell - \lambda)/2]$ denoting the position of segment i along the symmetry axis of the rod α , see Figure 1.4.

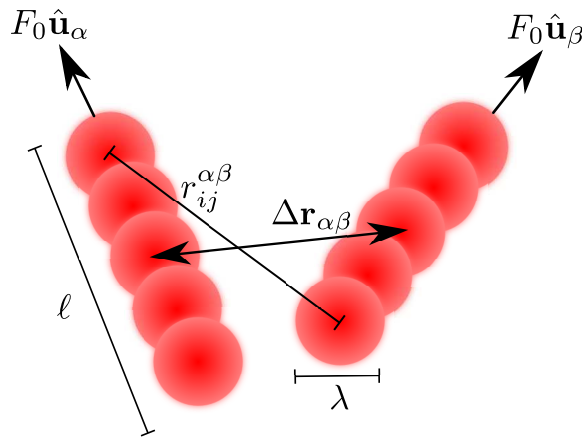


Figure 1.4.: Sketch of a rodlike self-propelled particle pair $\{\alpha, \beta\}$ build up by the Yukawa segment model. Each rod consists of $n = 5$ such segments, has a length ℓ and width λ , leading to an aspect ratio $a = \ell/\lambda$. The effective self-propulsion force F_0 acts along the main rod orientation $\hat{\mathbf{u}}$. Additionally indicated is the center of mass distance $\Delta\mathbf{r}_{\alpha\beta}$ and $r_{ij}^{\alpha\beta}$, the distance between segment i of rod α and segment j of rod β .

We will focus on the dynamics of active particles propagating with a velocity v_0 . As introduced in Section 1.2, the respective self-propulsion force F_0 is directed along the particle orientation $\hat{\mathbf{u}}_\alpha$, see again Figure 1.4.

The translational $\mathbf{f}_\mathcal{T}$ and rotational $\mathbf{f}_\mathcal{R}$ friction tensors can be decomposed into parallel f_\parallel , perpendicular f_\perp and rotational $f_\mathcal{R}$ components in the following way,

¹⁰A detailed study shows that the collective behavior of sufficiently hard rods is only weakly dependent on the exact value of the Yukawa amplitude [76]. Furthermore we will restrict our studies to monodisperse systems.

$$\mathbf{f}_{\mathcal{T}} = f_0 [f_{\parallel} \hat{\mathbf{u}}_{\alpha} \hat{\mathbf{u}}_{\alpha} + f_{\perp} (\mathbb{1} - \hat{\mathbf{u}}_{\alpha} \hat{\mathbf{u}}_{\alpha})], \quad (1.16)$$

$$\mathbf{f}_{\mathcal{R}} = f_0 f_{\mathcal{R}} \mathbb{1}, \quad (1.17)$$

with a Stokesian friction coefficient f_0 and the 2D unit tensor $\mathbb{1}$. The dimensionless geometric factors $\{f_{\parallel}, f_{\perp}, f_{\mathcal{R}}\}$ depend solely on the aspect ratio a of the rodlike particles. Here we adopt the standard expression for stiff rodlike macromolecules as given in Ref. [77],

$$\frac{2\pi}{f_{\parallel}} = \ln a - 0.207 + 0.980a^{-1} - 0.133a^{-2}, \quad (1.18)$$

$$\frac{4\pi}{f_{\perp}} = \ln a + 0.839 + 0.185a^{-1} + 0.233a^{-2}, \quad (1.19)$$

$$\frac{\pi a^2}{3f_{\mathcal{R}}} = \ln a - 0.662 + 0.917a^{-1} - 0.050a^{-2}. \quad (1.20)$$

The described model is an established one for charged rodlike colloids [78–80], such as suspensions of the tobacco-mosaic virus [75, 81], fd-virus [82] and DNA strands [83–85]. It has already been extensively used to model active particles, showing good agreement to experimental results, see e. g. Ref. [76, 86, 87]. Such a segment model has also been used for different repulsive potentials like a shifted Lennard-Jones potential, showing similar results in the case of self-propelled rods [88].

Any modifications of this particle model will be explicitly described in the respective chapter.

1.5. Polymer physics

In general a polymer is a large molecule consisting of many small simple chemical units, called monomers, which are joint together. Accordingly, such polymers can be modeled by N segments connected with bonds of length b .

In order to make an assumption on the statistical properties of such a polymer, the spatial extension will be discussed in the following. At first we will start with the simplest model of an *ideal chain* before introducing more complex models. In case of such an ideal chain it is assumed that there are no correlations between the directions of different bonds and all directions occur with the same probability. Furthermore, the monomers do not interact with each other at all. The resulting polymer chain conformation is the same as a random walk on a lattice.

To make an assumption on the spatial extension, i.e. the length of the polymer, we start with the *end-to-end vector* \mathbf{R}_E , which joins one end of the chain with the other. For a chain with N monomers with bond vectors \mathbf{r}_i it is given by

$$\mathbf{R}_E = \sum_{i=1}^N \mathbf{r}_i. \quad (1.21)$$

Obviously, the average of this quantity vanishes, $\langle \mathbf{R}_E \rangle = 0$, since all directions have the same probability. Therefore, the second moment $\langle \mathbf{R}_E^2 \rangle$, which is the average of the square of the end-to-end vector,

$$\langle \mathbf{R}_E^2 \rangle = \sum_{i=1}^N \sum_{j=1}^N \langle \mathbf{r}_i \cdot \mathbf{r}_j \rangle, \quad (1.22)$$

will be considered and its square root will be used to express R_E , the length of the end-to-end vector. Since there are no correlations between the directions of the bonds if $i \neq j$, $\langle \mathbf{r}_i \mathbf{r}_j \rangle = \langle \mathbf{r}_i \rangle \cdot \langle \mathbf{r}_j \rangle = 0$ is valid. Consequently, equation (1.22) can be rewritten as

$$\langle \mathbf{R}_E^2 \rangle = \sum_{i=1}^N \langle \mathbf{r}_i^2 \rangle = Nb^2. \quad (1.23)$$

The same scaling for large numbers of monomers N can be found if a fold-back of two consecutive bonds is excluded through interactions within the chain. Even in case of a *Gaussian chain*¹¹ this scaling is unaffected, although an effective bond length may be used to express the average end-to-end distance. For all these simple models excluding interactions between the segments themselves, the scaling

$$R_E \sim N^{1/2} \quad (1.24)$$

is valid.

The end-to-end distance is only a valid quantity to measure the spatial extension in the case of chainlike polymers. For branched or starlike polymers using the end-to-end distance characterization is inappropriate. Instead it is common to evaluate the *radius of gyration* as a quantity describing the spatial extension for polymers of all shapes – even for chains. Another advantage of this quantity is that it can be measured by means of scattering experiments, which is not possible for the end-to-end distance. The radius of gyration R_G is defined by the square root of

¹¹In case of a Gaussian chain it is assumed that the bond vector \mathbf{r} itself possesses flexibility and follows a Gaussian distribution.

$$R_G^2 = \frac{1}{N^2} \sum_{i=1}^N \sum_{j=1}^N \langle (\mathbf{R}_i - \mathbf{R}_j)^2 \rangle, \quad (1.25)$$

where \mathbf{R}_i corresponds to the position of the i th monomer of the polymer. By using the position of the *center of mass*

$$\mathbf{R}_C = \frac{1}{N} \sum_{i=1}^N \langle \mathbf{R}_i \rangle, \quad (1.26)$$

R_G^2 can be expressed as the square of the average distance between the single segments of the polymer and its center of mass

$$R_G^2 = \frac{1}{N} \sum_{i=1}^N \langle (\mathbf{R}_i - \mathbf{R}_C)^2 \rangle. \quad (1.27)$$

Let us now focus on the actual scaling behavior of the radius of gyration. Again, in the case of a long ideal chain, $\mathbf{R}_i - \mathbf{R}_j$ has a Gaussian distribution with variance $|i - j|b^2$. Equation (1.25) can be rewritten in the following way

$$R_G^2 = \frac{1}{2N^2} \sum_{i=1}^N \sum_{j=1}^N |i - j|b^2 = \frac{1}{6}Nb^2. \quad (1.28)$$

As a result, $R_G^2/R_E^2 = 1/6$ and both quantities show the exact same scaling behaviors, $R_G \sim N^{1/2} \sim R_E$ [89, 90].

Up to now we have dealt with polymers which are not self-avoiding. If we consider self-avoidance, the scaling exponent, which we will call ν from now on, is different. Since excluded volume effects have to be considered for real chains, the scaling exponent for the spatial extension should be larger than before, so $\nu > 1/2$. We will now focus on Paul Flory's approach to determine this exponent by assuming a self-avoiding polymer chain with an unknown radius R and N monomers in d dimensions [91]. The total repulsive energy E scales as

$$E \sim \frac{N^2}{R^d}. \quad (1.29)$$

Here, we assume a monomer concentration $c \sim N/R^d$ and integrated the repulsive energy between the monomers which scales with $E_m \sim c^2$ over the volume R^d . According to equation (1.29) the total energy of a polymer decreases with increasing spatial extension of the polymer. Consequently, elongated chains are the preferred configuration. However, this leads to a minimization of the entropy. To avoid this, Flory introduced a term for the entropy according to an elastic energy

$$S \sim \frac{R^2}{b^2 N}, \quad (1.30)$$

where b is the length of a bond as before.

It is well known that these approximations overestimate the repulsion because they ignore correlations. However, the entropy term is overestimated as well [90], so these two errors cancel each other out to give a good approximation. The free energy of the considered system can be estimated by

$$F \sim \frac{N^2}{R^d} + \frac{R^2}{b^2 N}. \quad (1.31)$$

Its minimum

$$R^{d+2} \sim b^2 N^3 \quad (1.32)$$

leads to a general scaling $R \sim N^\nu$ with the well known Flory exponent [91]

$$\nu = \frac{3}{d+2}, \quad (1.33)$$

and thus $\nu = 3/4$ in two dimensions and $\nu = 3/5 \sim 0.588$ in three dimensions¹², which has been studied extensively by simulations [93].

¹²Flory introduced the scaling exponent for the case of $d = 3$. For general d it was first quoted in Ref. [92].

Vortex arrays as emergent collective phenomena for circle swimmers

Both swimming micro-organisms [94, 95] and synthetic colloidal swimmers [40] are able to form remarkable collective spatiotemporal patterns [73, 96–101] including swarming [102–105] and complex swirling [76, 106–114] behavior. Most of the observed patterns can be obtained by a simple modeling that includes the tendency of the particles to move autonomously and their direct interaction mainly governed by the excluded volume of effective anisotropic objects [76, 86]. When supplemented with Brownian dynamics, binary collisions between neighboring particles lead to mutual alignment and thus provide a mechanism of swarming [115]. The observed effects occur in most cases in two dimensions, i.e., for particles moving in a planar geometry.

In fact, self-propelled particles in two dimensions can be realized in a number of ways including autonomously navigating confined bacteria and microbes [107, 108, 116–119], polar granular rods on a vibrating flat surface [120, 121], flagellated alga [122], and even pedestrians in a pedestrian zone [13, 14]. Moreover, colloidal dispersions have been shown to provide various valuable model systems of active matter [37, 50, 123–128]. Most of these particles have an anisotropic rodlike shape and move along their orientation axis such that a single particle proceeds along a line. This is a key ingredient in previous modeling of many swimmers [84, 105, 115, 129–133].

Moreover, self-propelled particles have been discovered that move in circles rather than in a straight line. Examples for these circle swimmers include various bacteria [134–139], protozoans [140], microtubules [141], spermatozoa [109, 142, 143], crustaceans [144], and spherical camphors that have been shown to exhibit circular swimming at an interface [145]. Furthermore, synthetic microswimmers with various shapes exhibit circular motion [58, 59, 146, 147]. Driven Brownian particle models [69, 70, 148–150] have been proposed to describe the basic physics of circle swimmers where the particles proceed with both an effective translational and angular propagation velocity and experience additional Brownian fluctuations. The determin-

This chapter has been published in a very similar form by Andreas Kaiser and Hartmut Löwen, *Phys. Rev. E* **87**, 032712 (2013), see Reference [1].

istic (noise-free) trajectory in two dimensions is a closed circle. More explicit models that resolve the swimming strokes have recently been put forth for single circle swimmers [151, 152].

However, the collective properties of circle swimmers at finite density are rarely understood. Experiments [109] have shown emerging dynamic arrays of vortices for spermatozoa resembling quantized rotating waves if the density exceeds a threshold. The origin was explained in terms of hydrodynamic interactions. However, apart from a coarse-grained recent diffusive theory [153], there is no particle-resolved simulational study nor any theoretical study for the emergent behavior of many circle swimmers. Here we simulate the collective behaviour of many circle swimmers by a minimal model in two spatial dimensions incorporating excluded volume interactions. The swimmers are interacting via a strongly repulsive and short-range Yukawa-segment potential [75], which prevents particles from overlapping. Each rod has a length ℓ . The self-motility of the individual swimmers is imposed by introducing a constant translational velocity along the main orientation axis of each rod and a constant angular velocity that rotates each rod. The combination of both translational and rotational self-propulsion results in a circular swimming path for the center of mass of radius R for each individual rod. At finite density, different circle swimmers will collide, leading to nontrivial emergent behavior that gets crowded and nontrivial if the area πR^2 embraced by a single swimmer is occupied on average by two or more swimmers. In particular, at intermediate and high densities, novel emerging effects are expected.

The model considered here has been studied previously in two special limits, namely, for vanishing angular velocity [76, 86] and vanishing translational velocity [154]. For vanishing angular velocity, we recover the special case of linear swimmers that move in straight lines corresponding to the limiting case $R \rightarrow \infty$. Even though the averaged swimming direction is constant, it has been shown [76, 86] that at finite density, swirls emerge in the model. The average rotational sense of the swirls, however, averages to zero due to symmetry. The complementary case of vanishing translational velocity [154, 155] describes passive rotors. The absence of translational propulsion leads to a vanishing swimming radius R . These rotors can be realized by placing passive colloids into circularly polarized light fields [156–158]. Passive rotors have been shown to exhibit a T structure of neighboring rotating rods that can also be viewed as a special kind of vortex array, a *singlet vortex*, in the sense that each rotor forms its own vortex and neighboring vortices possess perpendicular rod orientation. The compact though dynamic T structure is formed since mutual collisions are avoided. At high density, the vortex array structure disappears due to jamming [154], leaving a slowed rotor fluid as the high-density state.

In our simulation of many circle swimmers, we have the radius R of a single swimmer’s path as an additional parameter. First we confirm that the singlet-vortex phase and the slowed rotor fluid phase that were discovered previously for vanishing R [154] possess a large stability for finite R . More surprisingly, we find a novel vortex array formation at intermediate swimmer densities and an intermediate range of radii R . In this phase, the vortices are composed of circle swimmer *pairs* that are oriented antiparallel with respect to each other. Many of these *doublet vortices* exhibit strong structural ordering on an array. We propose a simple theory to predict the onset of circle swimmer pairing to understand the underlying mechanisms for

vortex array formation. Our vortex array is induced by steric interactions together with circular self-propulsion and is therefore different in origin that the hydrodynamically induced vortices of Refs. [109, 159]. The rotation sense of the vortices is obviously correlated with the sense of rotation of a single swimmer since the clockwise or counterclockwise symmetry of rotation is broken in our model. This make our vortex pairing different from previous explorations of swirling in linear swimmers at intermediate densities [76, 107, 108, 160, 161]. In principle, our results are verifiable for bacterial and artificial rodlike circle swimmers.

This Chapter is organized as follows: In Section 5.1 we specify our model for circle-swimming self-propelled rods, the corresponding equations of motion and the simulation technique. Simulation results on the nonequilibrium state diagram are presented and analyzed in Section 2.2 while in Section 2.3 a simple theory is proposed to predict the vortex formation. We conclude in Section 5.4 with a brief discussion of possible extensions of the model and highlight opportunities to observe the predicted behavior in experiment.

2.1. Frictional dynamics of a self-propelled-rod model

The rodlike circle swimmers in our model are characterized by a length ℓ and are driven by a constant self-propulsion force F directed along the main rod axis $\hat{\mathbf{u}}$. The actual position of the α th rod ($\alpha = 1, \dots, N$) is described by a center of mass position vector \mathbf{r}_α and a unit orientational vector $\hat{\mathbf{u}}_\alpha = (\cos \varphi_\alpha, \sin \varphi_\alpha)$. We do not resolve the details of the swimming mechanism. The force F is a formal one that results in some overdamped dynamics in a constant propagation velocity as in previous models [5, 86, 130]. Similarly, the circular movement is implemented using an additional torque \mathbf{M} normal to the plane of motion as described for a single rod in Ref. [69]. The rods themselves are modelled by the Yukawa segment model, as introduced in Section 1.4.

Accodring to the low-Reynolds-number limit, the translational and rotational equations of motion can be written as

$$\mathbf{f}_T \cdot \partial_t \mathbf{r}_\alpha = -\nabla_{\mathbf{r}_\alpha} U + F \hat{\mathbf{u}}_\alpha, \quad (2.1)$$

$$\mathbf{f}_R \cdot \partial_t \hat{\mathbf{u}}_\alpha = -\nabla_{\hat{\mathbf{u}}_\alpha} U + \mathbf{M}. \quad (2.2)$$

Here F is the constant self-motility force acting along the longitudinal axis of each rod (see Figure 2.1), $U = (1/2) \sum_{\beta, \alpha: \beta \neq \alpha} U_{\alpha\beta}$ is the total potential energy, $\nabla_{\hat{\mathbf{u}}}$ denotes the gradient on the unit circle, and \mathbf{f}_T , \mathbf{f}_R are the translational and rotational friction tensors. The dimensionless geometric factors $\{f_{\parallel}, f_{\perp}, f_R\}$ depend solely on the aspect ratio a and we adopt the standard expressions for rodlike macromolecules, as given in Ref. [77], and shown in Section 1.4.

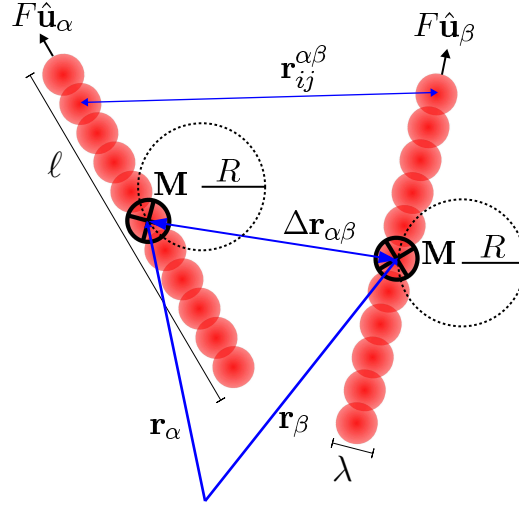


Figure 2.1.: Sketch of a pair of rodlike circle swimmers with $n = 11$ repulsive Yukawa segments and aspect ratio $a = \ell/\lambda$. Self-propulsion is provided by a constant force F acting along the main rod axis $\hat{\mathbf{u}}$. The circular motion is brought about by an additional torque \mathbf{M} perpendicular to the plane of motion. The total rod pair potential is obtained by a sum over all Yukawa segment pairs with distance $r_{ij}^{\alpha\beta}$ and is a function of the center of mass distance vector $\Delta\mathbf{r}_{\alpha\beta}$ and orientations (1.14). The circular swimming path of radius R of the center of mass coordinates is also indicated.

The constant torque M , directed perpendicular to the plane of motion (see Figure 2.1), induces a circular motion of a single swimmer with a radius

$$R = \frac{f_{\mathcal{R}} F}{f_{\parallel} M}, \quad (2.3)$$

and an angular velocity

$$\omega_0 = \frac{M}{f_{\mathcal{R}}}. \quad (2.4)$$

Clearly, there is no finite temperature in our model as any stochastic fluctuations are ignored.

In our simulations, we have adopted characteristic units such that $\lambda = 1$, $F = 1$, and $f_0 = 1$, which means that distance is measured in units of λ , velocity in units of F/f_0 , time in units of $\tau_0 = \lambda f_0/F$ and energy in units of $F\lambda$. Upon rescaling to dimensionless coordinates, four relevant system parameters remain: the dimensionless Yukawa amplitude $\tilde{U}_0 = U_0/(F\lambda)$, which determines the hardness of the rod interactions relative to their characteristic propulsion

energy, the aspect ratio a , the reduced radius R/λ , and the packing fraction of the rods. This fraction is specified in terms of the dimensionless area fraction

$$\eta = \frac{\pi N}{4 A} \ell^2 \quad (2.5)$$

where N is the total number of rodlike circle swimmers and A denotes the area of the quadratic simulation box. For steeply repulsive Yukawa interactions, the general dynamical behavior resembles that of hard rods and only weakly depends on the Yukawa amplitude and we set $\tilde{U}_0 = 250$. We further consider anisotropic rods with fixed aspect ratio $a = 10$. The remaining quantities, the reduced swimmer radius R/λ and area fraction η constitute the main steering parameters for our investigation. We simulate the evolution of the many-body self-propelled rod model as a function of time $\tau = t/\tau_0$ in a square box with periodic boundary conditions at packing fractions in the range $0.1 < \eta < 2.5$. The simulations are carried out using a total number of $N = 10^3$ rods. Initial configurations are generated from a rectangular lattice of aligned rods with \hat{u} pointing randomly up or down. The rods are randomly displaced from the initial lattice such that the starting configuration bears already some randomness. We have tested different random starting configurations and confirmed that the steady state properties do not depend on the starting configuration. We then relax the system during an time interval of a transitory time $\tau_T = 2000$ before statistics are being gathered over an interval $\tau_S = 40\,000$. We checked that the results do not depend on τ_T if τ_T is chosen larger than 2000. Moreover, we have done longer exploration runs with $\tau_S = 100\,000$ to confirm that the steady state averages are reproduced. Finally, we have checked the system size dependence by systematically exploring particle numbers in the range of $N = 100 - 1000$ particles. The occurrence of the different steady states is stable.

2.2. Simulation results

Figure 2.2(a) shows a state diagram for rodlike circle swimmers in the two-dimensional parameter space of swimmer density η and swimming radius R . Four different states emerge, for which typical simulation snapshots are shown in Figures 2.2(b) - 2.2(e)¹. We discriminate between different states by suitable order parameters as explained in detail below, but emphasize here that there are no strict phase transitions between the different states. Let us first discuss the contents of Figure 2.2 before we characterize the states in more detail.

For low densities there are only very few collisions and therefore little or no collective motion. Consequently, there is a *dilute* state at low density η [see Figure 2.2(b)]. Complementarily, at high density, there is a *slowed rotor fluid* with no particular mesostructure [see Figure 2.2(e)]. In this state, rotating rods collide, which slows down their mean angular velocity. More interestingly, there are intervening phases at intermediate densities. We find two different vortex array states. The first consists of singlet vortices such that every vortex comprises a single

¹See <http://link.aps.org/supplemental/10.1103/PhysRevE.87.032712> for movies showing the individual occurring states.

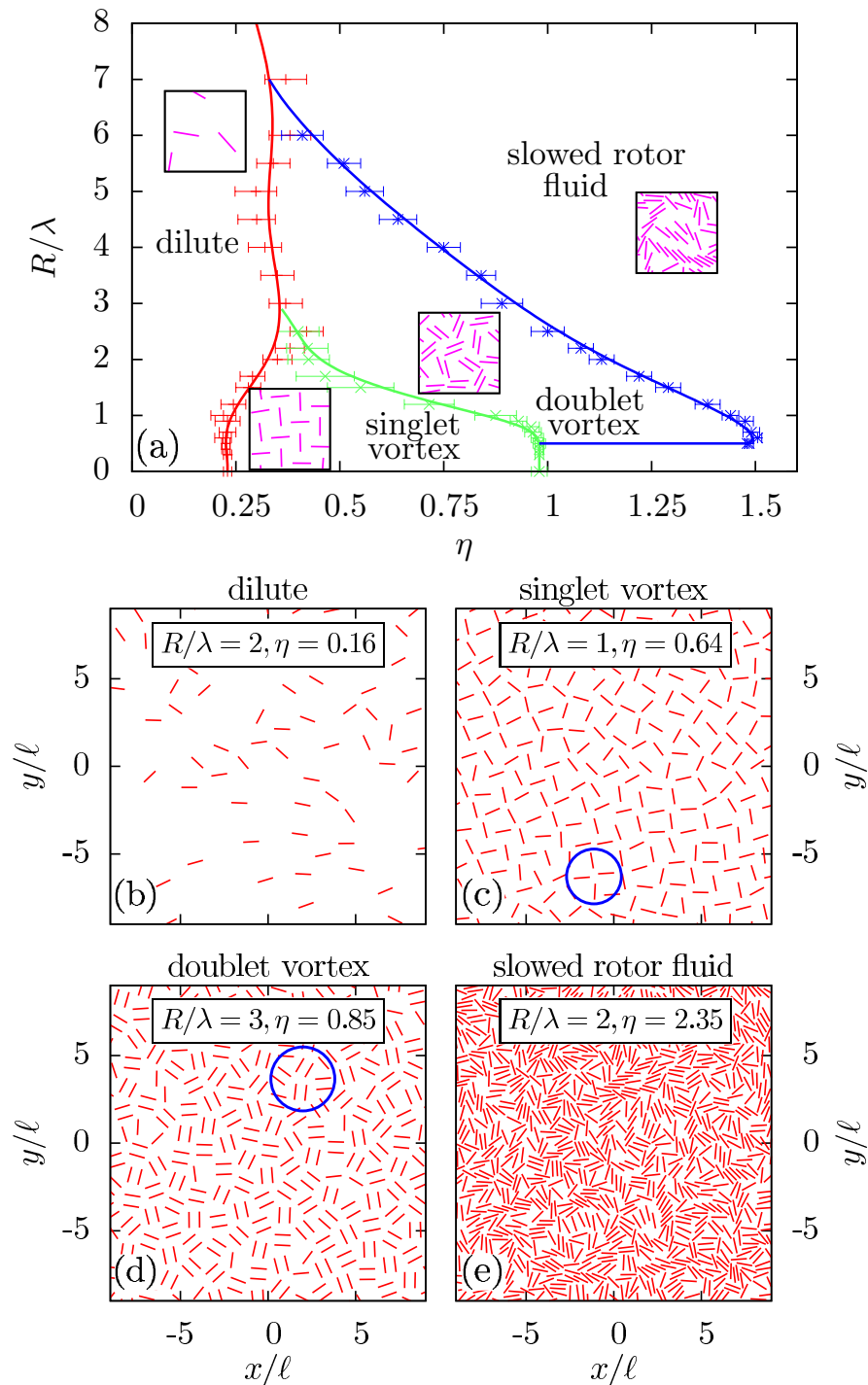


Figure 2.2.: (a) Nonequilibrium state diagram of rodlike circle swimmers in the parameter space spanned by the swimming radius R and the swimmer density η . Four different states emerge, which are depicted as - dilute for low swimmer densities, singlet vortex for intermediate densities and low rotation radii, doublet vortex for higher swimmer densities and slowed rotor fluid for even higher densities. (b)-(e) Characteristic simulation snapshots for the four states are also shown, including blue circles to show typical configurations of the vortex array states.

particle. This phase has been called T structure in earlier investigations for passive particles at vanishing radius R [154] since it clearly shows a perpendicular orientation of neighboring rods. We refer to this state here as a *singlet-vortex* array phase as every particle rotates around its own such that any vortex comprises a single particle [see Figure 2.2(c)]. The second phase is a *doublet-vortex* array such that each vortex comprises two rods that are oriented in an antiparallel way. The rod pairing is clearly visible in the snapshot shown in Figure 2.2(d). It is important to note that the doublet-vortex state is stable only in a finite range of swimming radii $\lambda/2 < R < 7\lambda$. Its transition density towards the slowed rotor fluid exhibits a large nonmonotonicity in R , which implies a marked reentrant behavior of the slowed rotor fluid if R is increased at fixed density. For the parameter space studied, we never found vortices with more than two rods.

In more detail, we now define order parameters in order to distinguish and characterize the four different states. To analyze the orientation of neighboring rods we define normalized orientational order parameters

$$m_1 = \langle \cos \theta(r) \rangle_s, \quad (2.6)$$

$$m_2 = \langle \cos^2 \theta(r) \rangle_s, \quad (2.7)$$

where $\langle \dots \rangle_s = \int_0^s dr g(r) \dots / \int_0^s dr g(r)$ is a statistical steady state average. These order parameters correspond to measures of the polar and nematic order in a neighbor shell of size s . Here $g(r)$ is the pair correlation function between two rods (provided their center of mass positions have a distance r) and $\theta(r)$ denotes the angle between their orientations. Moreover, $s = (N/A)^{-1/2}$ is the average distance between two rods. The order parameter m_2 was already applied to evaluate passive rotors [154].

In the case of no correlation of neighboring rods $m_1 = 0$ and $m_2 = 0.5$. Perpendicular orientation is indicated by $m_1 = 0$ and $m_2 = 0$. A perfect parallel orientation leads to $m_1 = 1$ and $m_2 = 1$, while an antiparallel alignment is represented by $m_1 = -1$ and $m_2 = 1$. Furthermore, we calculate (as a dynamical diagnostics) the mean angular velocity

$$\langle \omega \rangle = \frac{1}{N} \sum_{\alpha=1}^N \dot{\varphi}_\alpha \quad (2.8)$$

of the rods.

The dilute state is characterized by almost freely rotating rods with just a few collisions. We define this state by a combination of structural and dynamical criteria demanding that $m_1 > -0.4$, $m_2 > 0.4$, and $\langle \omega \rangle \geq 0.99\omega_0$ should hold in the dilute state. Moreover, the singlet-vortex state is defined via the condition $m_2 \leq 0.4$, which brings about strong perpendicular orientation of neighboring rods. Conversely, for doublet vortices we require $m_1 \leq -0.4$, indicating that neighboring rods are orientated in an antiparallel way. The slow rotor fluid state is defined by the combined complementary conditions $m_1 > -0.4$, $m_2 > 0.4$, and $\langle \omega \rangle < 0.99\omega_0$.

Simulation data for the orientational order parameters m_1 and m_2 and the mean angular velocity $\langle \omega \rangle$ are given in Figures 2.3 and 2.4(a), respectively, as a function of swimmer density

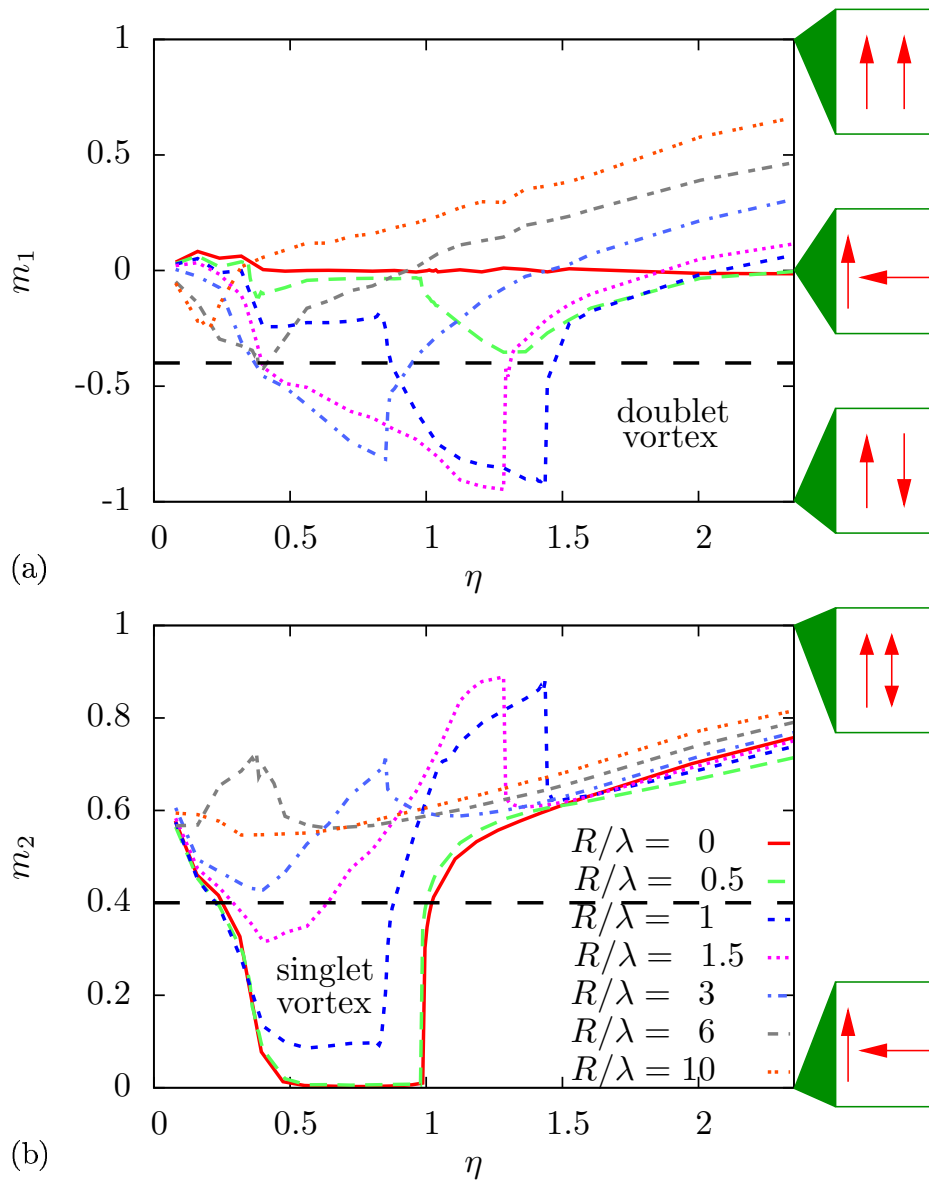


Figure 2.3.: Orientational order parameters (a) m_1 and (b) m_2 for several swimming radii R as a function of swimmer density η . The horizontal dashed lines represent the criteria for the vortex states. Typical swimmer configurations, hereby their orientation is indicated by arrows, for selected order parameter values are sketched on the right – in the case of no correlation of neighboring rods $m_1 = 0$ and $m_2 = 0.5$.

η for various swimming radii R . These plots are consistent with the state diagram shown in Figure 2.2(a). In detail, for low densities, clearly the dilute state emerges. For small radii, m_2 drops down to zero for intermediate densities and then increases again. This demonstrates the occurrence of the singlet-vortex state. At higher densities there is no indication for the doublet-

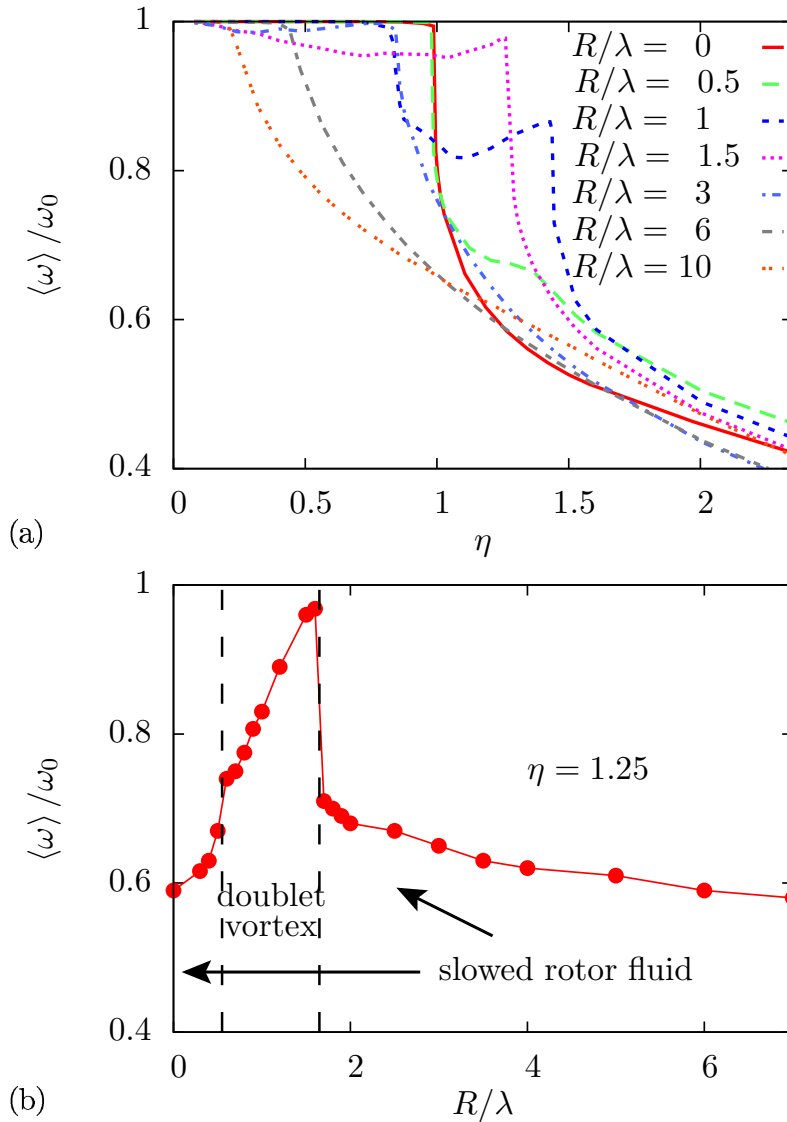


Figure 2.4.: (a) Reduced circular frequency $\langle \omega \rangle / \omega_0$ as a function of swimmer density η and different rotation radii R . (b) Reduced circular frequency $\langle \omega \rangle / \omega_0$ as a function of swimmer radius R for a fixed swimmer density $\eta = 1.25$ showing the reentrance of the slowed rotor fluid. The intermediate doublet vortex state is denoted by vertical dashed lines.

vortex state, but the system goes directly into the slowed rotor fluid state, as indicated by an alignment that leads to the increase of m_2 . This is accompanied by a very sharp reduction in the mean angular velocity as shown in Figure 2.4(a).

For $R > \lambda/2$, in contrast, there is an overshoot of m_2 as a function of density just after the singlet vortex is stable, implying a parallel ordering of neighboring rods. This points to the new state of doublet vortices. This is simultaneously revealed by a largely negative m_1

as indicative for the antiparallel doublet-vortex state. Again, further increasing of the density leads to the slowed rotor fluid state where the swimmers hinder each other in rotating [see again Figure 2.4(a)].

Finally, for very large R , the dilute to slowed rotor fluid state becomes more and more blurred. For $R \rightarrow \infty$ the crossover from the dilute to a swarming state [103, 115] is approached slowly as observed in Ref. [86].

Figure 2.4(b) shows the mean angular velocity $\langle \omega \rangle$ now as a function of the swimming radius R for fixed density $\eta = 1.25$. Clearly $\langle \omega \rangle$ is nonmonotonic, revealing again the reentrant transition of the slowed rotor fluid phase with an intermediate doublet-vortex phase.

As a general final remark the order parameter plots Figures 2.3 and 2.4 reveal that some transitions are pretty sharp (in particular the transition from the doublet vortex to the slowed rotor fluid state at low R) and other are rather smooth crossovers whose location depends a bit on the precise definition of the states (as for the transition from the doublet vortex to the slowed rotor fluid state at high R). We emphasize, however, that the global topology of the state diagram does not change if the transition criteria as shown by the dashed lines in Figure 2.3 are modified.

2.3. Simple Theory

Let us now present a simple instability theory to predict the state diagram of rodlike circle swimmers. For a vanishing swimming radius R , as already denoted in Ref. [154], the singlet vortices are mostly governed by a situation where four rodlike circle swimmers on a square lattice rotate with a relative perpendicular orientation [see again the encircled region of the snapshot shown in Figure 2.2(c)]. For infinitely thin needles ($\lambda \rightarrow 0$), as sketched in Figure 2.5(a), the circles covered by the needle orientation can overlap if the rotating motion is performed coherently with a fixed relative phase shift. The maximal packing fraction that can be reached in this configuration is when needles of length ℓ are placed on a square lattice of lattice constant $\ell/\sqrt{2}$ [see again Figure 2.5(a)], resulting in a threshold packing fraction of

$$\eta_0 = \frac{\pi}{2}. \tag{2.9}$$

Rods with an effective finite thickness λ need to be more distant to avoid overlap upon their coherent rotation, corresponding to the infinitely thin needles of a larger length $\ell + \lambda$ [see again Figure 2.5(a)]. If they perform an additional circling of swimming radius R [see Figure 2.5(b)], this effective length needs to be augmented by $2R$ such that the singlet-vortex state should be stable up to

$$\eta_1(R) = \eta_0 \left(\frac{\ell}{\ell + 2R + \lambda} \right)^2. \tag{2.10}$$

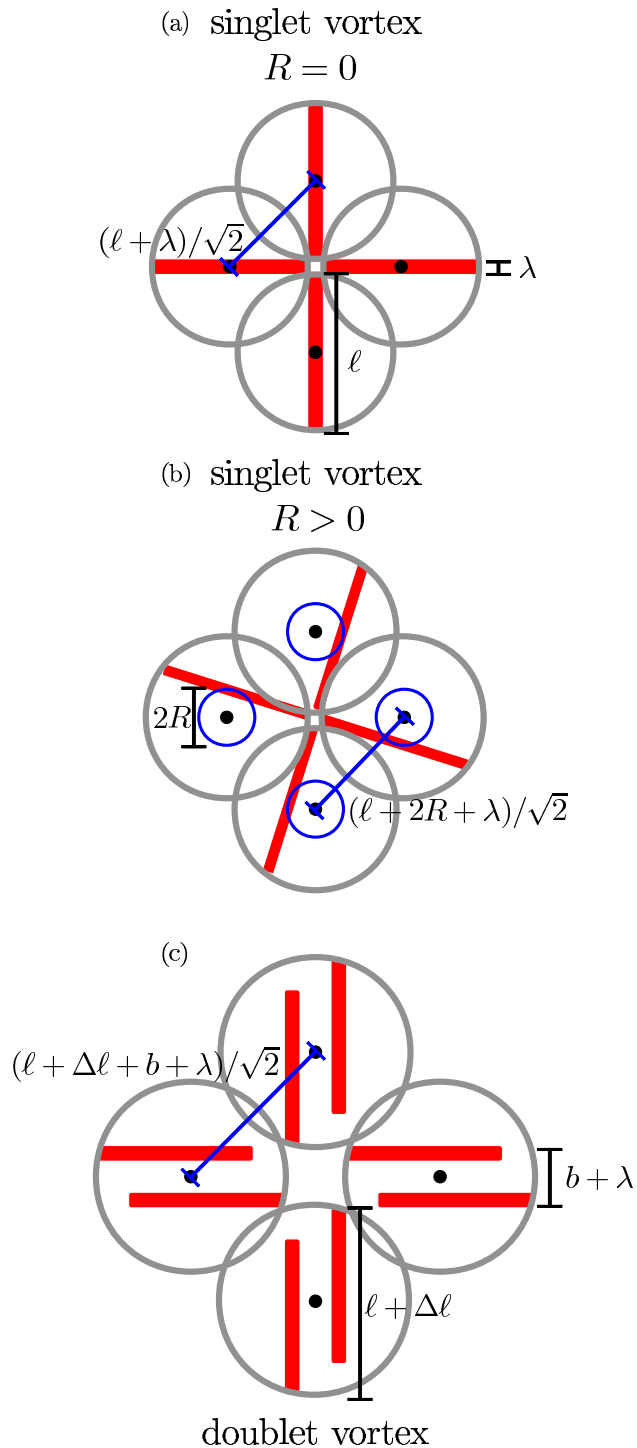


Figure 2.5.: Schematic representations of rod-shaped circle swimmers in the vortex states, showing typical configurations marked in Figures 2.2(b) and 2.2(c). The singlet-vortex state is illustrated for (a) a passive rodlike particle and (b) an active swimmer whose center of mass moves on a circle with radius R , shown here by small blue circles. The doublet-vortex state is sketched in (c). In all figures black dots represent the rotation center of the swimmers, while the light gray circles indicate the area covered by the circle swimmers during a full rotation. The lattice constants for all square lattices are given as well.

We now employ a similar argument for the doublet-vortex state by considering effective composite rods consisting of a swimmer pair [see Figure 2.5(c)]. A suitable cutout from a simulation snapshot is presented in Figure 2.2(d). In the simulations, the pairs are observed to rotate around their joint center of mass without exhibiting any circling. The swimmer pair [see the encircled region of the snapshot shown in Figure 2.2(d)] possesses typically an inter-rod distance b and is laterally shifted by an amount of $\Delta\ell$ [see again Figure 2.5(c)]. In general, these two quantities depend on the prescribed swimming radius R and the prescribed density η . Lacking any theoretical input for these quantities b and $\Delta\ell$, we resort in our simulation data to determine them and to achieve at least a consistent theory. In detail, we identify swimmer pairs by a center of mass distance less than a cutoff r_c that we chose in the considered density range as $r_c = 8\lambda$. For all identified pairs, we average their mutual distance b and their lateral shift $\Delta\ell$. Results are presented in Figure 2.6(a). Interestingly, b and $\Delta\ell$ depend strongly on the swimming radius R , but are rather density independent. In fact, the data obtained for two selected densities $\eta = 0.75$ and 1 almost coincide. Therefore, we skip the density dependence and consider just $b(R)$ and $\Delta\ell(R)$ for which we obtain linear and hyperbolic fits from the simulation data [see dashed lines in Figure 2.6(a)] as

$$b(R)/\lambda = 1.73R/\lambda + 0.78/\lambda, \quad (2.11)$$

$$\Delta\ell(R)/\lambda = 4.29/R/\lambda - 0.93/\lambda. \quad (2.12)$$

After all one can then treat a pair effectively as a rectangular block of length $\ell + \Delta\ell(R)$ and width $b(R) + \lambda$. Since the block now contains two particles, the instability density for the doublet-vortex state now reads

$$\eta_2(R) = 2\eta_0 \left(\frac{\ell}{\ell + \Delta\ell(R) + b(R) + \lambda} \right)^2. \quad (2.13)$$

In Figure 2.6(b) both instability lines obtained from either equation (2.10) or (2.13) are shown. The simulated state diagram from Figure 2.2(a) is plotted as a reference. Given the simplifications entering in our instability theory, the transition lines describe the simulation data reasonably well. Moreover, the reentrance effect of the slowed rotor fluid is well captured by our instability analysis such that the topology of the phase diagram is predicted correctly by the theory.

We finally remark that our instability analysis also sheds light on the stability of the singlet- and doublet-vortex states for parameter combinations different from those used in our simulation study. For example, one important condition is that the aspect ratio of the swimmers is high since the reference system in the theory consists of infinitely thin hard needles. This implies that no multiplet-vortex states are expected for almost spherical swimmers.

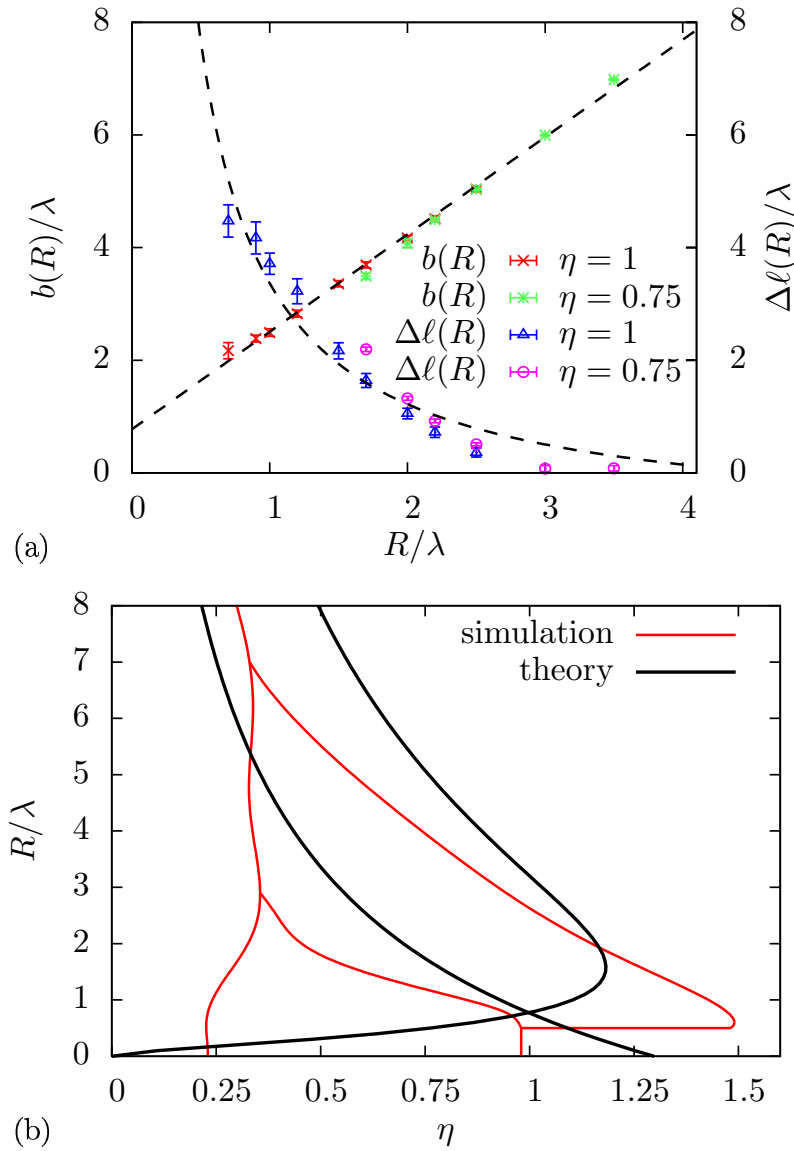


Figure 2.6.: (a) Spatial extent of the circle swimmer pairs in the doublet vortex state as characterized by the width b and the extended length $\Delta\ell$ as a function of the swimming radius R for different densities $\eta = 0.75$ and $\eta = 1$. (b) Instability lines for the singlet and doublet vortex state as obtained from our analysis. The simulated state diagram is shown as a reference.

2.4. Conclusions

We have studied the collective dynamical behavior of a simple two-dimensional model of circle-swimming rigid rods by computer simulation. A new vortex array formation was found

where a vortex is composed of a circle swimmer pair, which we referred to as a doublet-vortex state.

The results obtained in our modeling of circle swimmers can be verified in experiments of circle swimmers on two-dimensional substrates. An ideal realization for our model consists of such colloidal rods that are catalytically driven from one side such that they perform strong circular swimming. The swimming radius can in principle be tuned by the lever arm length of the spot where the catalytical reaction happens. The same idea can be used for thermally driven rodlike particles as proposed in Ref. [124]. It is, however, essential to use slender rodlike particles in order to obtain the singlet- and doublet-vortex states. As documented by our theoretical approach, almost spherical particles with a low aspect ratio are not expected to show these vortex states.

For the future, it would be interesting to explore other physical shapes of the swimmer such as recently explored L -particles [59] or C -particles² that have a strong tendency to form stacks [162]. We expect that the pairing process will be significantly disturbed for a different particle shape. For such nonconvex particle shapes, it is possible that multiplet-vortex states arise, which comprise an even higher number of swimmers.

Further theoretical efforts should be aimed at expanding the model and equations of motion step by step by considering effects that are relevant in experiment such as multi-body hydrodynamic interactions and flexibility of particle shape. The effect of finite temperature could be incorporated as well if one wishes to assess the effect of translation and rotational noise (e.g., tumbling in bacteria) in more detail. In fact, previous studies [154] have already shown that the results are stable with respect to noise provided the strength of the noise is not too large. We have confirmed the stability for some selected parameters also for the doublet-vortex state. It is also desirable to explore the model in three spatial dimensions where the swimming path is a helix rather than a circle [163]. Finally, it would be challenging to construct microscopic theories that are capable of predicting the observed emergent states advanced in this study. Dynamical density functional theory for anisotropic systems [130, 164, 165] might provide a promising avenue for this.

Acknowledgments

We thank Henricus H. Wensink for helpful discussions. This work was financially supported by the ERC Advanced Grant INTERCOCOS (Grant No. 267499) and by the DFG within SFB TR6 (Project D3).

²A recent numerical study shows the emergence of spinning rotor clusters for C -shaped self-propelled particles [87].

Capturing self-propelled particles in a moving microwedge

With an appropriate use of a fishing net, many fish can be simultaneously caught in an efficient way. There are two different strategies to catch fish using, e.g., a cone-shaped net; the net can either be dragged through quiescent water or a stationary trap (a so-called “fyke”) can be placed in running water, forcing the fish to swim into the fyke. While the general methods for trapping macroscopic swimming organisms (fish) have been known since ancient times [166], the corresponding problem in the microscale has been scarcely explored thus far due to the general difficulty in controlling and designing processes in systems of micron-sized objects. There are many realizations of microscopic swimmers [40, 94–96] including autonomously navigating microbes [107, 108, 111, 118, 119, 135–139, 167] and human-made artificial swimmers [37, 38, 44, 50, 58, 59, 123, 125–127, 146, 147, 168, 169]. For many applications it is of key importance to trap collections of these active particles into a moving trap. A first application is to transport ensembles of swimmers to a given destination like a cargo. This situation differs from the more commonly considered case in which the swimmer itself transports an inert cargo [170–174]. It is obvious that, in the former situation, one, first, has to catch the particles in an efficient and controlled way before they can be transferred to the specific destination via a moving trap. A second application could be to efficiently remove “dangerous” toxic particles in order to clean the environment [175, 176]. Moreover, the motion of the trap is expected to play a crucial role in optimizing the removal of contaminating mesogens.

Apart from the different length scale, it is important to note that another basic difference between macroscopic fish and microbes is their Reynolds number Re , which characterizes the ratio of inertial to viscous forces associated with swimming. While fish typically swim at a Reynolds number of several hundred, microswimmers typically operate at very low Reynolds numbers, $Re \ll 1$.

In this chapter, we transfer the ideas of catching fish in a net to micron-sized self-motile particles propagating through a solvent at a low Reynolds number. We use computer simulations

This chapter has been published in a very similar form by Andreas Kaiser, Katarina Popowa, Henricus H. Wensink, and Hartmut Löwen, *Phys. Rev. E* **88**, 022311 (2013), see Reference [2].

of a two-dimensional system of self-propelled rods and drag a chevron-shaped obstacle with a constant speed v through the embedding active fluid. As revealed by a simple Galilean transformation, this setup is equivalent to a static trap in a flowing solvent. Our simulations complement earlier studies for a static trap [5] where a wedge was found to optimize the catching efficiency. Here, we focus on the effect of a nonzero drag speed. At fixed swimmer density and varied drag velocity v and apex angle of the trap, there are three emerging states corresponding to no trapping, partial trapping, and complete trapping. While in the no-trapping state, no particles remain in the trap over time, in the complete trapping state all swimmers are permanently caught in the microwedge after a certain amount of time. Finally, partial trapping refers to a state where only a fraction of the particles are permanently trapped. Obviously, the dream of any fishermen and the most desirable situation in many applications is the complete-trapping state, where no freely moving particles are left.

We solve the single-rod case analytically and present the trapping state diagram in the plane spanned by the opening angle α of the microwedge ($0 < \alpha \leq \pi$) and the trap velocity v (normalized by the swimmer velocity v_0). The drag direction is along the symmetry axis of the wedge and we define a positive drag speed if its drag is along the inner part of the wedge. As a result, if the net is dragged into the positive direction, trapping is facilitated. Counterintuitively, however, for a negative drag velocity, a situation of no trapping can change into a trapped one, which we attribute to polar ordering of the swimmer along the wedge symmetry axis. Clearly, when the (negative) trap velocity exceeds the swimmer velocity ($v/v_0 < -1$), trapping is no longer possible as the trap overtakes the swimmer, which leads to a reentrant effect for increasing negative velocity: for intermediate opening angles α , we observe the state sequence of no trapping, complete trapping, and no trapping. For finite trap density we employ computer simulations [5, 130, 177] and confirm the trends of single-particle trapping. For high-enough positive drag speed, a partial trapped situation will change into a complete trapped situation. In the converse case of a negative trap velocity, the reentrance effect is amplified by a collective polar ordering in the trap. This is a typical example of self-assembly of self-propelled colloidal rods [178] directed by the moving microwedge. Previous studies analyzing the rectification effect of a wall of funnels by experiments [29, 179], theory [180], and simulation [181–184] have utilized similar chevron-shaped boundaries but have never focused on trapping¹.

Apart from their relevance for applications, our predictions can be verified in experiments on rodlike microbes and self-propelled colloids and granulates [103, 179, 188–190]. Typically, the system is moving on a two-dimensional substrate or can be subject to a strong two-dimensional confinement [76]. A chevronlike trap can be prepared by lithographic techniques [58, 116, 168, 191] and it can be dragged at will using optical tweezers [124, 192]. Therefore, an experimental realization of our model is conceivable. We further anticipate that the same effects occur also in three dimensions where the corresponding generalization of the wedgelike trap is a hollow cone, similar in spirit to a real fishing net.

This chapter is organized as follows: in Section 5.1 we introduce the model and explain the simulation method. Section 3.2 is devoted to the case of a single self-propelled rod. We will

¹In the meantime there a couple of studies focussing on the trapping of active swimmer due to boundaries, e.g. [185–187].

give a theoretical prediction of the trapping state diagram along with numerical results. In Section 3.3, we investigate the trapping states for many particles and all three main control parameters. In particular, we fix each time one of these, vary the others and obtain a full trapping state diagram which can be explained by the effects already showing up for the single particle case. Finally, we conclude in Section 5.4.

3.1. Model

The aim is to formulate a minimal collision-based model for self-propagating rod-shaped particles that is capable of capturing the generic features of interacting swimmers at intermediate to high particle density and their collective response to mobile confining boundaries. Following earlier studies [5, 86], our system consists of N rigid rods of length ℓ , each moving in the overdamped limit with a propagation velocity v_0 arising from a formal force F_0 fixed along the longitudinal rod axis $\hat{\mathbf{u}}$ [86, 130]. The rodlike swimmers are modelled via the Yukawa segment model, introduced in Section 1.4. A trap is introduced as a boundary with a prescribed shape and contour length ℓ_T and is dragged with a velocity v through the system. Particle-trap interactions are implemented by discretizing the trap boundary into $n_T = \lfloor \ell_T/d \rfloor$ equidistant segments² each interacting with the rod segments via the same Yukawa potential, resulting in the pair potential

$$U_{\alpha T} = U_0 \sum_{i=1}^n \sum_{k=1}^{n_T} \frac{\exp[-r_{ik}^{\alpha T}/\lambda]}{r_{ik}^{\alpha T}}. \quad (3.1)$$

Here $r_{ik}^{\alpha T}$ denotes the distance between segment i of rod α and segment k of the trap. The net is dragged with imposed velocity $\mathbf{v} = v\mathbf{x}$ along the symmetry axis of the wedge according to

$$\mathbf{r}_k = \mathbf{v}t, \quad (3.2)$$

where \mathbf{r}_k denotes the position of the k th segment of the trap. Mutual self-propelled rod collisions generate apolar nematic alignment which stimulates swarm formation at finite concentrations [103]. The wedge boundary mimics a hard wall and imparts 2D planar order with rods pointing favorably perpendicular to the local wall normal.

The microscopic equations of motion for the center-of-mass position $\mathbf{r}_\alpha(t)$ and orientation $\hat{\mathbf{u}}_\alpha(t) = (\cos \varphi_\alpha(t), \sin \varphi_\alpha(t))$ of the self-propelled particles emerge from a balance of the forces and torques acting on each rod α and are similar as described in Ref. [86]

$$\mathbf{f}_T \cdot \partial_t \mathbf{r}_\alpha = -\nabla_{\mathbf{r}_\alpha} U + F_0 \hat{\mathbf{u}}_\alpha, \quad (3.3)$$

$$\mathbf{f}_R \cdot \partial_t \hat{\mathbf{u}}_\alpha = -\nabla_{\hat{\mathbf{u}}_\alpha} U, \quad (3.4)$$

²Here the segment distance d is equal for both, the swimmers and the trap.

in terms of the total potential energy $U = (1/2) \sum_{\alpha, \beta (\alpha \neq \beta)} U_{\alpha\beta} + \sum_{\alpha, T} U_{\alpha T}$ with $U_{\alpha T}$ the potential energy of rod α with the trap and $\nabla_{\hat{\mathbf{u}}_\alpha}$ denotes the gradient on a unit circle. The one-body translational and rotational friction tensors \mathbf{f}_T and \mathbf{f}_R can be decomposed into parallel f_{\parallel} , perpendicular f_{\perp} and rotational f_R contributions as shown in Section 1.4.

Equation (3.4) neglects thermal or intrinsic Brownian noise [73], which is acceptable at intermediate to high concentrations when particle collision dominate the dynamics [76]. Despite its minimal nature, the self-propelled rod model provides a remarkably accurate description of the velocity statistics and microstructure of dense active matter [76].

It is important to note that our system is strictly equivalent to a quiescent net where the swimmers all experience their propagation velocity \mathbf{v}_0 together with an added velocity $-\mathbf{v}$. This can easily be demonstrated by transforming the equation of translational motion equation (3.3) in terms of reduced difference coordinates $\tilde{\mathbf{r}}_\alpha = \mathbf{r}_\alpha - \mathbf{v}t$, i.e., by applying a *Galilean transformation* [193] so:

$$\partial_t \tilde{\mathbf{r}}_\alpha = (v_0 \hat{\mathbf{u}}_\alpha - \mathbf{v}) - \mathbf{f}_T^{-1} \cdot \nabla_{\tilde{\mathbf{r}}_\alpha} U. \quad (3.5)$$

The typical self-propulsion speed of a free single self-propelled rod

$$v_0 = \frac{F_0}{f_0 f_{\parallel}} \quad (3.6)$$

defines the time interval

$$\tau = \frac{\ell}{v_0} \quad (3.7)$$

a rod needs to swim a distance comparable to its size. In the following, distances are measured in units of ℓ and energy in units of $F_0 \ell$.

We simulate self-propelled rods with aspect ratio $a = 10$, using $n = 11$ segments, in a square simulation box with area A and periodic boundary conditions in both Cartesian directions. A particle packing fraction is defined as $\phi = N\sigma/A$ with $\sigma = \lambda(\ell - \lambda) + \lambda^2\pi/4$ the effective area of a single rod. In the bulk density range $\phi < 0.2$ the self-propelled rods spontaneously form flocks with strong spatial density fluctuations [194]. We subject the self-propelled rods to a mobile chevron boundary with contour length $\ell_T = 20\ell$ and variable apex angle $0^\circ < \alpha < 180^\circ$, leading to an occupied trap area $A_0 = (\ell_T^2/8) \sin \alpha/2$, which is dragged with velocity v (see Figure 4.1). In the macroscopic limit, the system can be interpreted as a reservoir of microswimmers exposed to an equidistant array of mutually independent wedges. A reduced trap density is defined by $\phi_T = (\ell_T^2/8A)$ which fixes the number of rods via $N = (\ell_T^2/8\sigma)(\phi/\phi_T)$. We constrain $\phi_T = 0.031 < 0.1$ in order to guarantee the microwedges to be completely independent of each other within the typical range of bulk rod packing fractions $0 < \phi < 0.1$ considered here. The latter density is one of our main steering parameters. There are also the drag velocity which is in the range of $-1.2v_0 < v < 8v_0$ and the apex angle α of the microwedge.

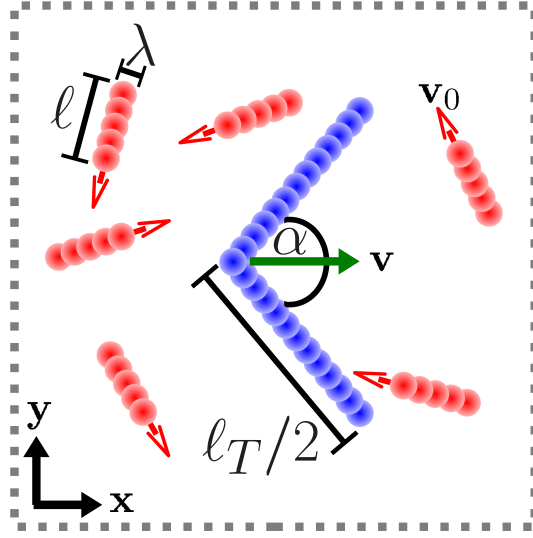


Figure 3.1.: Sketch of the system of self-propelled rods with aspect ratio $a = \ell/\lambda$ and a self-motile velocity \mathbf{v}_0 directed along the main axis $\hat{\mathbf{u}}$ (red arrows) of each rod at bulk density ϕ . The single Yukawa segments are shown as red spheres. A mobile wedge (indicated by blue spheres) with contour length ℓ_T and an apex angle α is dragged with a constant velocity \mathbf{v} (green arrow). Periodic boundary conditions in both Cartesian directions are indicated by dotted lines.

Initial configurations are generated from a rectangular lattice of aligned rods with $\hat{\mathbf{u}}$ pointing randomly up or down. The rods are randomly displaced from the initial lattice such that the starting configuration bears already some randomness. The segments of the microwedge are successively placed in the system to avoid overlapping rods. We simulate the whole system for a time of at least $t_s = 15000\tau$.

3.2. Trapping a single swimmer in a mobile microwedge

We first focus on a single swimmer for which analytical results can be obtained which we test against our computer simulations. In Figure 3.2(a), simulation results and analytical formulas for the trapping state diagram are combined. The main control parameters we vary are the reduced trap drag velocity v/v_0 and the apex angle α . The trapping scenario of a single swimmer is generic and is independent of the contour length of the net, as long as $\ell_T \gg \ell$, and the aspect ratio of the rod-shaped swimmer. In the simulation, a particle is considered to be trapped if it remains inside the wedge for at least $t^* = 10^3\tau$.

Let us, first, discuss some limiting cases which are all intuitive: For strongly negative drag velocities, $v/v_0 < -1$, the swimmer is slower than the microwedge and therefore can never get trapped for any opening angle α . Conversely, for $v/v_0 > -1$ and very small opening angles,

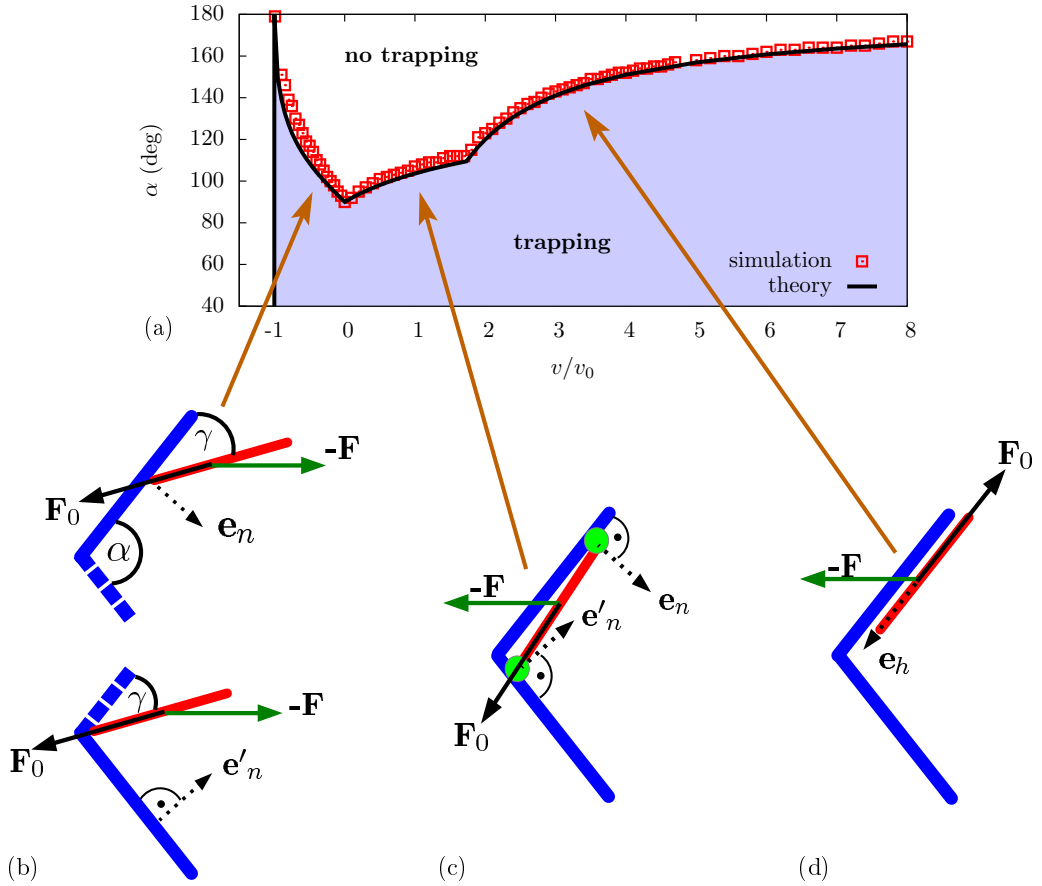


Figure 3.2.: (a) Trapping state diagram for a single self-propelled rod in the plane of reduced drag velocities v/v_0 and net apex angles α . The shaded region marks the trapping regime. The dots represent simulation results for the trapping-no trapping boundary while the solid line contains the analytical predictions. Different trapping mechanisms are sketched in (b)–(d). For more details, see text. Points of contact of the swimmer and the microwedge are highlighted by light green circles.

once a rod enters the moving net it is faster than the net and therefore will approach to the kink of the wedge, where it remains because it cannot escape by turning around. Hence there is a trapping state for $v/v_0 > -1$ and small opening angles. Complementarily, for $v/v_0 > -1$ and very large opening angles ($\alpha \approx \pi$), if the rod enters the microwedge, it will just slide along the wall of the wedge and will then pass over the slight kink of the wedge such that the rod leaves the trap again. Consequently, the rod does not permanently reside in the wedge and, thus, attains a no-trapping state.

As shown in Figure 3.2(a), the intermediate transition opening angle which separates the trapping from the no-trapping regime is a marked function of the reduced trap velocity which exhibits some cusps. The cusps occur at $v/v_0 = -1$, $v/v_0 = 0$, and $v/v_0 = \sqrt{3}$ and clearly distinguish four different situations which we now discuss quantitatively step by step. We

use the frame of the resting net for this discussion and introduce forces instead of velocities. Clearly forces are proportional to velocities. In the microwedge system, the rod center experiences a force $\mathbf{F}_0 \propto \mathbf{v}_0$ governing its self-propulsion plus another force $-\mathbf{F} \propto -\mathbf{v}$ arising from the resting rod frame. Third, the wall possibly exerts at contact a force \mathbf{F}_N onto the rod which is always normal to the wall.

As already stated above, for strongly negative drag velocities, $v/v_0 < -1$, a swimmer moves slower than the microwedge and therefore can never get trapped. For $-1 < v/v_0 < 0$, it is expected that single rods are still spilled out by the net, but the opposite behavior is true: trapping becomes more efficient if the drag speed approaches the swimmer speed $v/v_0 \rightarrow -1^+$ from above. This counter-intuitive behavior can be understood as sketched in Figure 3.2(b). If a rod enters the trap and hits a wall (see upper sketch of Figure 3.2(b)), it will orient at an angle γ . This angle is determined by the condition that the projection of $\mathbf{F}_0 - \mathbf{F}$ onto the wall normal has to vanish, $(\mathbf{F}_0 - \mathbf{F}) \cdot \mathbf{e}_n = 0$, with the wall normal vector $\mathbf{e}_n = (\sin \alpha/2, -\cos \alpha/2)$. This leads to $\gamma = \arcsin(v/v_0)$. With this orientation, the rod will slide along the wall inside the corner until it touches the lower wedge wall [see lower sketch of Figure 3.2(b)]. The threshold condition whether the rod slides further outside the wedge along the lower wall is finally given by requiring that the normal projection along the lower wall normal $\mathbf{e}'_n = (\sin \alpha/2, \cos \alpha/2)$ vanishes, i.e.: $(\mathbf{F}_0 - \mathbf{F}) \cdot \mathbf{e}'_n = 0$. This all leads to the threshold condition

$$\alpha = \frac{\pi}{2} - 2 \left(\arcsin \left(\frac{v}{\sqrt{2}v_0} \right) - \arcsin \left(\frac{v}{v_0} \right) \right). \quad (3.8)$$

which is plotted as a solid line in Figure 3.2(a). This implies that a trap moving into the negative direction orients the rods along the wedge symmetry axis and thus keeps them inside, thereby enhancing the trapping efficiency.

In the case of positive drag velocities, two different trapping mechanisms can occur. The first mechanism is shown in Figure 3.2(c). Here the swimmer enters into the wedge and is stuck close to the wedge cusp with two contact points, one at the higher and another at the lower wall. This hinders the rod in rotating further such that it gets immobilized. The contact points are indicated in Figure 3.2(c). In this situation, the rod experiences four different forces, two arising simultaneously from the wall normals plus $\mathbf{F}_0 - \mathbf{F}$. The normal wall forces are unknown but determined by the joint conditions of the vanishing total force and the torque acting on the rod center which characterize the transition from no trapping to trapping. Hence, these conditions are $\mathbf{F}_0 - \mathbf{F} + \mathbf{F}_n + \mathbf{F}'_n = 0$ and $F_n \mathbf{e}_h \times \mathbf{e}'_n + F'_n \mathbf{e}_h \times \mathbf{e}_n = 0$. Eliminating the unknown normal forces, we obtain the threshold criterion

$$\frac{v}{v_0} = -\cos \left(\frac{\alpha}{2} \right) + \frac{\sin^4(\alpha/2)}{\cos^3(\alpha/2)}. \quad (3.9)$$

The second mechanism is shown in Figure 3.2(d) and refers to a situation where an aligned rod intends to leave the trap, for example when it was able to turn in the kink. If the projection of $-\mathbf{F}$ tangential to the wall exceeds the self-propulsion, the moving microwedge surpasses

the rod and keeps it caught. The condition for the threshold for this second mechanism is, therefore $\mathbf{F} \cdot \mathbf{e}_h = F_0$ for $\mathbf{e}_h = (-\cos \alpha/2, -\sin \alpha/2)$ which yields

$$\cos\left(\frac{\alpha}{2}\right) = \frac{1}{v/v_0}. \quad (3.10)$$

As can be shown easily, this second mechanism surpasses the former mechanism for dragging velocities $v/v_0 > \sqrt{3}$.

Summarizing, a single self-propelled particle can always be trapped for $v > -v_0$ and $\alpha < 90^\circ$. For apex angles larger than 90° and increasing trap velocities, the following sequence of states is found: no trapping, trapping, no trapping, and trapping. This clearly demonstrates the nontrivial interplay between wedge geometry and orientational coupling to the rod. Moreover we find for positive drag velocities two different mechanisms which hold the particles inside the microwedge³. Finally, the good agreement of the threshold lines between analytical theory and simulations shows that the segment model used in this thesis reproduces well the purely geometric conditions of steeply repulsive interactions.

3.3. Collective trapping

3.3.1. Static microwedge

Let us, first, briefly recapitulate previous results [5] for a static trap ($v = 0$). The trapping state diagram now drawn in the parameter space spanned by the wedge apex angle α and reduced rod packing fraction ϕ_R at fixed net densities is shown in Figure 3.3, including characteristic snapshots.

Following earlier work [5], we consider a rod α trapped if its velocity $v_\alpha = |\mathbf{v}_\alpha| < 0.1v_0$ for a time interval $t^* = 25\tau$. In contrast to the single particle case we now have to distinguish between two different kinds of trapped states. These are characterized by the fraction of trapped particles $x_T = N_T/N$ which acts as some kind of order parameter for the different states. Either no particle is trapped, $x_T = 0$ (no trapping), or all particles are trapped, $x_T = 1$ (complete trapping), or just a fraction of all particles in the system can be captured by the wedge, $0 < x_T < 1$. This new state will be referred to as partial trapping.

All trapping states can be found in the state diagram for a static microwedge, see Figure 3.3. Evidently, in the case of small apex angles there is only partial trapping since the area of the wedge is too small to accommodate all particles.

Larger apex angles enable complete trapping up to a certain reduced rod density. The resulting triple point is independent of the trap density and attains a value $\phi_R^* \approx 1.3$. Higher densities will show only two different trapping states. While for a single particle and a static microwedge

³See <http://link.aps.org/supplemental/10.1103/PhysRevE.88.022311> for movies showing the occurring trapping mechanisms for the single-particle case.

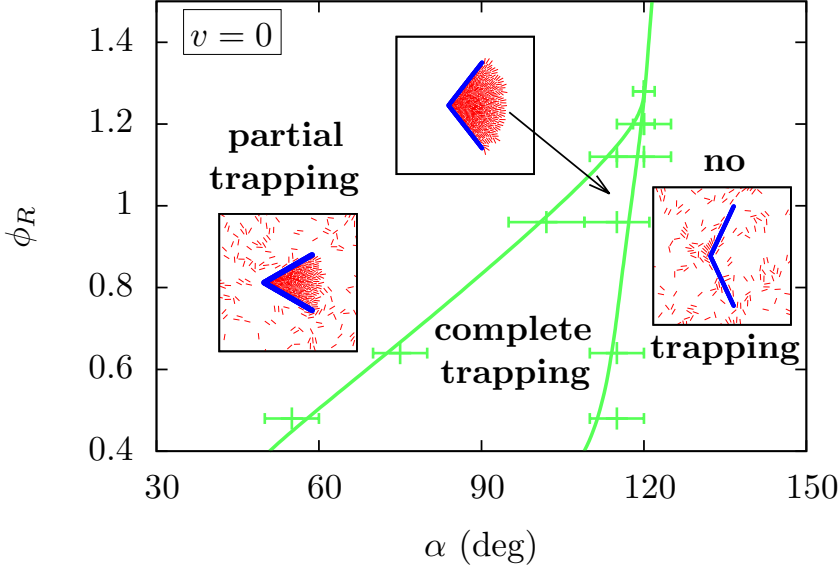


Figure 3.3.: Trapping state diagram in the case of a static trap $v = 0$ denoting three different states for varying apex angles and a reduced self-propelled rod packing fraction. All occurring trapping states are visualized by use of characteristic snapshots using central sections of the simulation box.

a capture is only possible for an apex angle $\alpha < 90^\circ$, an increase of the rod density leads to an increase of the maximum apex angle which allows trapping. Self-propelled rods coherently self-trap at the kink of the trap and jam. Hereby a small immobile cluster can be formed which grows and leads to a filling of the wedge. Therefore, in the studied density regime, a trapping state is possible for apex angles up to $\alpha \approx 120^\circ$. The influence of rotational noise, which may arise from fluctuations in the swimming direction as manifested by *run-and-tumble* motion of swimming bacteria, has been accounted for by adding Gaussian white noise to the equation of rotational motion equation (3.4). No significant effect on the trapping state diagram was found for typical values of the effective rotational diffusivity of bacterial swimmers [5].

3.3.2. Mobile microwedge

We now consider a moving trap. Simulation results for the trapping state diagram in the plane spanned by reduced trap velocity v/v_0 and apex angle α are shown in Figure 3.4 combined with appropriate simulation snapshots characterizing the final state. As a first general finding, the state diagram has the same topology as that for a single rod if one does not discriminate between partial trapping and complete trapping. Of course, the actual numbers for the trapping to no trapping transition are significantly shifted. In particular, the worst case of trapping which occurs at an opening angle of 90° for a static microwedge [see Figure 3.2(a)] is now

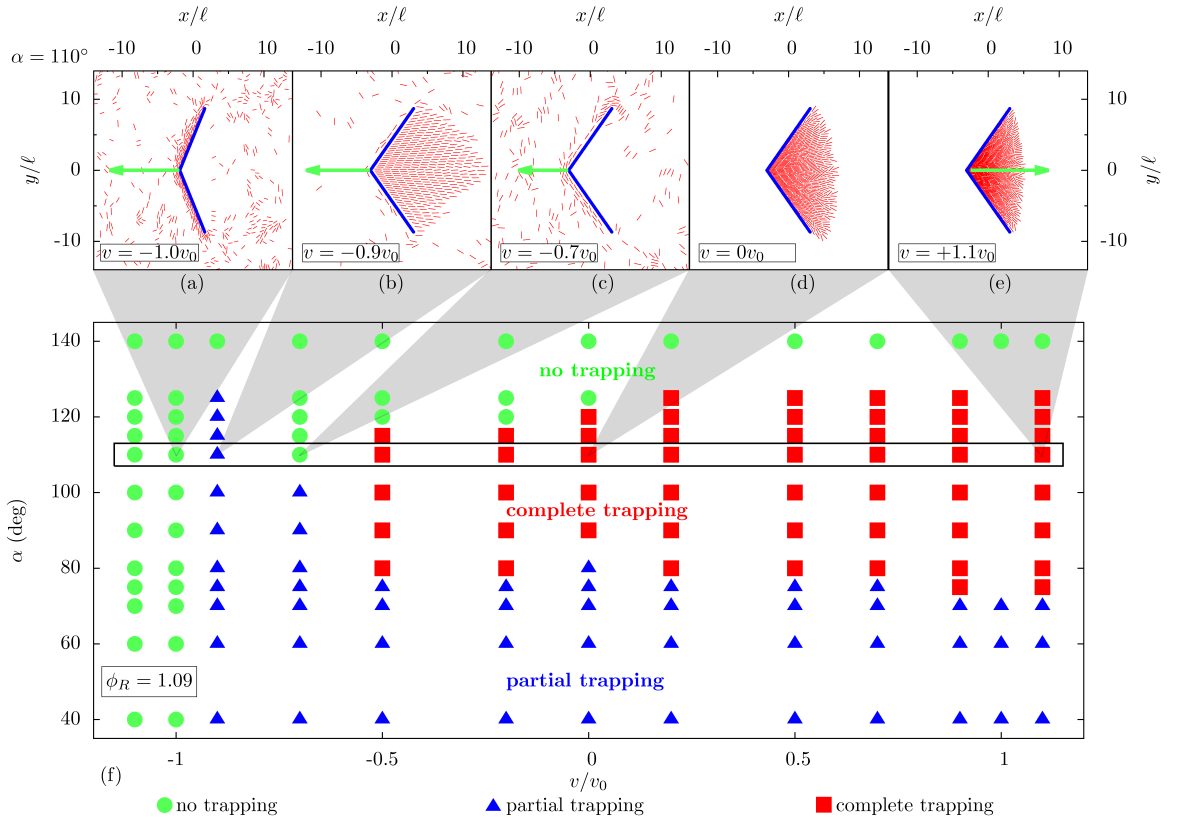


Figure 3.4.: Trapping state diagram and simulation snapshots of the final state at finite rod density $\phi_R = 1.09$. (a) - (e) Simulation snapshots for an apex angle $\alpha = 110^\circ$. The respective dragging velocity of the trap is given in each figure and indicated by a scaled arrow. (f) State diagram showing the three different trapping states in the plane spanned by the reduced net velocity and the trap apex angle α . Circles correspond to no trapping, triangles to partial trapping and squares to complete trapping.

significantly shifted towards an opening angle of about 110° at a negative reduced drag velocity of about -0.7 . A corresponding snapshot of the empty microwedge is shown in Figure 3.4(c).

If the trap velocity is varied at a fixed opening angle of 110° , as indicated by the different snapshots in Figures 3.4(a)-3.4(e), there is an intermediate trapping effect at reduced negative drags close to -1 , as indicated in Figure 3.4(b). In this case, rods can catch up with the moving net to accumulate inside the wedge. This is opposed to strongly negative dragging velocities $v \leq -v_0$, where the wedge is faster than the rods on average, which leads to an accumulation of particles outside the net [see Figure 3.4(a)].

Let us focus on the partial trapping situation of rods which are only slightly faster than the net as shown in Figure 3.4(b). We observe a large swarm following the movement of the net. The structure of the swarm is characterized by a significant degree of nematic (or polar) order which stems from the repulsive rod interactions. The big swarm therefore is a result of rod self-assembly templated by the moving net. The net plays the role of a leader which

guides the swarm. This is an interesting collective effect which can be in principle exploited to control and guide assemblies of active particles at will [152] or to align them dynamically in an efficient way. Qualitatively, the tendency of alignment can be seen from only a single rod [see Figure 3.2(b)] which tries to orient along the drag direction. The rod interaction, however, dramatically increases the alignment, leading to a large orientated swarm.

Further increasing positive drag speed will compress the trapped particles, leading to a larger number density of the captured particles inside the net. Therefore, at higher speeds, the threshold to a no-trapping state is shifted towards larger opening angles.

We now focus on the transition line between partial trapping and complete trapping; see the squares and triangles in Figure 3.4(f). At fixed opening angle (say at about 80°), this line also shows an interesting reentrance effect for increasing drag velocities as embodied in the highly nontrivial state sequence of partial trapping - complete trapping - partial trapping - complete trapping. The first transition from partial trapping to complete trapping has to do with the efficient nematization which then becomes less efficient at almost zero drag velocities. The ultimate transition to complete trapping is then an effect of rod compression inside the net for increasing drag velocities. Interestingly, starting with a resting net with opening angles slightly below 90° , the trapping efficiency increases no matter in which direction the microwedge is dragged.

We now characterize the directed self-assembled state more carefully by monitoring the area covered by the trapped particles and the actual nematic order. First we draw a convex hull around all trapped particles which defines an area A_c . We normalize this area to the inside area $A_0 = (\ell_T/8) \sin \alpha/2$ of the wedge. Results for A_c/A_0 as a function of the drag speed are presented in Figure 3.5(a) at fixed opening angle α . In line with the huge nematic wake discussed earlier, the ratio A_c/A_0 vastly exceeds unity for negative drags close to $-v_0$. In fact, A_c/A_0 has a maximum as a function of v/v_0 , which points to a very efficient wake area that contains particles which are dragged through the liquid by the moving wedge.

Second, we analyze the degree of nematic ordering in the trapped particles by calculating the average

$$S = \langle 2 \cos^2 \theta_i - 1 \rangle, \quad (3.11)$$

where θ_i is the angle between the rod orientation of the i th rod and the drag velocity. The average $\langle \dots \rangle$ refers to an average over all captured rods for a variety of different initial configurations. The nematic order parameter S is defined as usual in two spatial dimensions. For a perfect alignment of all trapped rods, $S = 1$, while S vanishes if there is no orientational ordering at all. We relate this quantity S to a perfect cone filling of the rods where the orientational direction is anti-radially towards the origin of the wedge. In this reference situation, the nematic order parameter S_r is given by

$$S_r = \frac{1}{\alpha} \int_{-\alpha/2}^{\alpha/2} (2 \cos^2 \theta - 1) d\theta = \sin \alpha / \alpha. \quad (3.12)$$

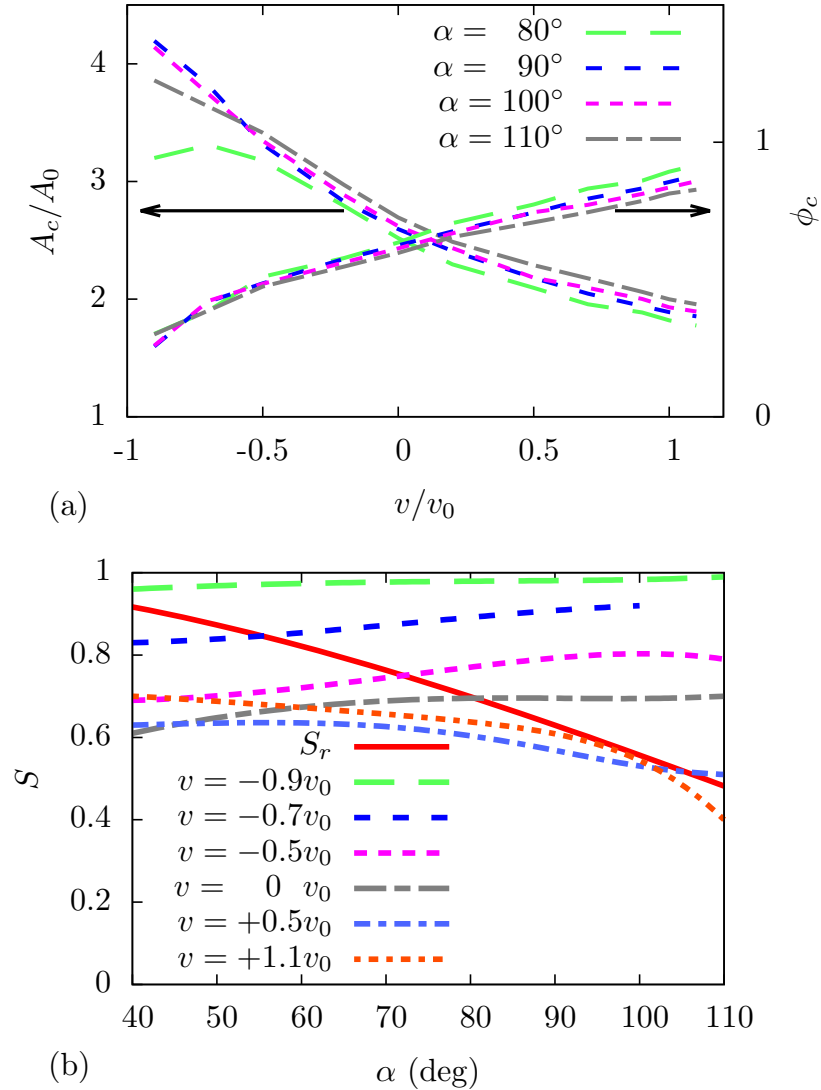


Figure 3.5.: (a) Relative area occupied by captured swimmers A_c/A_0 and resulting packing fraction ϕ_c for $\phi_R = 1.09$ and varying drag velocities for four apex angles. (b) Dependence of the nematic order parameter S on the apex angle for various drag velocities (dashed lines). The reference value S_r for a perfect cone-orientation of the captured rods is given by the solid line.

In Figure 3.5(b), S is shown versus the opening angle for fixed drag speeds. The cone normalization S_r is also given. For the nematic swarm at $v/v_0 = -0.9$, S clearly exceeds S_r . This is inverted for very high positive drags $v > v_0$, where $S < S_r$ holds over the full range of opening angles. This finding can be attributed mainly to particle misorientations at the wedge boundary close to the end of the wedge, see again the snapshot of Figure 3.4(e).

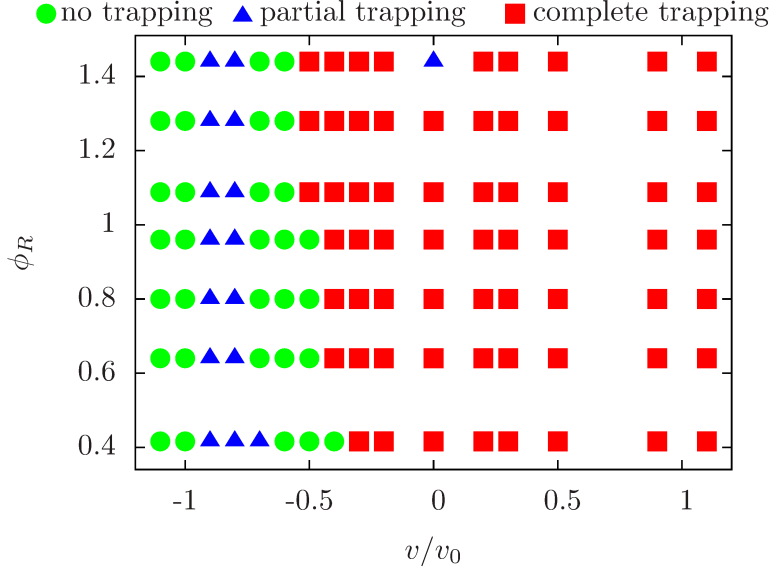


Figure 3.6.: *Trapping states for a fixed apex angle $\alpha = 110^\circ$ and varied rod density ϕ_R and reduced dragging velocity v/v_0 .*

In addition, we consider a system with a fixed apex angle $\alpha = 110^\circ$ and vary the reduced rod packing fraction ϕ_R and the dragging velocity. The data contained in Figure 3.6 show that the dependence on the rod density is weak providing the same state-sequence as for the special rod density selected previously for Figure 3.4(f). Only in the case of extreme rod densities $\phi_R > \phi_R^* = 1.3$ is the area of the net not large enough to accommodate all particles. This leads to a partial trapping state instead of complete trapping as indicated in Figure 3.6 for a static microwedge at high rod densities.

We expect our results to be robust against hydrodynamic far-field interactions, which are expected to be less important for the particle dynamics at high local particle densities, as found inside the trap, due to mutual hydrodynamic screening [195] and the small magnitude of the flows fields generated by the microswimmers [73] and the moving wedge. Moreover, the presence of no-slip trap boundaries in microfluidic devices are expected to strongly suppress hydrodynamic long-range interactions between swimmers due to cancellation effects from the hydrodynamic images [76].

3.4. Conclusions

While there is a considerable amount of detailed knowledge about how to trap macroscopic particles and passive particles in static traps such as colloids using optical tweezers or atoms in a Paul trap, is it much less clear how large numbers of active microscopic particles can be captured in an efficient way. Using computer simulations, we have studied a dragged chevron-

shaped trap which allows us to capture several self-propelled rods in an irreversible manner. A microwedge with variable apex angle α enforces active particles to rectify their swimming direction and stimulates the formation of microscopic cluster which may subsequently act as a nucleus for a fast-growing mesoscopic aggregate of captured rods. We have demonstrated the crucial role of the apex angle and the drag velocity of the trap. A non-zero drag velocity imposes dynamic nematization and layerlike ordering of the clustered rods provided the drag velocity is slightly above $-v_0$ ($v \gtrsim -v_0$). We have highlighted the influence of collective self-trapping by comparing results for many self-propelled rods with the single-particle case. The dramatical collective response of self-propelled rods to a minor change in the boundary shape or drag velocity is remarkable and remains unseen for passive systems exposed to external boundaries or electromagnetic traps.

Collective trapping of ensembles of active particles in moving traps can be verified by experiments using rod-shaped bacteria [160] or driven polar granular rods [120] exposed to geometrically structured boundaries [58, 116, 191]. While the presented results are valid for linearly propagating swimmers, it would be interesting to study a trapping device for several swimmers moving on circlelike pathways⁴ [1, 59, 70, 197]. Furthermore, it would be interesting to exploit the trapping scenarios proposed here to design a trapping device which is capable of extracting swimmers with a specific velocity bandwidth from a mixture of active particles with a strong spread in motility. According to the results in Figure 3.4, such velocity-selective trapping could be envisaged by dragging the net at a judiciously chosen negative drag velocity such as to facilitate templated clustering of a subset of swimmers whose individual motility closely resembles that of the moving net.

An interesting open question is in regard to what extent the details of the propulsion mechanism affect the self-trapping behavior of the rods. In particular, it would be interesting to study whether puller- and pusher-type swimmers exhibit different trapping behaviors. These problems will necessitate the use of more sophisticated simulation schemes [198–200] and bring us also to the question regarding the importance of hydrodynamic near-field interactions [201] which are ignored in our model. Real bacteria are usually propelled by flagella attached to the bacterial body whose internal configuration will presumably change at high bacterial density, under strong confinement or at an obstacle [202]. These flagellar interactions may lead to more specific effects which are neglected in our model but could be included on a coarse-grained level in future studies. In particular, one could introduce a density-dependent microscopic mobility which is known to have a considerable effect on the collective behavior in bulk [203]. Finally, it would be interesting to model the properties of the trapped polar state of rods using continuum elasticity theory following recent efforts in this direction for the wetting behavior of (passive) liquid crystals confined in wedges [204–206].

⁴In the meantime the behavior of circle swimmer interacting with a periodic array of L -shaped obstacles has been studied in [196].

Acknowledgments

We thank J. Tailleur for helpful discussions. This work was financially supported by the ERC Advanced Grant INTERCOCOS (Grant No. 267499) and by the DFG within SFB TR6 (Project No. D3).

4

Transport powered by bacterial turbulence

Suspensions of bacteria or synthetic microswimmers show fascinating collective behavior emerging from their self-propulsion [16, 40, 94, 95] which results in many novel active states such as swarming [84, 111, 121, 131, 207] and “active turbulence” [71, 76, 88, 110, 208–211]. In contrast to hydrodynamic turbulence, the apparent turbulent (or swirling) state occurs at exceedingly low Reynolds numbers but at relatively large bacterial concentrations.

Here we address the question whether one can systematically extract energy out of the seemingly turbulent state established by swimming bacteria and how the bacterial turbulence may power micro-engines and transport mesoscopic carriers through the suspension. A related question is what processes on a scale of an individual swimmer are responsible for the energy rectification from this “active heat bath”.

In our experiments we analyze the motion of a microwedge-like carrier (“bulldozer”) submerged in a suspension of swimming bacteria *Bacillus subtilis*. Experimental studies are combined with particle-resolved computer simulations. A broad span of bacterial densities is examined, ranging from the dilute regime over the turbulent to the jammed state. Due to the activity of the suspension, the bulldozer-like particle is set into a rectified motion along its wedge cusp [179, 181], in contrast to tracers with symmetric shape [116]. Its averaged propagation speed becomes maximal within the turbulent-like regime of collective swimming. Our simulations and experiment indicate that the directed motion is caused by polar ordered bacteria trapped inside the carrier in a region near the cusp which is shielded from outer turbulent fluctuations. The orientation of trapped bacteria yields a double-peaked distribution centered in the direction of the average carrier motion. Consequently, the bacterial turbulence powers efficiently the transport of carriers through the suspension. This finding opens the way to utilize self-propulsion energy of bacteria forming a turbulent active fluid for the purpose of control and powering of mesoscopic engines.

Converting bacterial self-propulsion into mechanical energy has been considered previously for shuttles and cogwheels [87, 174, 188, 189, 212, 213] and for bristlebots, meaning centrimetric rodlike robots [214]. Most of the studies were restricted to low swimmer concentrations

This chapter has been published in a very similar form by Andreas Kaiser, Anton Peshkov, Andrey Sokolov, Borge ten Hagen, Hartmut Löwen, and Igor S. Aranson, *Phys. Rev. Lett.* **112**, 158101 (2014), see Reference [3].

where swirling is absent. While fundamental microscopic mechanisms of energy transduction and interaction with solid walls on a scale of a single bacterium are fairly well understood, see e.g. [73, 136, 215], the role of collective motion has not been elucidated so far. Ref. [117] demonstrated that while the energy generated by individual bacteria dissipates on microscale, the increase in swimming velocity and mass transport due to collective motion is significant. Here we put forward an idea how the collective bacterial swimming (bacterial turbulence) strongly amplifies the energy transduction. Complementarily, in high-Reynolds-number turbulent flows, the motion of suspended inertial particles is not directed [216], lacking a conversion of turbulent fluctuations into useful mechanical work.

4.1. Experiment

Mesoscopic wedge-like carriers were fabricated by photolithography [189, 217]. We mixed a liquid photoresist SU-8 with micron-size magnetic particles before spin coating. This allows to control the orientation of the carriers with an external magnetic field applied parallel to the fluid surface. The arm length of the wedge-like carriers is $L = 262 \mu\text{m}$ (see Figure 4.1), and the wedge angle is 90° . Experiments were conducted on a suspension of *Bacillus subtilis*, a flagellated rod-shaped swimming bacterium $\ell \sim 5 \mu\text{m}$ long and $0.7 \mu\text{m}$ wide. The suspension of bacteria was grown for 8–12 hours in Terrific Broth growth medium (Sigma Aldrich). To monitor the concentration of bacteria during the growth phase, we continuously measured the optical scattering of the medium using an infrared proximity sensor. At the end of the exponential growth phase the bacteria were washed and centrifuged to achieve the desired concentration. Then a small drop of concentrated bacterial suspension was placed between four movable fibers and stretched up to the thickness of $\sim 100 \mu\text{m}$ (see Ref. [108]). Both surfaces of the free-standing liquid film were exposed to air, significantly increasing the oxygen diffusion rate into the bulk of the film. According to our previous study [71], a relatively high concentration of oxygen is required for bacterial motility in concentrated suspensions of *Bacillus subtilis*. We measured the bacteria concentration (or, equivalently, three-dimensional volume fraction) by means of optical coherence tomography (see Ref. [218]) before and after the experiments in order to monitor the effect of film evaporation. This revealed that evaporation is negligible in the course of our relatively short experiment.

Two pairs of orthogonal Helmholtz coils were used to create a uniform magnetic field in the bulk of the liquid film. The carrier was carefully inserted in the film by a digital micropipet. In the course of our experiment, the orientation of the magnetic carrier was reversed every 20 s to prevent migration of the carrier out of the field of view¹. We also confirm that the average speed of the wedge does not depend on the direction of the motion. The influence of gravity was negligible in our experiment. The motion of the wedge was captured by a digital high-resolution microscope camera [Figure 4.1(a)] for the duration of 2 – 4 min. Both

¹See <http://link.aps.org/supplemental/10.1103/PhysRevLett.112.158101> for movies from the experiment and the simulation.

displacement and orientation of the carrier were tracked by a custom-designed software based on Matlab toolboxes.

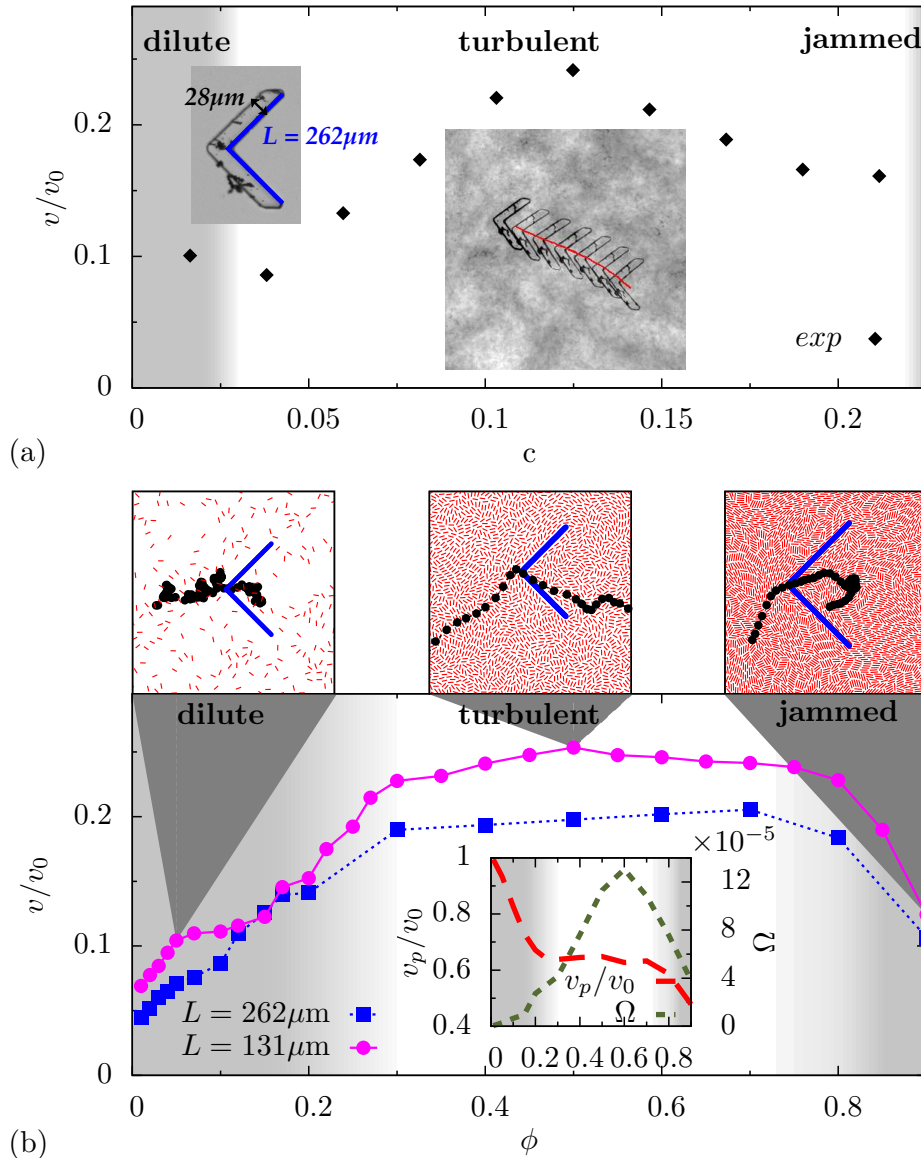


Figure 4.1.: (a) Experimental carrier speed v/v_0 as a function of the bacterial 3D volume fraction c . The insets show the temporal progress of the carrier positions (right) as well as a snapshot of the carrier (left) indicating the characteristic spatial dimensions and the schematic representation (blue line). (b) Numerically obtained transport speed for varying swimmer concentration ϕ and carriers of two different contour lengths: $L = 262\mu\text{m}$ (squares) corresponding to the experimental size of the carrier and half the length $L = 131\mu\text{m}$ (circles). Magnitude of vorticity Ω and averaged bacterial swimming speed v_p/v_0 for various concentrations are shown in the inset.

4.2. Model

We model the bacteria by rod-like objects with repulsive interactions and an effective self-propulsion using parameters matching the experimental conditions. More specifically, the excluded volume interaction between the rods is described by n ‘‘Yukawa’’ segments positioned equidistantly with the distance $d = 0.85 \mu\text{m}$ along a stiff axis of length ℓ , i.e., a repulsive Yukawa potential is imposed between the segments of different rods [75]. However, in order to properly take into account collisions between the bacteria, an important modification is introduced in the model compared to that of Ref. [76]. Experiments [73, 108, 219] demonstrated that two bacteria swim away from each other after the collision. This effect results in a suppression of clustering for small and moderate bacteria concentrations. However, in previous simulations [76], the bacteria had a propensity to swim parallel after the collision and to form dense clusters with a smectic-like alignment. In order to describe the experimentally observed swim-off effect and the resulting suppression of clustering, we incorporate an asymmetric effective bacterial shape² by enlarging the interaction prefactor of the first segments of each rod with respect to the other segments by a factor of 3. The resulting total interaction potential between a swimmer pair α, β is then given by $U_{\alpha\beta} = \sum_{i=1}^n \sum_{j=1}^n U_i U_j \exp[-r_{ij}^{\alpha\beta}/\lambda]/r_{ij}^{\alpha\beta}$ with $U_1^2/U_j^2 = 3$ ($j = 2 \dots n$), where λ is a screening length obtained from the experimental effective rod aspect ratio $\ell/\lambda = 5$, and $r_{ij}^{\alpha\beta} = |\mathbf{r}_i^\alpha - \mathbf{r}_j^\beta|$ is the distance between segment i of rod α and segment j of rod β ($\alpha \neq \beta$). The carrier is implemented correspondingly by tiling the wedge-like contour with length $L = 262 \mu\text{m}$ [see Figure 4.1(a)] with Yukawa segments. The ratio L/ℓ is matched to the experimental situation. For comparison we also perform simulations for smaller arm lengths. The self-propulsion is taken into account via a formal effective force F_0 acting along the rod axis $\hat{\mathbf{u}} = (\cos \varphi, \sin \varphi)$. By imposing a large interaction strength $U_j^2 = 2.5F_0\ell$, we ensure that the bacteria and the wedge do not overlap. The model neglects long-range hydrodynamic interactions between the swimmers. These interactions do not change the overall morphology of the bacterial flow. The most noticeable effect of the hydrodynamic interactions is a seven to ten fold increase of the collective flow velocity compared to the speed of individual bacteria [107, 108]. Certainly, this phenomenon cannot be attained by our model and would require proper incorporation of the hydrodynamic forces.

Since bacterial swimming occurs at exceedingly low Reynolds numbers, the overdamped equations of motion for the positions and orientations of the rods are

$$\mathbf{f}_{\mathcal{T}} \cdot \partial_t \mathbf{r}_\alpha(t) = -\nabla_{\mathbf{r}_\alpha} U + F_0 \hat{\mathbf{u}}_\alpha(t), \quad (4.1)$$

$$\mathbf{f}_{\mathcal{R}} \cdot \partial_t \hat{\mathbf{u}}_\alpha(t) = -\nabla_{\hat{\mathbf{u}}_\alpha} U. \quad (4.2)$$

Here, $U = (1/2) \sum_{\alpha, \beta (\alpha \neq \beta)} U_{\alpha\beta} + \sum_\alpha U_{\alpha<}$ is the total potential energy, where $U_{\alpha<}$ denotes the interaction energy of rod α with the carrier. (In general, a subscript $<$ refers to a quantity associated with the wedge-like carrier.) The one-body translational and rotational friction

²Recently, the impact of the body shape asymmetry of the swimmers on the transport efficiency of a micro-wedge has been studied in Ref. [8].

tensors for the rods \mathbf{f}_T and \mathbf{f}_R can be decomposed into parallel f_{\parallel} , perpendicular f_{\perp} , and rotational f_R components which depend solely on the aspect ratio ℓ/λ , see Section 1.4, and are taken from Ref. [77]. The resulting self-propulsion speed of a single rod $v_0 = F_0/f_{\parallel}$ is matched to the experimental value $15 \mu\text{m/s}$ [108] leading to the time unit $\tau = \ell/v_0$. Since at a relatively large bacteria concentration thermal fluctuations and tumbling are not important, we neglect all stochastic noise terms (our experimental studies in Ref. [71] showed that tumbling of *Bacillus subtilis* becomes significant only for very low oxygen concentrations). Moreover, details of the hydrodynamics between the bacteria and the air-water interface are neglected. According to the experiment, the motion of the carrier is mostly translational and induced by the carrier-bacteria interactions. The hydrodynamic friction tensor $\mathbf{f}_{<}$ of the wedge is calculated for the specific geometry with the dimensions shown in the sketch (left inset) in Figure 4.1(a). For this purpose, the shape of the carrier is approximated by a large number of beads that are rigidly connected. The corresponding hydrodynamic calculations based on the Stokes equation for the flow field around a particle at low Reynolds number are performed with the software package HYDRO++ [220, 221].

The resulting equation of motion for the carrier is

$$\mathbf{f}_{<} \cdot \partial_t \mathbf{r}_{<}(t) = -\nabla_{\mathbf{r}_{<}} \sum_{\alpha} U_{\alpha<}(t). \quad (4.3)$$

We simulate $N \sim 10^4$ rods and a single carrier in a square simulation domain with the area $A = (3L/\sqrt{2})^2$ and periodic boundary conditions in both directions. The dimensionless packing fraction $\phi = N\lambda\ell/A$ corresponds to the bacterial volume fraction c in the experiments.

4.3. Transport of a wedgelike carrier

The shape reflection symmetry of the wedge around its apex will exclude any averaged directed motion perpendicular to the apex while there is no such symmetry in the apex direction. Hence, due to rectification of random fluctuations, the carrier will proceed on average along its cusp. The transport efficiency of the carrier can then be characterized by its average migration speed v in this direction. We have examined the carrier motion in a wide range of bacterial bulk concentrations including a dilute regime, where bacterial swimming is almost uncorrelated, as well as an intermediate turbulent and a final jammed regime. These regimes can be characterized by suitable order parameters. For that purpose, we define the mean magnitude of vorticity $\Omega = \frac{1}{2} \langle |[\nabla \times \mathbf{V}(\mathbf{r}, t)] \cdot \hat{\mathbf{e}}_z|^2 \rangle$ for a bacterial velocity field $\mathbf{V}(\mathbf{r}, t)$ coarse-grained over three bacterial lengths which is a convenient indicator for bacterial turbulence [76, 86]. The average swimming speed v_p of the bacteria obtained by averaging the displacements after a time $t = 10^{-3}\tau$ indicates jamming at high concentrations. Simulation results for these two order parameters are presented for a bacterial suspension in the absence of the carrier [see inset in Figure 4.1(b)]. The results indicate three different states: “dilute” ($\phi \lesssim 0.25$), “turbulent” ($0.25 \lesssim \phi \lesssim 0.75$), and “jammed” ($0.75 \lesssim \phi$). The same sequence of states is found in the experiments [100].

Figures 4.1(a) and 4.1(b) show that the transport efficiency v/v_0 of the carrier peaks in the turbulent regime where it attains a significant fraction of the net bacterial velocity v_0 . Experimentally, this fraction is found to be about 0.25, which is confirmed by the simulations. Snapshots from the experiments and simulations (see insets in Figure 4.1) show a directed motion along the wedge apex though there are considerable fluctuations which we discuss later. For a very dilute regime, there are only a few bacteria pushing the carrier such that v tends to zero in this limit [note that in the experiment no motion of the carrier was observed in a very dilute regime since the resulting bacterial forces are not sufficient to overcome the friction of the carrier with the surface (air-water interface)]. We have also performed simulations for different carrier lengths and opening angles to determine the geometry leading to optimal transport. While we have chosen the optimal apex angle for our experiments, a slightly higher transport efficiency can be achieved with a smaller carrier length, see Figure 4.2.

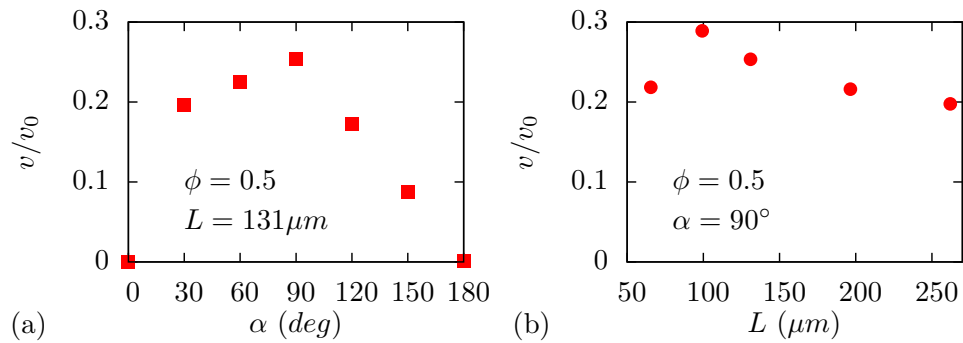


Figure 4.2.: Transport speed for a fixed swimmer density $\phi = 0.5$ for (a) varied apex angles α of the carrier and constant length $L = 131 \mu\text{m}$ and for (b) varied length and fixed apex angle $\alpha = 90^\circ$.

In the following we discuss the underlying reason for the optimal carrier transport in the turbulent regime. First, the bacteria inside the wedge close to the cusp are on average orientationally ordered along the wedge orientation (x -direction). The orientational ordering is revealed by the intensity plots for $\langle \cos \varphi \rangle$, $\langle \sin \varphi \rangle$ which is used as an appropriate orientational order parameter (see the green “hot spot” in Figure 4.3). The “hot spot” sets the carrier into motion along the x -direction. Similar to a moving bulldozer piling up sand, the carrier motion causes an accumulation of particles in the front and a depleted wake, while not destroying the ordering of particles inside the wedge (see the intensity plot in Figure 4.3 as well as Figure 4.4 for experimental and simulation data for the averaged concentration difference between inside and outside bacteria). This concentration difference decreases the transport speed. But the driving effect increases with the increase in bacterial concentration.

When the turbulence sets in, there is a shielding of turbulent fluctuations near the walls of the carrier (see the intensity plots of the local magnitude of vorticity in Figure 4.5). The shielding is, however, more pronounced inside than outside the wedge. Intuitively this implies that the hot spot is shielded from swirls which would sweep away the driving bacteria. (Concomitantly, the outside swirls shown in Figure 4.5 are induced by the bulldozer motion but do not cause

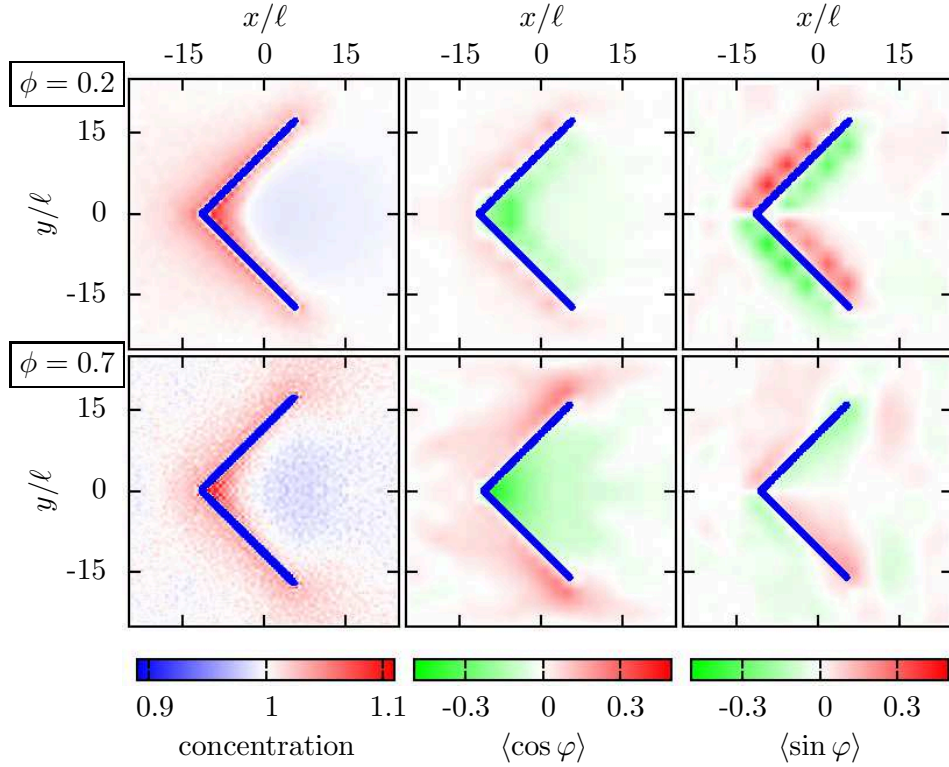


Figure 4.3.: Intensity plots for different bacteria concentrations, $\phi = 0.2$ (top row) and $\phi = 0.7$ (bottom row): local bacterial concentration around the carrier, normalized by the total concentration (left) as well as averaged bacteria orientations $\langle \cos \varphi \rangle$ (middle) and $\langle \sin \varphi \rangle$ (right).

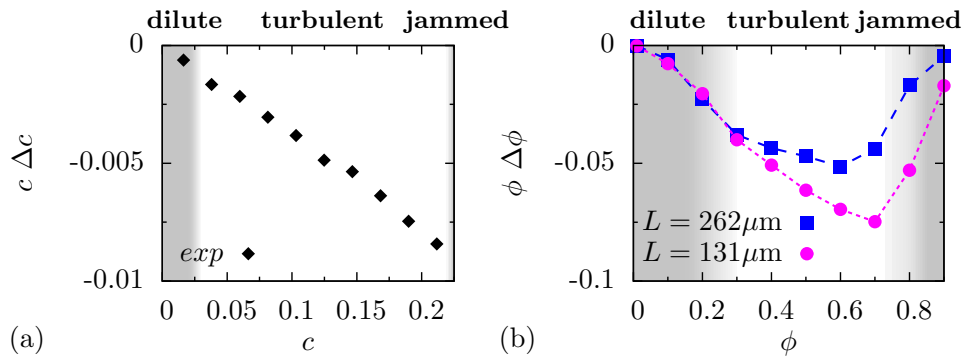


Figure 4.4.: Concentration difference between the wake of the carrier and its front $\Delta c = c_w - c_f$ obtained from (a) experiments and (b) simulations.

the motion.) The intuitive concept of swirl shielding is sketched in Figure 4.5 where also a typical swirl size as a function of the density is shown, which has been obtained as the first minimum of the equal-time spatial velocity autocorrelation function [86]. A typical swirl of

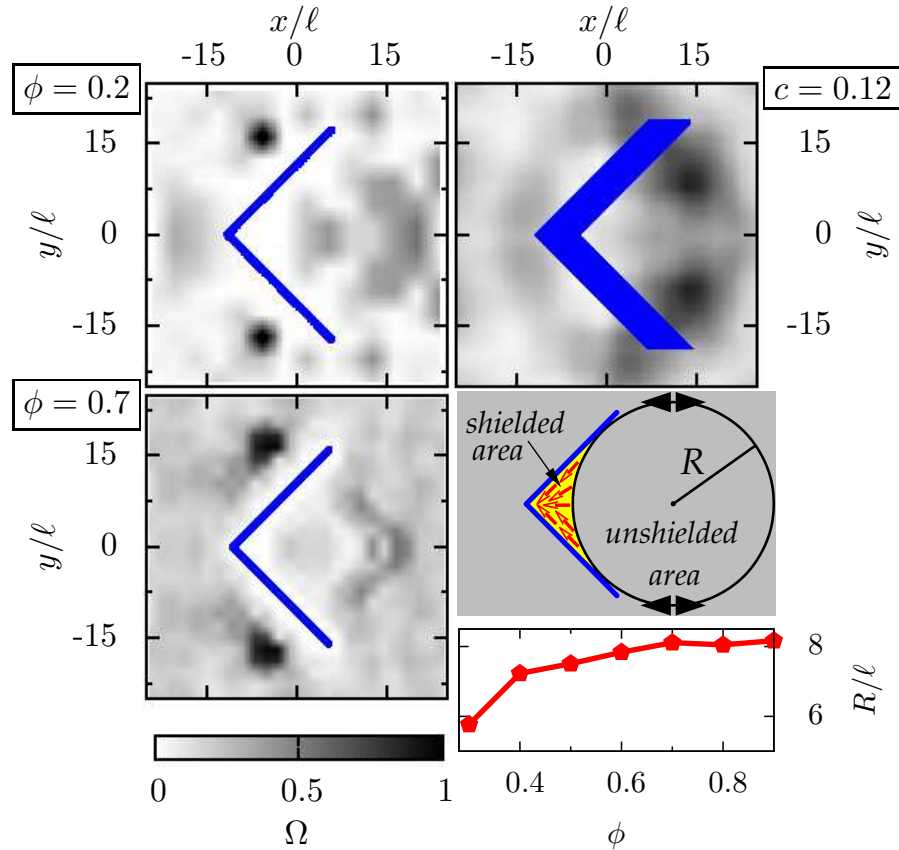


Figure 4.5.: Normalized local enstrophy obtained from simulations (left column) and experiment (top right) for given bacterial concentrations. Bottom right: illustration of swirl shielding in the carrier cusp – bacteria in the shielded area (highlighted in yellow) are indicated by arrows and the unshielded area is marked by dark color – as well as typical swirl radii R for different bacteria concentrations in the turbulent regime.

this size can never reach the “hot spot” area as schematically shown by the shielded area in Fig. 4.5. Swimmer within this area are trapped, leading to large transport velocity correlation times t_v for the carrier, see Figure 4.6. For simple geometric reasons, there is no such shielded zone for the outside bacteria as a swirl can sweep them away. At very high concentrations ($\phi \approx 0.8$), the bacteria are jammed (see Figure 4.1), which is manifested also in a reduced carrier mobility. In conclusion, the polar order of bacteria (see intensity plots in Figure 4.3) inside the wedge and its shielding from the swirls are the two basic ingredients to understand the optimal transport in the turbulent state. As a consequence, optimal transport is achieved when the carrier aperture width is comparable to typical swirl size, see again Figure 4.2.

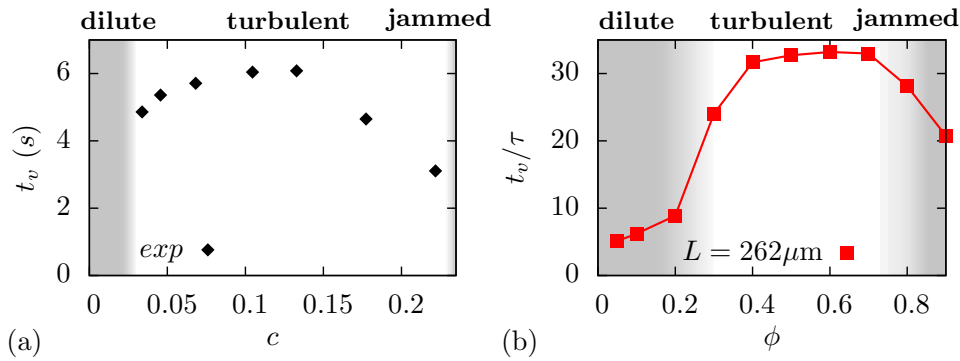


Figure 4.6.: (a) Experimentally and (b) numerically obtained velocity correlation time t_v for various bacteria concentrations.

4.4. Direction of transport

Finally, we plot the full distribution of the carrier velocity direction $P(\vartheta)$ in Figure 4.7(a). For small bacterial densities ϕ the distribution is random, while for intermediate concentrations this distribution exhibits a single peak centered around the x -axis. For even higher concentrations it becomes double-peaked corresponding to a motion perpendicular to the single wedge walls ($\pi \pm \pi/4$). This is correlated with the orientational order distribution of the inside bacteria in the shielded area, $P(\langle\varphi\rangle)$, implying that there is a flipping in the orientation of the inside bacteria, see Figure 4.7(b), for high bacterial concentrations. The kink-like change in the direction of motion perpendicular to the wedge walls is also observed experimentally [see the trajectory in Figure 4.1 and peaks in Figure 4.7(a)].

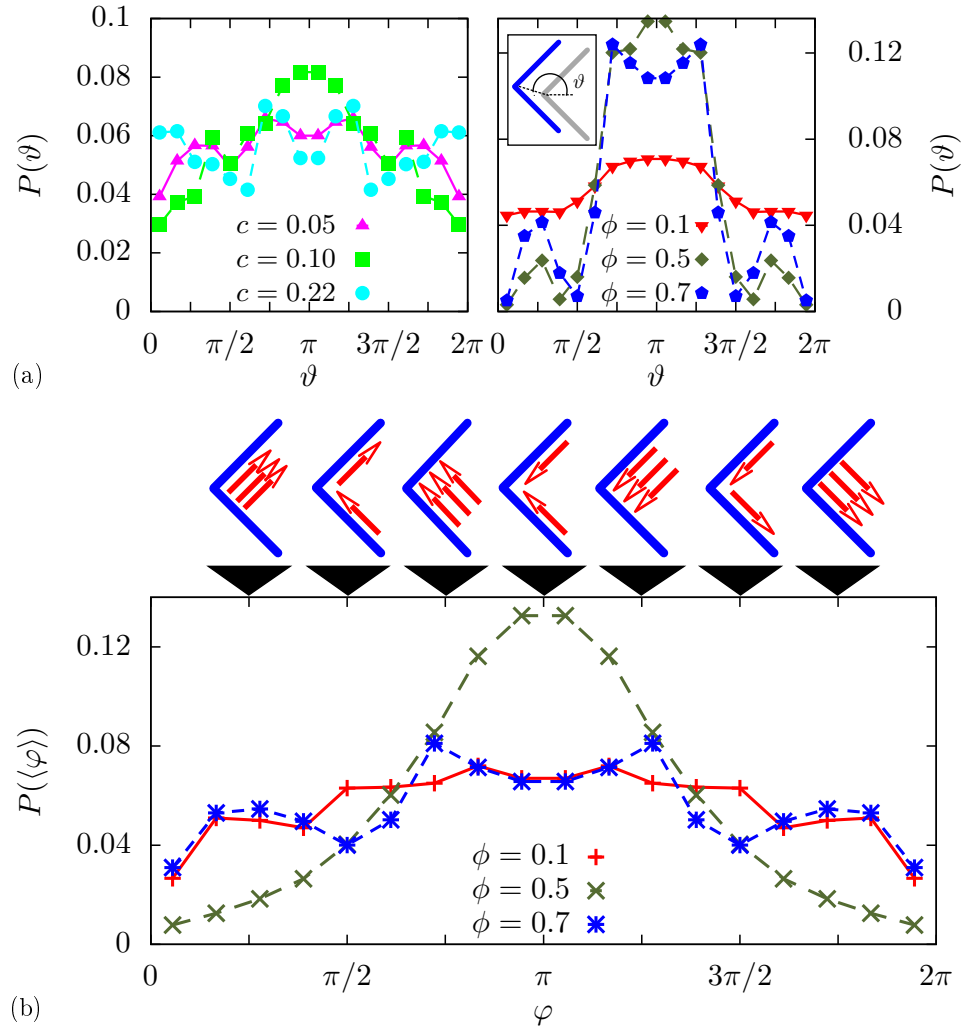


Figure 4.7.: (a) Symmetric full probability distributions of the carrier displacement direction ϑ : Experimental results (left) measured after a time of 0.03 s and numerically obtained data (right) after a time of $10^{-3}\tau$ for various bacterial concentrations. The definition of the displacement angle ϑ is illustrated in the inset. (b) Orientational order distribution of the bacteria within the swirl shielded area. Characteristic configurations are illustrated by sketches.

4.5. Conclusion

We have shown that mechanical energy from bacterial turbulent movements can be extracted powering directed motion of a wedge-like carrier. Both polar ordering and swirl shielding inside the wedge yield an optimal transport velocity which becomes even bidirectional at high concentrations. This effect can be exploited to power and steer microcarriers and motors by bacterial turbulence or collective motion of synthetic swimmers.

Acknowledgments

Work by Andreas Kaiser and Borge ten Hagen was supported by the ERC Advanced Grant INTERCOCOS (Grant No. 267499) and Hartmut Löwen was supported by the SPP 1726 of the DFG. Work by Andrey Sokolov, Anton Peshkov, and Igor S. Aranson was supported by the US Department of Energy (DOE), Office of Science, Basic Energy Sciences (BES), Materials Science and Engineering Division.

Unusual swelling of a polymer in a bacterial bath

The physics of polymer chains in a thermalized bath is governed by scaling laws. One of the most fundamental scaling relates the typical extension of a polymer chain R to its molecular weight N culminating in the traditional Flory exponent ν , such that $R \propto N^\nu$ [89, 90] for very large N . While $\nu = 1/2$ for a Gaussian chain, a self-avoiding chain exhibits a Flory exponent $\nu > 1/2$ which depends on the spatial dimensions d , we have $\nu = 0.588 \approx 3/5$ in three and $\nu = 3/4$ in two dimensions [93]. Similar scaling laws apply to the polymer dynamics where hydrodynamic interactions between the monomers play a crucial role [89]. It is important to note that these basic considerations are designed for equilibrium situations, i.e. the solvent is a thermal bath at temperature T and the chain is not exposed to external fields.

In this Chapter we consider a polymer chain in a bacterial (or active) bath which consists of swimming particles or bacteria. The collisions of the bacteria with the chain lead to nonequilibrium (non-thermal) fluctuations of the chain which may result in new phenomena of chain stretching and compaction different from equilibrium solvents. Active matter itself has been intensely explored over the last years, both for living systems as bacteria [108], spermatozoa [109] and mammals [13, 96] or is system of artificial microswimmers [37, 48, 50, 59, 126, 222] with various propulsion mechanisms [58, 128, 223–225] and a plethora of nonequilibrium pattern formation phenomena were discovered [76, 104, 110, 111, 169, 194, 208, 211, 226–234]. At fixed system boundaries active system show distinct clustering and trapping behavior [5, 130, 179–181, 185–187, 235–239] and can be exploited to steer the motion of microrotors and microcarriers [3, 188, 189] of fixed shape.

Here, we link the field of microswimmers to polymer physics and consider a single polymer chain in a bacterial bath (or an active solvent). The motivation to do so is threefold: first, from a fundamental point of view, there is a need to understand how polymer scaling laws are affected by non-bulk or nonequilibrium situations [240–243]. An active solvent which is intrinsically in nonequilibrium is one of basic cases which put the scaling laws into questions. Second, the collective behavior of microswimmers has been studied at moving boundaries [2, 3, 174] but all of which were of fixed shape. Bacteria and active particles near flexible boundaries have not

This chapter has been published in a very similar form by Andreas Kaiser and Hartmut Löwen, *J. Chem. Phys.* **141**, 044903 (2014), see Reference [4].

yet been explored systematically and it is interesting to understand how clustering and trapping phenomena are modified for flexible boundaries [244]. Our case of a flexible polymer chain is therefore one of the simplest key examples to proceed along this important direction. Third, in general, the set-up we are proposing is realizable in experiments and relevant for biological systems where swarms of bacteria are moving close to flexible objects like at water-air interfaces [245–250]. Our two-dimensional model can indeed be realized e.g. by inserting long polymers into two-dimensional *Bacillus subtilis* suspensions [3, 76, 111]. Another complementary realization is by exposing colloidal model chains [251] to artificial colloidal microswimmers [50, 124, 252].

We use computer simulations of a self-avoiding polymer chain in two dimensions which is exposed to a dilute bath of active particles. As a result, we show that the Flory-scaling exponent $\nu = 3/4$ is unaffected by the bath activity provided the chain is very long. For shorter chains, there is a nontrivial coupling between the bacteria intruding into the chain which stiffen and expand the chain. As a function of the molecular weight, the swelling first scales faster than described by the Flory exponent until a plateau-like behavior with a slight non-monotonicity is reached. This is nonuniversal behavior which reminds to the swelling of polymers in quenched disorder where similar nonmonotonicities have been observed [253, 254] which have, however, a different physical origin. Finally, for large molecular weights, a crossover to the universal Flory behavior is observed. Moreover, as a function of bacterial activity, the chain end-to-end distance shows a pronounced non-monotonicity. The dynamical correlations exhibit a diffusive behavior for very short and long times in qualitative accordance with an equilibrated polymer, while an intermediate ballistic regime can be found in the mean-square displacement of the center of mass of the chain induced by the active solvent.

This Chapter is organized as follows: we introduce our model and our computer simulation technique in Section 5.1. Various results on the statistics of polymer structure in a bacterial bath are presented in Section 5.2 while the polymer dynamics is discussed in Section 5.3. Finally we conclude and give an outlook in Section 5.4.

5.1. Model

We study the statistics of a polymer chain, modeled as a sequence of N coarse-grained spring beads, in a bacterial bath, composed of spherical swimmers in two dimensions, see Figure 5.1. For simplicity, interactions between the active particles and the chain as well as inter-chain interactions are modeled by the same repulsive WCA (Weeks-Chandler-Andersen) potential

$$U_{\text{WCA}}(r) = 4\epsilon \left[\left(\frac{\sigma}{r} \right)^{12} - \left(\frac{\sigma}{r} \right)^6 \right] + \epsilon, \quad (5.1)$$

for distances $r < 2^{1/6}\sigma$. Here the diameter of a bead and a disk-like swimmer is assumed to be equal and is denoted with σ and $\epsilon = k_{\text{B}}T$ is the interaction strength. These quantities

represent the length and energy units, while times are measured in $\tau = \sigma^2/D_0$, where D_0 is the short-time diffusion constant of a single monomer.

Springs are introduced via a so-called FENE (finitely extensible nonlinear elastic) potential [255]

$$U_{\text{FENE}}(r_{ij}) = -\frac{1}{2}KR_0^2 \ln \left[1 - \left(\frac{r_{ij}}{R_0} \right)^2 \right], \quad (5.2)$$

with neighboring beads i, j and their distance $r_{ij} = |\mathbf{r}_i - \mathbf{r}_j|$. The spring constant is fixed to $K = 27\epsilon/\sigma^2$ and the maximum allowed bond-length to $R_0 = 1.5\sigma$. These interactions ensure that for the parameters chosen the swimmers do not cross the polymer chain.

In our chosen units, the overdamped equation of motion of the i th bead located at position $\mathbf{r}_i = [x_i(t), y_i(t)]$ is given by

$$\partial_t \mathbf{r}_i(t) = -\nabla_{\mathbf{r}_i} U + \boldsymbol{\xi}_i \quad (5.3)$$

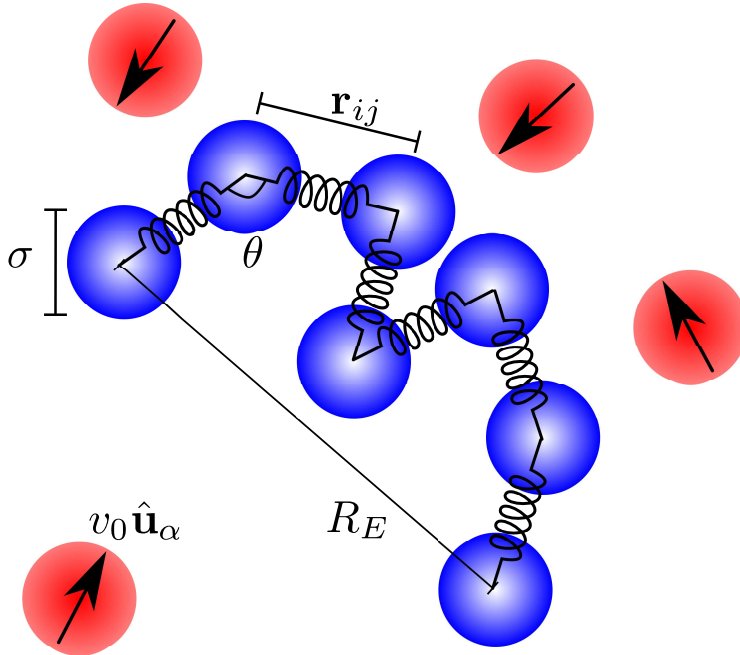


Figure 5.1.: Schematic sketch of the system for a chain with a low number $N = 7$ of beads (blue) connected by springs with bond angle θ . Furthermore the end-to-end distance R_E is indicated. The α th self-propelled disk (red – bottom left) is driven along the marked orientation $\hat{\mathbf{u}}_\alpha$ (black arrow) with an velocity v_0 .

where ξ_i is Gaussian white noise with zero mean and correlations $\langle \xi(t) \xi \otimes (t') \rangle = 2D_0 \delta(t - t') \mathbb{1}$ with the unit tensor $\mathbb{1}$, and U is the total potential energy. The overdamped equation of motion for a swimmer α is described through

$$\partial_t \mathbf{r}_\alpha(t) = -\nabla_{\mathbf{r}_\alpha} U + v_0 \hat{\mathbf{u}}_\alpha(t) + \xi_\alpha \quad (5.4)$$

where ξ_α is Gaussian white noise as before, U is the total potential interaction, and v_0 is a self-propulsion velocity directed along $\hat{\mathbf{u}}_\alpha = (\cos \varphi_\alpha, \sin \varphi_\alpha)$, which will be given by the dimensionless Péclet number $Pe = v_0 \sigma / D_0$. The presence of v_0 brings the system inherently into non-equilibrium. Finally, the orientation of the swimmer is coupled to the rotational Langevin equation

$$\partial_t \hat{\mathbf{u}}_\alpha(t) = \zeta_\alpha \times \hat{\mathbf{u}}_\alpha(t). \quad (5.5)$$

Here ζ_α is as well a Gaussian-distributed noise with zero mean and variance $\langle \zeta(t) \otimes \zeta(t') \rangle = 2D_r \delta(t - t') \mathbb{1}$ and the corresponding rotational diffusion coefficient is $D_r = 3D_0 / \sigma$.

Steric interactions between the active particles are modeled by a soft repulsive Yukawa potential. The total pair potential between a pair of disks $\{\alpha, \beta\}$, is given by

$$U_{\alpha\beta} = U_0 \frac{\exp(-r_{\alpha\beta} / \sigma)}{r_{\alpha\beta} / \sigma}, \quad (5.6)$$

where the screening length corresponds to the disk diameter σ and $r_{\alpha\beta} = |\mathbf{r}_\alpha - \mathbf{r}_\beta|$ is the distance between the swimmers, the prefactor is set to $U_0 = 20\epsilon$.

We perform Brownian dynamic simulations for various chain lengths $1 \leq N \leq 1000$ ($N = 1$ refers to the case of a single spherical tracer) using periodic boundary conditions in a square simulation domain with an area $A = L_0^2$ where $L_0 \sim N\sigma$ corresponds to the contour length of a linear chain in equilibrium. In integrating the Brownian dynamic equations of motion, we have used a finite time step $10^{-7}\tau$. The number of bacteria is determined by the dimensionless packing fraction

$$\phi = \frac{N_S \sigma^2}{4A}, \quad (5.7)$$

where N_S is the number of swimmers. We are interested in a dilute bacterial bath, so we chose $\phi \leq 0.02$, which is below the jamming transition for self-propelled disks [86]. Statistics are gathered for 20 to 50 independent simulation runs.

5.2. Results

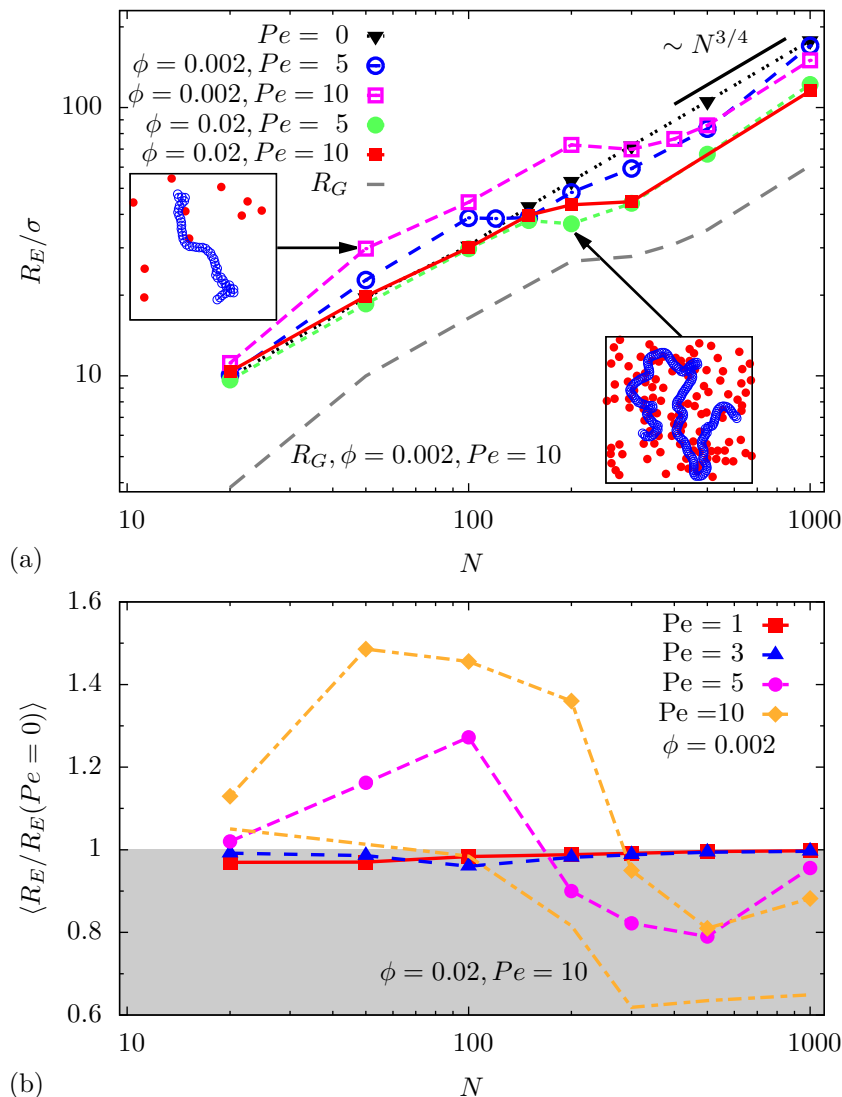


Figure 5.2.: (a) End-to-end distance R_E as a function of number of monomers N for different bacterial densities ϕ and different self-propulsion strengths Pe . Line corresponds to the radius of gyration R_G of the polymer for the given parameters. (b) Relative end-to-end distance, now scaled with its value at vanishing Péclet number, versus molecular weight N for different Péclet numbers at $\phi = 0.002$. The dashed line without symbols corresponds to the reduced end-to-end distance for $Pe = 10$ at $\phi = 0.002$.

As a key result, in Figure 5.2 the dependence of the end-to-end distance on the molecular weight is shown on a double-logarithmic plot where the slope indicating the typical two-dimensional Flory scaling with $\nu = 3/4$ is also indicated. For small chain lengths, the polymer

swells stronger than Flory scaling which is obviously more pronounced for large activities Pe . The strong swelling results from events where a bacterium intrudes into the polymer chain stretching it, see inset of Figure 5.2. Increasing the molecular weight N further results again in more coiling such that a plateau-like regime is reached, the associated molecular weight needed to reach the plateau depends on the Péclet number. Even a slight nonmonotonicity is compatible with the statistical uncertainties. Finally, a crossover to the universal Flory behavior of a self-avoiding chain is observed. This is expected since at very large scales only the statistics of self-avoidance should matter. In this limit, the presence of the bacteria are just providing some kind of higher effective temperature to the polymer such the typical entropically generated Flory exponent is obtained, compare to a similar finding in Ref. [256]. Clearly, the non-universal plateau-like behavior is also found when the radius of gyration is plotted instead of the end-to-end distance, see again Figure 5.2. In Figure 5.2(b), the polymer extension is again shown versus the molecular weight N but is now scaled with its equilibrium value for vanishing activity at same N . By definition, this quantity is unity when $Pe = 0$ but varies with increasing Péclet number. Interestingly, for this quantity there is a marked nonmonotonicity in N at intermediate Péclet numbers. For small N , the scaled end-to-end distance $R_E/R_E(Pe = 0)$ is larger than unity quantifying the stretching effect by the bacteria sliding along the polymer chain. For larger N , the collisions of the bacteria with the polymer chain lead effectively to a compression as signalled by $R_E/R_E(Pe = 0) < 1$. It is instructive here to consider the limit of infinite Péclet number. In this extreme case a single active particle would stretch the full polymer chain to its contour length implying a huge change in the end-to-end distance. At finite density, this extreme stretching is compensated by multiple particle collisions – see the reduced end-to-end distance for a fixed activity $Pe = 10$ and varied density [Fig. 5.2(b)]. However, the high Péclet number limit cannot be easily simulated as the time step required to resolve the dynamics has to be chosen to be very small.

The distribution of the end-to-end distance is shown in Figure 5.3(a) for various Péclet numbers for a fixed molecular weight $N = 50$ revealing a broad peak which first shifts to the left and subsequently to the right for increasing Pe . For intermediate Péclet numbers the peak is pretty broad documenting the strong polymer fluctuations imprinted by the bacterial bath. The quantitative analysis of the shift is shown in Figure 5.3(b) where the end-to-end distance in units of the contour length L_0 is plotted versus Péclet number for various N and at fixed diluted $\phi = 0.002$. For fixed N , a nonmonotonic behavior of R_E/L_0 (or equivalently of R_E/σ) is clearly revealed as a function of Péclet numbers. This can qualitatively understood as follows: for small Pe a bacterium intrudes into the swollen chain and thus compactifying it, see also the snapshot series in Figure 5.3(c). The larger Pe becomes, the more is the bacterium able to really stretch the chain by sliding along it which then induces an increase in the averaged polymer extension. This scenario occurs over the whole range of molecular weight explored in this work and is therefore quite general. The critical Péclet number for which the averaged polymer size is getting minimal increases with increasing molecular weight N , see Figure 5.3(b).

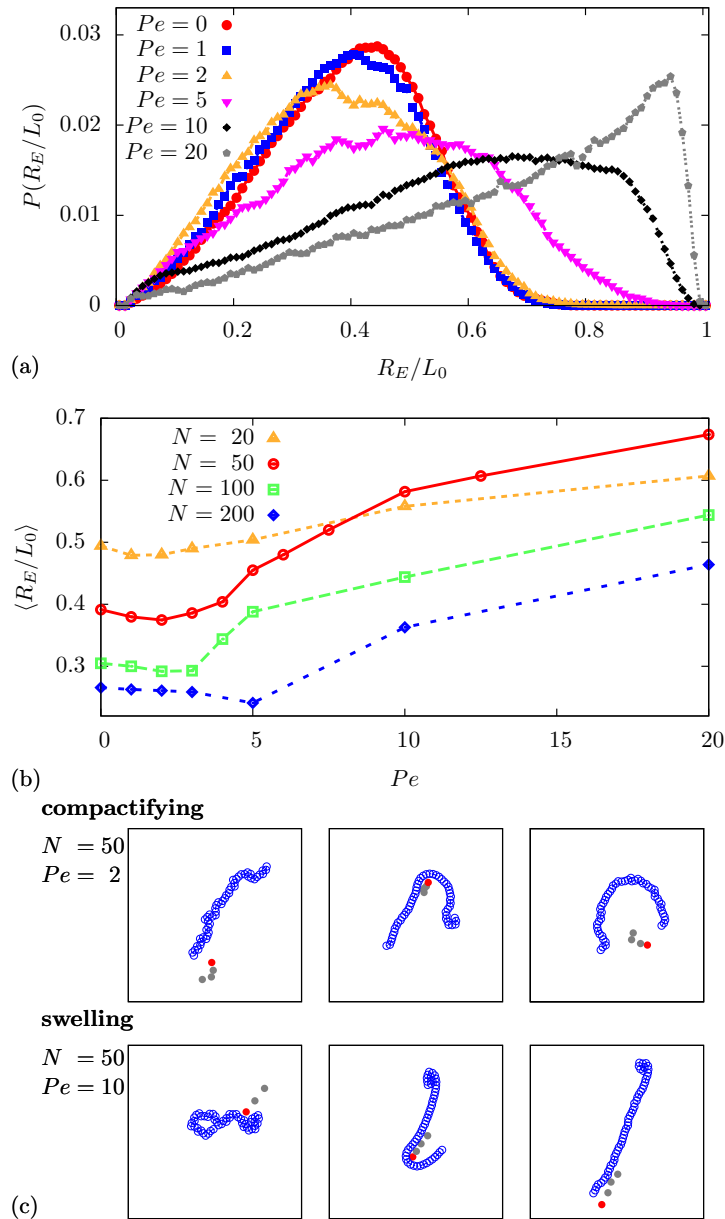


Figure 5.3.: (a) Probability distribution function of the reduced end-to-end distance R_E/L_0 for various self-propulsion strengths Pe and fixed chain length $N = 50$. (b) Averaged reduced end-to-end distance $\langle R_E/L_0 \rangle$ as a function of Pe for various chain lengths and end-to-end distance for various molecular weights N . (c) Time sequences showing the compactifying and the swelling of a polymer due to an a swimmer. Swimmer trajectories are indicated by its swimmer positions.

Finally, we explore the impact of the intruding bacteria on the bond angle θ of subsequent monomers along the chain in Figure 5.4¹. The statistical distribution of θ , as shown in Fig-

¹Another measure for the stiffness of the chain is the polymer persistence length [257] which could be used as an alternative quantity.

ure 5.4(a), reveals a double peak of stretched parts of the chain where the bacteria are scratching along and a coiled part unaffected by the bacteria, see again Figure 5.3(c). The average value $\langle\theta\rangle$ increases with Pe reaching slowly the asymptotic value of π due to full chain stretching induced by a bacterium travelling along the polymer, see Figure 5.4(b).

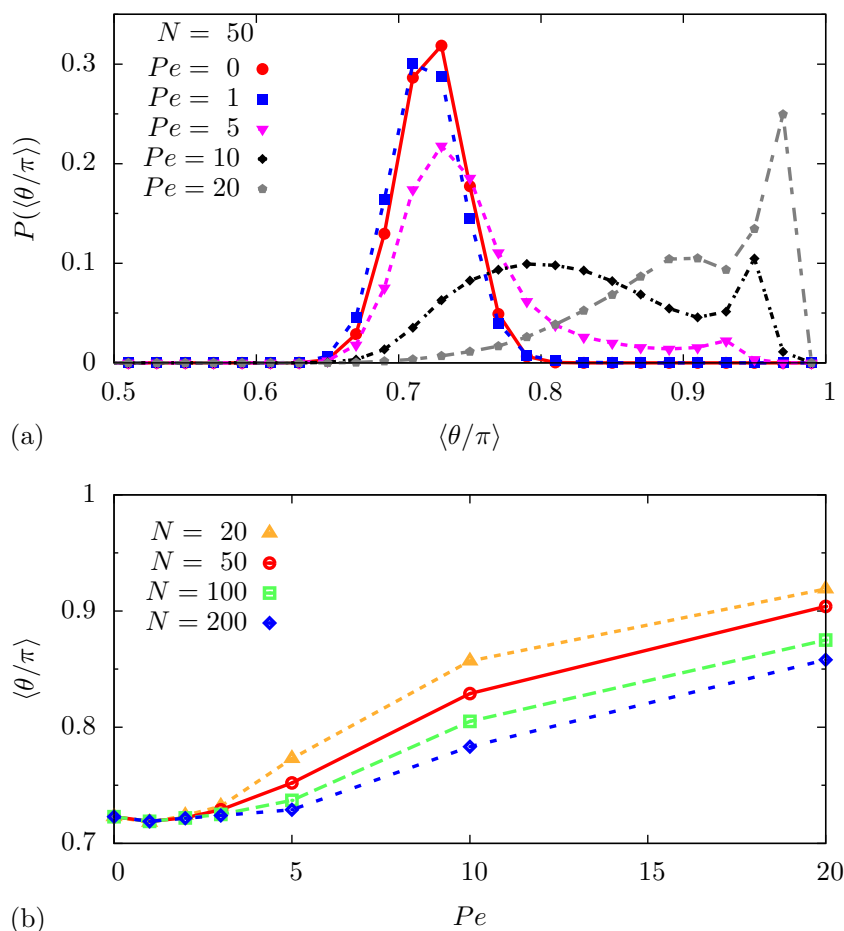


Figure 5.4.: (a) Probability distribution function of the averaged bond angle $\langle\theta\rangle$ at fixed $N = 50$ for various Péclet numbers Pe . (b) Averaged bond angle θ versus self-propulsion strength Pe for various molecular weights N .

5.3. Polymer dynamics

We finally turn to the influence of the bacterial bath on the polymers dynamics which is typically measured in terms of mean-square displacements. One may consider the latter for the end-monomer position \mathbf{r}_N , the end-to-end distance R_E itself, and the center of mass position \mathbf{r} .

Let us first recall the well-known scalings for a polymer in a thermal bath, corresponding to the case $Pe = 0$. In equilibrium, in the absence of hydrodynamic interactions, the mean square displacement of the *end-monomer* behaves as [258]

$$\langle(\Delta\mathbf{r}_N)^2\rangle \sim t + \lambda(1 - \exp(-t/\tau_p)), \quad (5.8)$$

for long times where λ is a constant coefficient and τ_p a characteristic polymeric relaxation time. For very short times $\langle(\Delta\mathbf{r}_N)^2\rangle$ is diffusive (i.e. linear in t). The crossover behavior from short to long times can be studied in terms of the logarithmic derivative which sets an effective time-dependent exponent as $\gamma(t) = d \log \langle(\Delta\mathbf{r}_N)^2\rangle / d \log t$. As a function of increasing time t , this exponent first decreases from 1 down to values of approximately 0.5 and then increases back to 1.

The mean-square displacement of the *end-to-end distance* in equilibrium is given for long times by [240]

$$\langle(\Delta R_E)^2\rangle \sim 1 - \exp(-t/\tau_p) \quad (5.9)$$

such that it approaches its limiting values exponentially in time, while it is again diffusive for short times and approximately scales with $\langle(\Delta R_E)^2\rangle \sim t^{1/2}$ for intermediate times [240].

Finally, the mean square displacement of the *center of mass* of the polymer chain scales in equilibrium as

$$\langle(\Delta r)^2\rangle \sim t \quad (5.10)$$

which turns out to be a good approximation for all times.

In Figures 5.5 and 5.6 we compare these well known mean-square displacements for a polymer chain in a thermal bath (insets) with those for a chain in a bacterial bath with $\phi = 0.02$ at a self-propulsion strength $Pe = 10$. We observe for all three studied quantities the same short and long-time behavior. For short time, this is simply a result of our Brownian model. For long times, it is expected that an active solvent can hardly be discriminated from a passive one on average. At intermediate time, however, different behavior gets visible. First of all, the end-monomer mean-square displacement shows an acceleration at intermediate times resulting in a larger value for the exponent $\gamma(t)$, compare Figure 5.5(a) with its inset. This obviously has to do with the intruding bacteria which brings in more dynamics into the chain. This effect is less pronounced for the end-to-end dynamics (Figure 5.5(b)) where the dynamical behavior is qualitative similar to the passive case, see the inset in Figure 5.5(b).

Conversely, for the center of mass motion, there is a strong amplification of the bacterial dragging effect on the chain. Clearly, even new intermediate ballistic scaling regime shows up here where the mean-square displacement scales as t^2 , compare Figure 5.6 with its inset. Again, this has to do with the fact that in this regime the active particles drag the whole

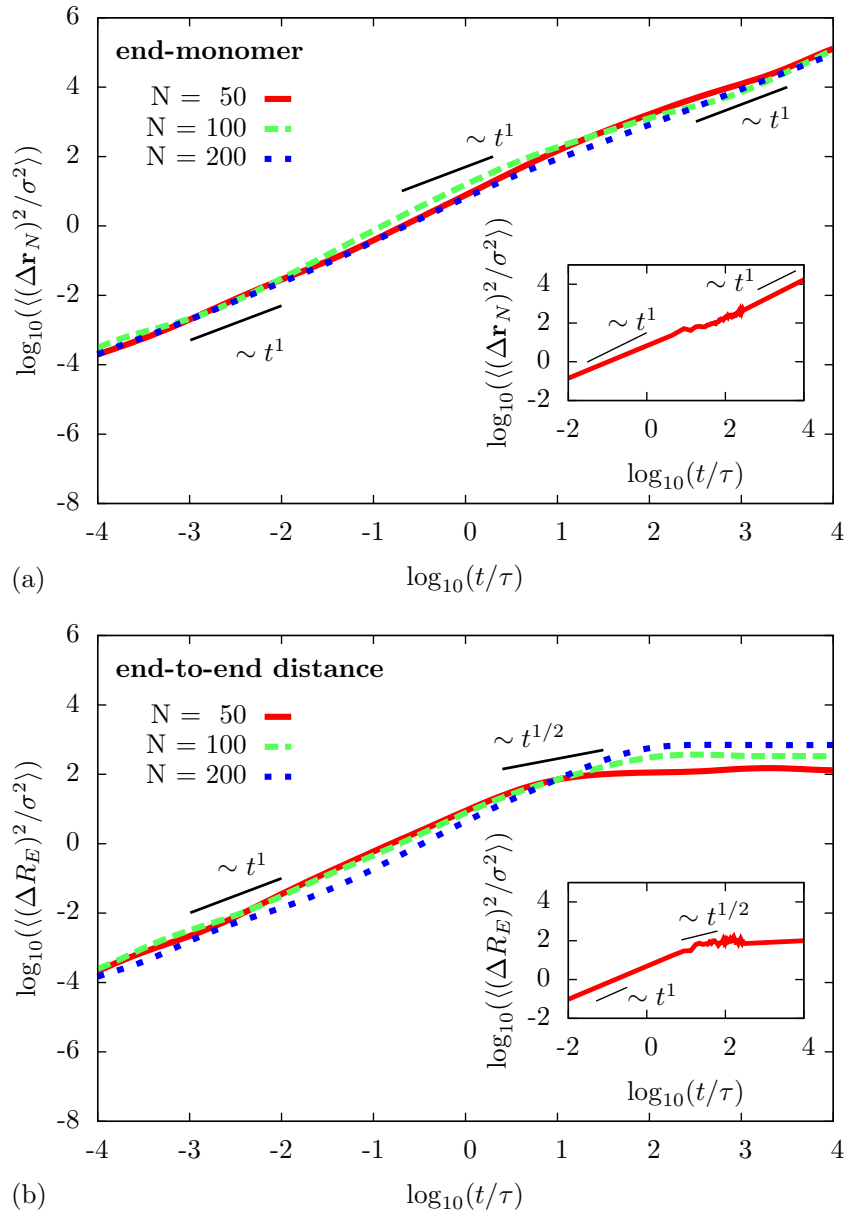


Figure 5.5.: Mean square displacements of (a) the end-monomer and (b) the end-to-end distance for various chain lengths N and a swimmer density of $\phi = 0.02$ with self-propulsion strengths $Pe = 10$. The insets show the temporal behavior for a polymer in a pure thermal bath.

chain with it. The ballistic regime typically ceases to exist when the particle decorrelates its orientation, i.e. its pulling or dragging force, which occurs on a time scale $1/D_r$. This has been studied in great detail for a single Brownian active particle [6,49,148] and will be briefly

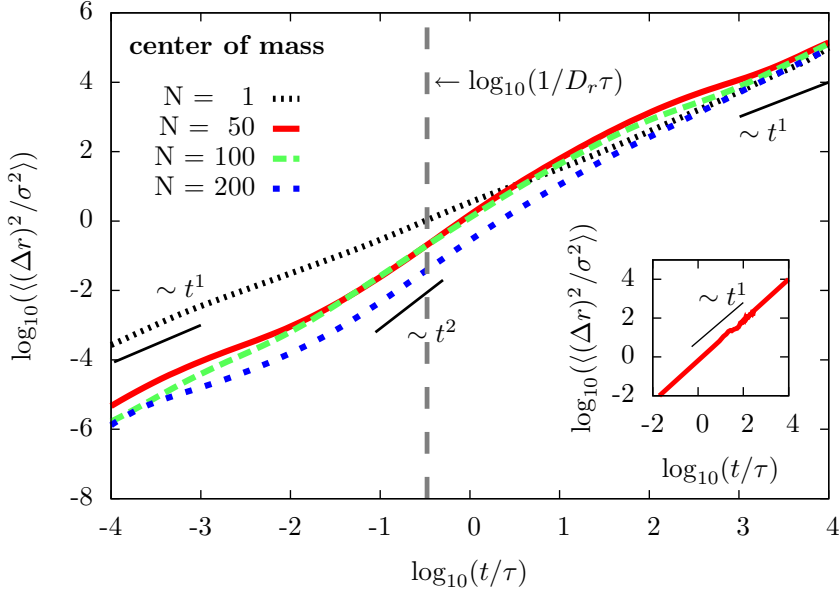


Figure 5.6.: Mean square displacements of the center of mass for various chain lengths N and a swimmer density of $\phi = 0.02$ with self-propulsion strengths $Pe = 10$. The insets show the temporal behavior for a polymer in a pure thermal bath. The dashed vertical line indicates the rotational diffusion time scale $1/D_r$ for an active swimmer.

summarized in the Appendix² following Ref. [6]. The decorrelation time scale $1/D_r$ is plotted as a reference in Figure 5.6 and represents indeed a reasonable upper bound at which the ballistic regime ceases to exist. Finally, as a further extreme reference, we have included the case $N = 1$ of a single segment, representing a passive tracer in a bath of active particles as studied recently [259–261]. In this case, the ballistic regime is not very visible, since the collision time of active particles with the tracer is short.

5.4. Conclusions

We have considered the impact of an active (bacterial) bath on the conformations of a flexible polymer chain in two dimensions by using extensive Brownian dynamics computer simulations. While the traditional Flory scaling for a two-dimensional self-avoiding random walk is found for large chains, there is an interesting nonuniversal behavior for finite chain lengths. Due to the intruding bacteria, the polymer extensions is getting more stretched than predicted by Flory scaling and then crosses over to a plateau where the chain size does not depend on the molecular weight. This behavior is unusual as it is not found in equilibrium. We have further

²Here among others the mean square displacement of an active particle will be presented, showing three distinct regimes.

identified trends of the chain size with increasing bacterial activity and find a relative compression for small activities and a strong stretching for large activities which we attribute to intrusion events of bacteria into the coiled chain. For the polymer dynamics, we find a t^2 scaling for the center of mass mean square displacement for intermediate times, which is absent for athermal solvents.

We hope that our findings will stimulate new explorations. First of all, a detailed theory would be challenging which predicts at least the scaling of the plateau behavior. Moreover, more simulation will be necessary to understand the three-dimensional case both for one-dimensional chains where bacteria can more easily circumvent the polymer and for flexible membranes. In two dimensions our predictions can in principle be verified. Bacterial suspensions [71] spontaneously form chains of inert bacteria in a bath of mobile ones. These chains can be considered to act like a passive polymer. When confined between glass plates this would be an intriguing realization of our model. It can also be realized on the granular level. Shaken granulates provide an active bath [194,262] and a usual macroscopic chain of millimetric beads can be added as a passive polymer. This set-up has the advantage that it can be studied in real-space directly avoiding any microscope. However colloidal polymers which are built by using lock-and-key colloids as monomeric entities [251] are among the realisations. These can easily be confined between glass plates and exposed to further artificial colloidal microswimmers such that the non-crossing situations which is crucial for our set-up is realized. It is less evident how our model is realized for real polymer chains and real bacteria as those are typical crossing in strong slit confinement. A related set-up are bacteria close to a liquid-air interface which are standardly considered in experiments, see e.g. Refs. [245,249,250]. The latter interface is flexible but under tension. The intrusion effect, however, is also expected to play a leading role in case the line tension is small compared to thermal effects. Finally we think that the complex interaction between bacteria and flexible filaments as revealed in our study may be exploited in general for the fabrication of machines on the micro- and nanoscale [186].

It would be interesting to consider bacterial suspensions with higher density as well as polymer chains at finite densities. At high densities the active bath is known to exhibit clustering [169,229,263,264]. It is an interesting question to study how an added passive polymer chain would influence the clustering behaviour. We expect that it will act as a heterogeneous nucleation center to nucleate active particle clusters. The feedback of clustering on the extension of the polymer chain is less obvious and left for future research. Finally for finite chain density the formation of a polymeric glass [265] which is well studied in a thermal bath is unexplored in an active bath. One might expect different dynamical modes (such as reptation) [90] in such a bath.

Acknowledgments

We thank Berenike Maier, Roland Netz, Christian von Ferber, Lyderic Bocquet, and Igor S. Aranson for helpful discussions. This work was financially supported by the ERC Advanced Grant INTERCOCOS (Grant No. 267499) and by the SPP 1726 of the DFG.

Conclusion

That linear propagating microswimmers are able to form remarkable collective spatiotemporal patterns like swarming or swirling had already been shown by a variety of experiments and simulations. We started this thesis by taking – for the first time – a look at the patterns formed by active particles moving on circular paths, so called circle swimmers. The emerging states have been mapped out in a state diagram spanned by the swimmer density and the radius of the swimming path. Hereby, we could successfully fill the gap between the case of passive rotors, corresponding to a vanishing swimming path radius, and linear propagating swimmers, corresponding to an infinite radius. We have studied the emerging vortex arrays consisting of either one, *singlet-vortex*, or two, *doublet-vortex*, circle swimmers. This state diagram can be reproduced using a simple instability theory.

We studied the influence of static wedgelike confinements on active fluids, as well as the influence of wedgelike confinements moving with a predefined velocity and orientation. In case of a dilute system of self-propelled rodlike particles a static wedgelike obstacle can be used as an efficient trap for these particles. Its efficiency can be tuned by the apex angle. We have presented a theoretical prediction for the critical apex angle which still allows a trapping of a single swimmer, even if the trap is dragged. Three different trapping mechanisms for a single swimmer and different dragging velocities could be observed. The resulting trapping state diagram shows a surprising reentrant effect. For apex angles $\alpha > 90^\circ$ and increasing dragging velocity we find the sequence *no trapping* – *trapping* – *no trapping* – *trapping*. This basic appearance of the trapping state diagram has also been found in case of many swimmers. Hereby, we have been able to show that a drag in the direction of the apex increases the trapping efficiency. For small apex angles a *partial trapping* passes into a *complete trapping* state, while for large apex angles it is possible to have *complete trapping* where it has not been able to trap any particle for lower dragging velocities. Furthermore, we propose a method for a velocity-selective trapping by dragging the trap in the direction of the cusp. This could be used in a suspension of various types of active particles to extract a specific species.

We have studied the efficiency of a directed transport induced by rodlike microswimmers for the whole density range of active particles. In agreement with experiments on *Bacillus subtilis* we have shown that the transport velocity of a wedgelike shuttle has its maximum in a density regime which is known as *bacterial turbulence*. We have successfully worked out the reason for the directed transport and why the velocity is maximal in the turbulent regime by introducing the concept of *swirl shielding*. In the state of bacterial turbulence the active fluid

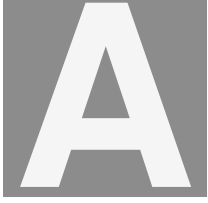
consists of several swirls with different directions of rotation. Due to the wedgelike geometry of the used carrier these swirls cannot wash out swimmers near the cusp. Consequently, swimmers get trapped in this region and are rectified by the wedgelike boundary, which leads to the directed transport. Since the typical radii of the swirls within the active fluid increase with increasing density it is clear why the efficiency increases with growing particle density. Another effect which occurs at the same time is the *bulldozer-effect*. The transported wedge accumulates swimmers in its front, which leads to a slow down. We have shown in this study that it is possible to extract directed motion, meaning useful kinetic energy, out of random fluctuations characterized by the turbulent state of the active fluid.

Finally, we have shown that for long polymer chains submersed in a bacterial bath the spatial extension scales with the well-known Flory exponent. This confirms a previously made assumption that an active fluid can be considered as an effective temperature. To gather further proof for this statement the dynamical quantities of the polymer chain were analyzed by the mean square displacement of typical quantities of polymer chains in a thermal and in a bacterial bath. All quantities show the same short and long-time behavior. However, for short chains the extension scales faster than the Flory exponent. This unusual swollen state is caused by a nontrivial coupling between the microswimmers intruding into the chain and expanding it. For intermediate chain lengths even a plateaulike behavior can be observed. As a function of activity the end-to-end distance of the polymer chain exhibits a strong non-monotonicity in N at intermediate Péclet numbers.

The basic results of this thesis have already been adopted by various other groups. The quantitative shape of the emergent state diagram for circle swimmers could be confirmed [266] and recently the collective behaviour of active spinners with different directions of rotation has been numerically investigated [267].

With respect to the possibility of trapping active particles there is first experimental evidence that the suggested wedgelike confinement is an effective trap for sperm [185] and artificial rodlike microswimmers [186]. A proposed trapping device for photophoretic swimmers uses a shading mask to slow down and accumulate particles at a predefined area [268]. Recent numerical studies have adopted the idea of dragging a trap through an active fluid by applying a constant external drift to active swimmers in a system with various L- and V-shaped barrier arrays [269], which is basically the same as our study, since we applied a Gallileian transformation. Using the same barriers, the behavior of circle swimmers has been investigated [196]. Rectangular obstacles positioned like a flower can trap circle swimmers. Hereby different flower chiralities lead to a sorting of the swimmers, depending on their direction of rotation [270]. The swimmer accumulation at convex boundaries has been studied for the case of non-interacting spherical self-propelled particles [239]. For such systems even fixed randomly placed obstacles can act as a trapping device [187]. Inside these traps vortexlike patterns have been observed. Asymmetric convex obstacles can also lead to a rectification of active particles [271]. It has been shown, by measuring the mean square displacement, that the curvature of a passive tracer submersed in an active fluid has a huge influence on its rotational and translational motion, as tracers with large curvature enable a directed transport [272].

Problems yet unexplored or unsolved are, among other, the influence of patterned walls on the state of bacterial turbulence, which could be tackled by particle-resolved simulations and by analytical calculations [273]. The behavior of several passive particles of various shapes submersed in an active fluid should be studied in more detail, since they can be used to extract useful energy out of the fluid. Another approach would be to check if several building blocks can be assembled by the active fluid to form a workable micromachine.



Appendix: Non-Gaussian statistics for the motion of self-propelled Janus particles: Experiment versus theory

In this Appendix we will briefly summarize the statistical properties of the diffusiophoretic motion of self-propelled particles using Platinum-Silica Janus spheres and our theoretical approach based on the Langevin description, see Ref. [6]. In the according experiments the particles have been in a quasi two dimensional confinement. The translation was limited to a plane, while the particle was freely rotating in three dimensions. The appropriate Langevin equations for the translational and rotational motion can be written as

$$\begin{aligned}\frac{d\mathbf{r}}{dt} &= \frac{D}{k_B T} F_0 \hat{\mathbf{u}} + \sqrt{2D} \boldsymbol{\xi}_r, \\ \frac{d\hat{\mathbf{u}}}{dt} &= \sqrt{2D_r} \boldsymbol{\xi}_{\hat{\mathbf{u}}} \times \hat{\mathbf{u}}.\end{aligned}$$

The translational and rotational random motion due to the kicks of the solvent molecules is included by the Gaussian noise terms $\boldsymbol{\xi}_r$ and $\boldsymbol{\xi}_{\hat{\mathbf{u}}}$ with zero mean and variances $\langle \boldsymbol{\xi}_r(t_1) \otimes \boldsymbol{\xi}_r(t_2) \rangle = \langle \boldsymbol{\xi}_{\hat{\mathbf{u}}}(t_1) \otimes \boldsymbol{\xi}_{\hat{\mathbf{u}}}(t_2) \rangle = \delta(t_1 - t_2) \mathbb{1}$, where $\mathbb{1}$ is the unit tensor and the self-propulsion is modeled by an effective force F_0 directed along the particle orientation $\hat{\mathbf{u}} = (\sin \theta \cos \varphi, \sin \theta \sin \varphi, \cos \theta)$. We will see later on that in case of large self-propulsion strengths the particle orientation will be confined to two dimensions, corresponding to $\theta = 0$. The self-propulsion will be measured by the dimensionless self-propulsion strength $a = F_0 d / k_B T$, where d is the diameter of the swimmer.

Mean square displacement of an active particle

In Figure A.1 we compare the experimentally obtained mean square displacement $\langle(\Delta\mathbf{r})^2\rangle$ of a self-propelled Janus sphere with the theoretical prediction.

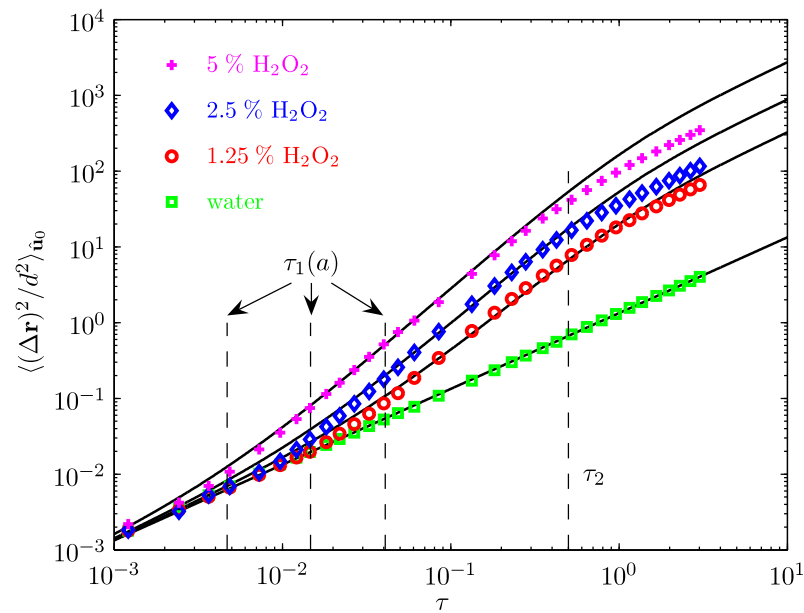


Figure A.1.: Comparison of the measured mean square displacement (symbols) with the theoretical prediction (solid curves) using appropriate fitting parameters a , see Ref. [6] for details. Dashed lines indicate the transition times $\tau_1(a) = 18/a^2$ and $\tau_2 = 1/2$ between the different regimes of motion.

Obviously we can distinguish three different regimes. For short times $t < \tau_1$ where particles undergo simple Brownian motion, $\langle(\Delta\mathbf{r})^2\rangle \sim t^1$, and the deterministic displacements due to the self-propulsion are not relevant. For longer times $\tau_1 < t < \tau_2$ the activity of the swimmer leads to a superdiffusive motion. Hereby the transition time τ_1 depends on the strength of the self-propulsion and is given by $\tau_1(a) = 18/a^2$, times are given in dimensionless units $\tau = tD_r$. The motion of the Janus particle is again Brownian for large times due to the rotational diffusion [49] with a constant transition time $\tau_2 = 1/2$ in our chosen units.

Higher displacement moments and displacement distribution function

On top of the analysis of the mean square displacement, here we also address skewness S and excess kurtosis γ , which serve to quantify the non-Gaussian behavior of self-propelled particles [148, 274]. They are given by

$$S = \frac{\langle(\Delta x)^3\rangle_{\hat{u}_0}}{\langle(\Delta x)^2\rangle_{\hat{u}_0}^{3/2}}$$

and

$$\gamma = \frac{\langle(\Delta x)^4\rangle_{\hat{u}_0}}{\langle(\Delta x)^2\rangle_{\hat{u}_0}^2} - 3,$$

respectively. Note that these equations are only valid because $\langle\Delta x\rangle_{\hat{u}_0} = 0$ in the system. Otherwise, the moments have to be replaced by the respective central moments. As the third moment $\langle(\Delta x)^3\rangle_{\hat{u}_0}$ trivially vanishes due to the symmetry of the full displacement probability distribution $\Psi(\Delta x, t)$, resulting from the averaging over the initial orientation \hat{u}_0 of the Janus particles, the skewness S is zero; though, the measurements in H_2O_2 solution clearly yield nonzero values for the excess kurtosis γ , which directly indicates non-Gaussian behavior.

Basically, the theoretical results show the same tendency as for the experimental curves in Figure A.2(a). In particular with regard to the general behavior and the position of the minimum for intermediate times the agreement is very good, although the experimental values for γ are usually less negative than the theoretical predictions. Slightly positive values as measured for very short times can again be ascribed to small deviations from an ideal isotropic particle shape, similar to our observations in pure water.

To visualize the non-Gaussian distribution, we are also interested in the exact shape of the full displacement distribution function $\Psi(\Delta x, t)$ for the one dimensional displacement. In water (corresponding to passive particles), the Janus particles show a simple diffusive behavior corresponding to Gaussian probability distributions at all times. However, for self-propelled particles the curves for $\Psi(\Delta x, t)$ significantly deviate from a Gaussian shape. In Figure A.3(a) exemplary the experimental results for various fuel concentrations, corresponding to various self-propulsion strengths, are given as well as numerically obtained results. All results show the same characteristic features - such as the broadened peak and the steep wings - as the experimental plots. These results have been obtained for low self-propulsion strengths where the orientation of the swimmer purely diffusive in three dimension. However large self-propulsion strengths lead to a double-peak structure for intermediate times of the full displacement probability function, see Figure A.4(a). Experimental observations have led to the conclusion that in case of strong self-propulsion the orientation of the particle is restricted to the plane of motion. Considering this limitation to the rotation of the self-propelled spheres in the numerical framework lead to the same shape of the probability distribution, see Figure A.4(b).

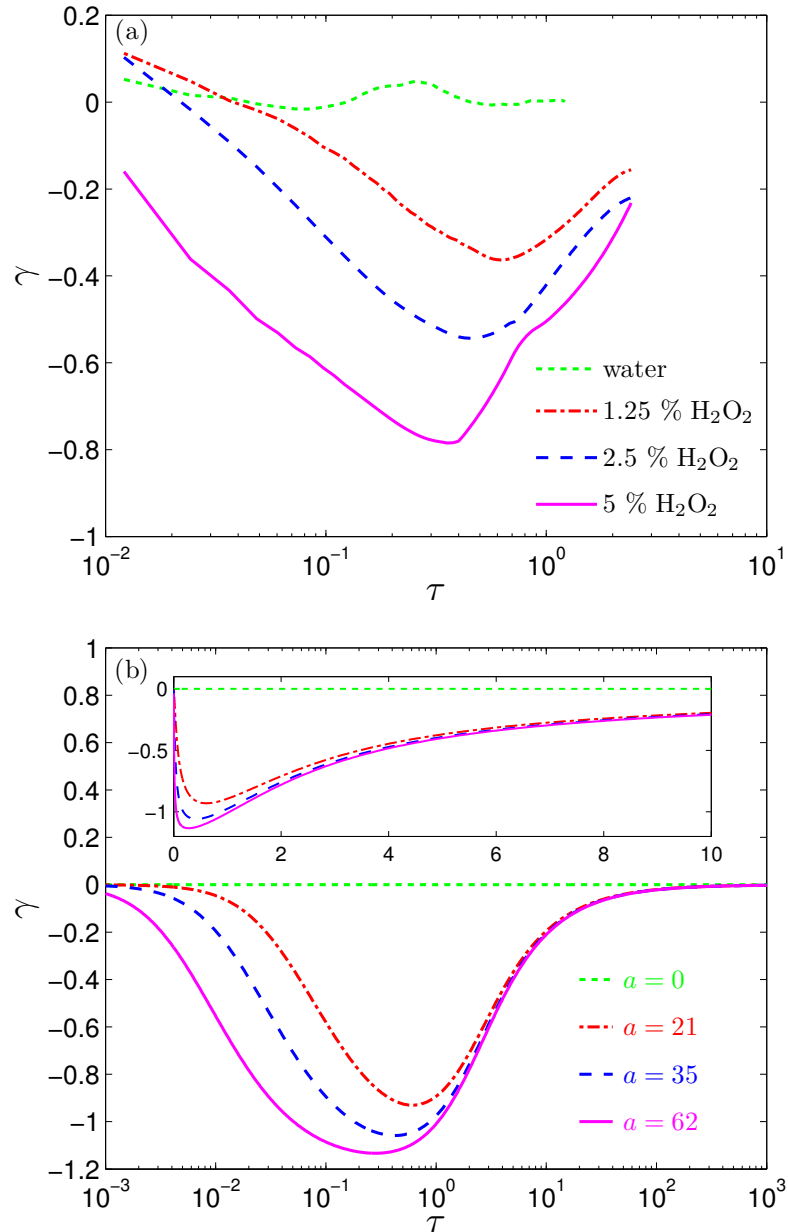


Figure A.2.: (a) Experimental and (b) theoretical results for the excess kurtosis γ . The theoretical curves are calculated for the values of the self-propulsion force extracted from the MSD fits in Figure A.1. Inset in (b): Visualization of the theoretical data in a linear plot.

In general for small times the random translational motion dominates, leading to a Gaussian distribution and a vanishing kurtosis. The same is true for large times due to rotational diffusion. The shape of the displacement probability distribution function depends however strongly on the self-propulsion (and its orientational constraints), leading to either a just broadened peak or even a double-peak.

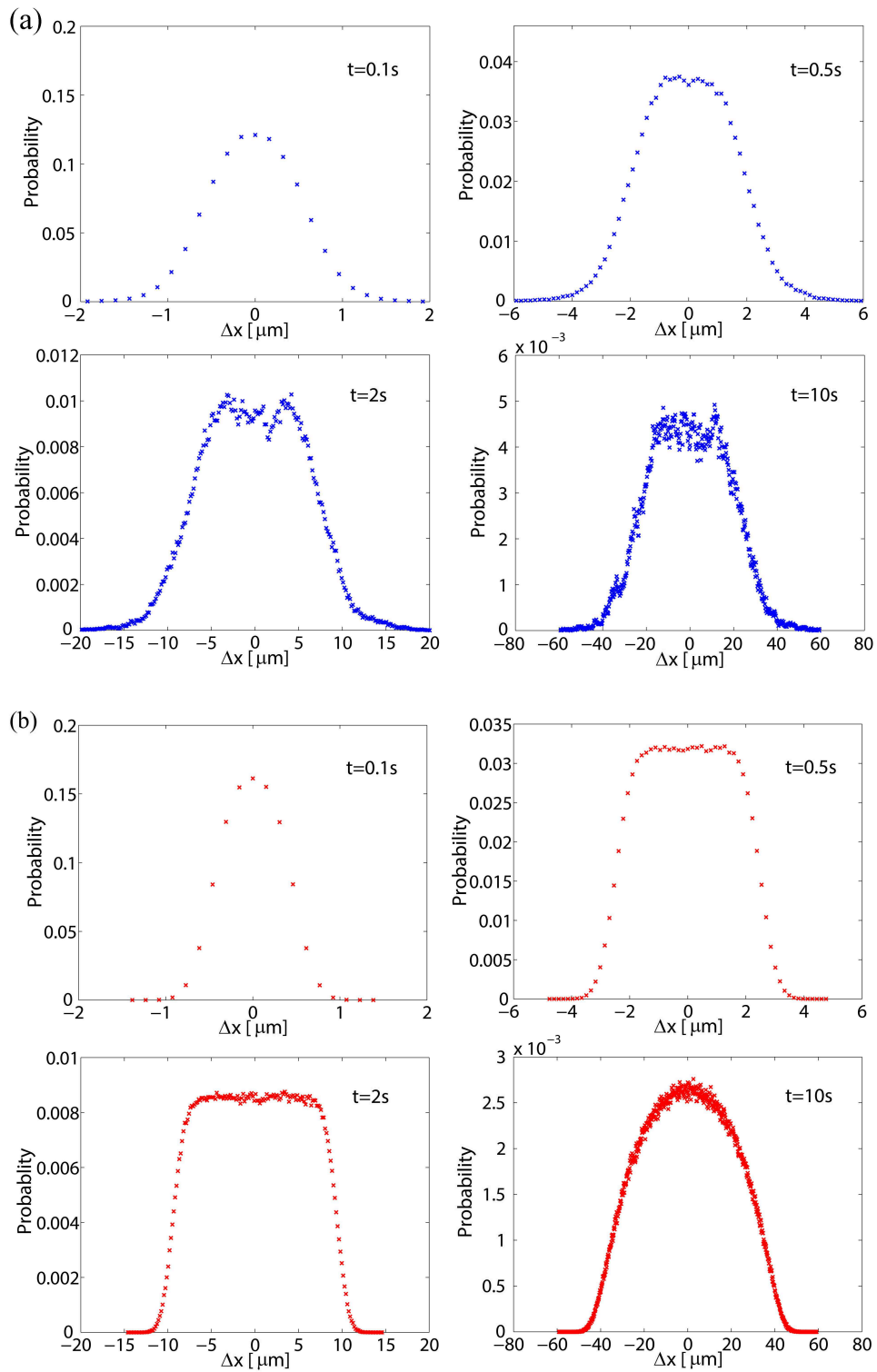


Figure A.3.: Time evolution of $\Psi(\Delta x, t)$: (a) experimental results for 5 % H_2O_2 concentration, (b) corresponding simulation for $a = 62$.

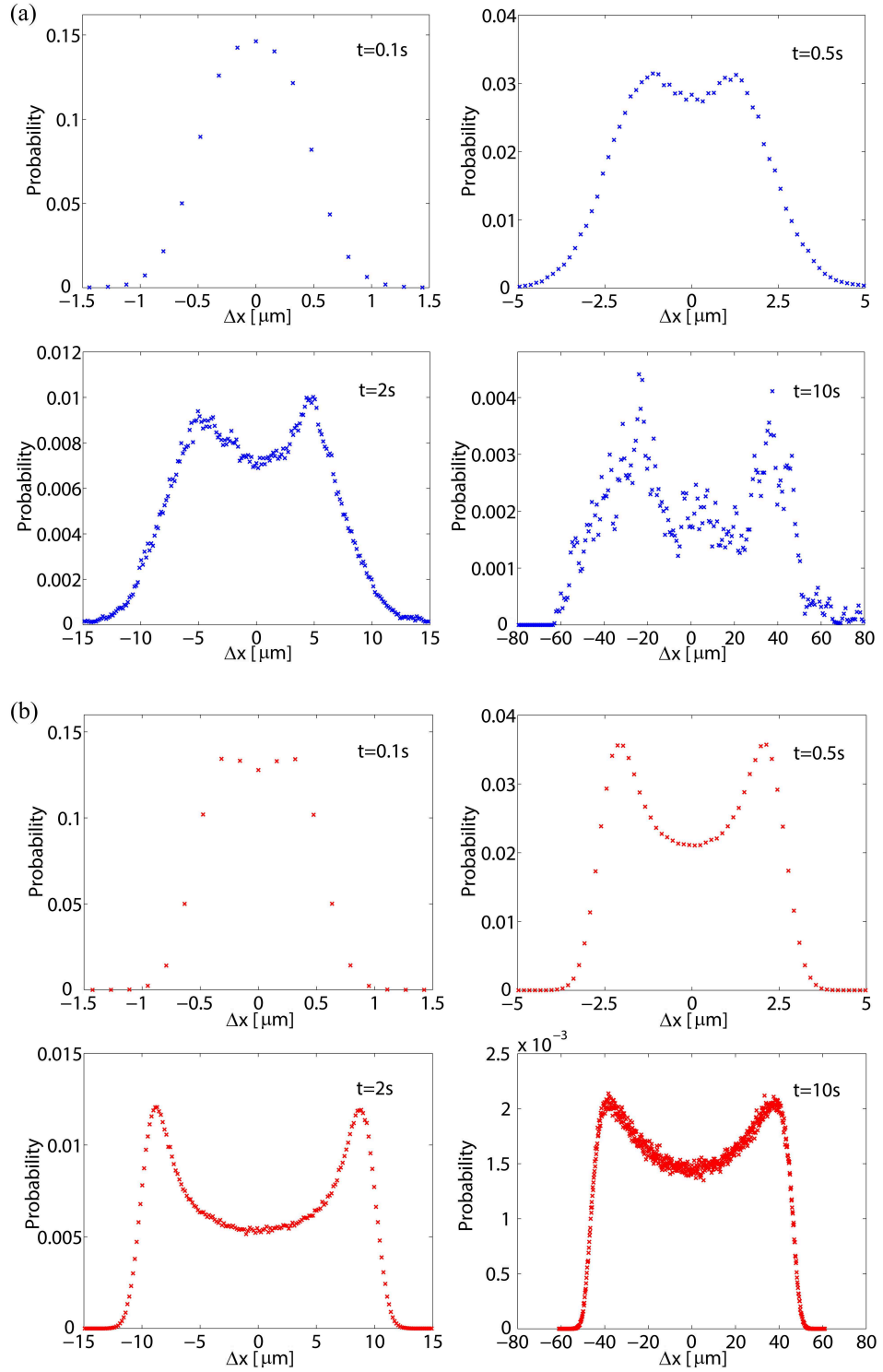


Figure A.4: (a) Time evolution of the measured probability distribution $\Psi(\Delta x, t)$ for Janus particles in a 10 % H_2O_2 solution. The occurrence of the double peak indicates that the particle orientation does not diffuse freely on a unit sphere for high H_2O_2 concentrations. (b) Reference simulation for particles whose orientation is restricted to the x - y plane.

Acknowledgments

In the end, I want to thank several people who supported me during this thesis and beyond that.

At first I want to thank Prof. Hartmut Löwen for giving me the opportunity to work at his institute and on such a great and fast-developing topic. I would particularly like to thank for countless Friday evenings – in good times and in bad times – for long discussions starting with "Do you have a minute?" and for making it possible for me to attend several conferences. I have to give thanks for the outstanding supervision, the patience to wait for some results (flexible chain) and leaving me free to work on other projects.

Also I want to thank Prof. Jan Dhont for being the second assessor of this thesis.

I want to thank my collaborators for their great job. Especially Igor S. Aranson for the opportunity to visit him at the Argonne National Lab and Borge ten Hagen for lots of discussions and sharing an office.

I want to thank all members of the institute for a lot of inspiring discussions – scientific and non-scientific (especially Andreas Menzel, Marco Heinen and Peet Cremer) – and of course for all the cakes, cookies and sweets during the years. Beyond that of course my fellow students who accompanied me in the lectures and in my desperation regarding some exercise sheets (Sandra Held, Oliver Karger, Thomas Hahn, Tobias Franzen, and many many more) and Savas Özdemir and Tomek Garbowski for the nice time working in the "Physikalisches Grundpraktikum".

The concluding thank you goes to all who have been available for proofreading and finding typos.

Bibliography

- [1] A. Kaiser and H. Löwen. Vortex arrays as emergent collective phenomena for circle swimmers. *Phys. Rev. E* **87**, 032712 (2013).
- [2] A. Kaiser, K. Popowa, H. H. Wensink, and H. Löwen. Capturing self-propelled particles in a moving microwedge. *Phys. Rev. E* **88**, 022311 (2013).
- [3] A. Kaiser, A. Peshkov, A. Sokolov, B. ten Hagen, H. Löwen, and I. S. Aranson. Transport powered by bacterial turbulence. *Phys. Rev. Lett.* **112**, 158101 (2014).
- [4] A. Kaiser and H. Löwen. Unusual swelling of a polymer in a bacterial bath. *J. Chem. Phys.* **141**, 044903 (2014).
- [5] A. Kaiser, H. H. Wensink, and H. Löwen. How to capture active particles. *Phys. Rev. Lett.* **108**, 268307 (2012).
- [6] X. Zheng, B. ten Hagen, A. Kaiser, M. Wu, H. Cui, Z. Silber-Li, and H. Löwen. Non-Gaussian statistics for the motion of self-propelled Janus particles: Experiment versus theory. *Phys. Rev. E* **88**, 032304 (2013).
- [7] H. H. Wensink, H. Löwen, M. Marechal, A. Härtel, R. Wittkowski, U. Zimmermann, A. Kaiser, and A. M. Menzel. Differently shaped hard body colloids in confinement: From passive to active particles. *Eur. Phys. J. Spec. Top.* **222**, 3023 (2013).
- [8] A. Kaiser, A. Sokolov, I. S. Aranson, and H. Löwen. Mechanisms of carrier transport induced by a microswimmer bath. *arXiv*, 1408.1883 (2014).
- [9] M. Ballerini, N. Cabibbo, R. Candelier, A. Cavagna, E. Cisbani, I. Giardina, V. Lecomte, A. Orlandi, G. Parisi, A. Procaccini, M. Viale, and V. Zdravkovic. Interaction ruling animal collective behavior depends on topological rather than metric distance: Evidence from a field study. *Proc. Natl. Acad. Sci. U.S.A.* **105**, 1232 (2008).
- [10] Y. Katz, K. Tunstrøm, C. C. Ioannou, C. Huepe, and I. D. Couzin. Inferring the structure and dynamics of interactions in schooling fish. *Proc. Natl. Acad. Sci. U.S.A.* **108**, 18720 (2011).
- [11] J. Buhl, D. J. T. Sumpter, I. D. Couzin, J. J. Hale, E. Despland, E. R. Miller, and S. J. Simpson. From disorder to order in marching locusts. *Science* **312**, 1402 (2006).
- [12] A. John, A. Schadschneider, D. Chowdhury, and K. Nishinari. Trafficlike collective movement of ants on trails: Absence of a jammed phase. *Phys. Rev. Lett.* **102**, 108001 (2009).

- [13] J. Zhang, W. Klingsch, A. Schadschneider, and A. Seyfried. Ordering in bidirectional pedestrian flows and its influence on the fundamental diagram. *J. Stat. Mech.* **2012**, P02002 (2012).
- [14] D. Helbing, I. Farkas, and T. Vicsek. Simulating dynamical features of escape panic. *Nature* **407**, 487 (2000).
- [15] J. L. Silverberg, M. Bierbaum, J. P. Sethna, and I. Cohen. Collective motion of humans in mosh and circle pits at heavy metal concerts. *Phys. Rev. Lett.* **110**, 228701 (2013).
- [16] I. S. Aranson. Active colloids. *Physics-Uspekhi* **56**, 79 (2013).
- [17] R. Hunter, L. R. White, and D. Y. C. Chan. *Foundations of Colloid Science* (Clarendon Press, Oxford, 1987).
- [18] H. Berg. *E. coli in motion* (Springer Verlag, New York, 2004).
- [19] O. Reynolds. An experimental investigation of the circumstances which determine whether the motion of water shall be direct or sinuous, and of the law of resistance in parallel channels. *Phil. Trans. R. Soc. Lond.* **174**, 935 (1883).
- [20] F. Kümmel, B. ten Hagen, R. Wittkowski, D. Takagi, I. Buttinoni, R. Eichhorn, G. Volpe, H. Löwen, and C. Bechinger. Reply to Comment on "Circular motion of asymmetric self-propelling particles". *Phys. Rev. Lett.* **113**, 029802 (2014).
- [21] E. M. Purcell. Life at low Reynolds number. *Am. J. Phys.* **45**, 3 (1977).
- [22] J. E. Avron, O. Gat, and O. Kenneth. Optimal swimming at low Reynolds numbers. *Phys. Rev. Lett.* **93**, 186001 (2004).
- [23] E. Lauga and D. Bartolo. No many-scallop theorem: Collective locomotion of reciprocal swimmers. *Phys. Rev. E* **78**, 030901 (2008).
- [24] G. P. Alexander and J. M. Yeomans. Dumb-bell swimmers. *Europhys. Lett.* **83**, 34006 (2008).
- [25] A. Najafi and R. Golestanian. Simple swimmer at low Reynolds number: three linked spheres. *Phys. Rev. E* **69**, 062901 (2004).
- [26] R. Golestanian. Three-sphere low-Reynolds-number swimmer with a cargo container. *Eur. Phys. J. E* **25**, 1 (2008).
- [27] G. P. Alexander, C. M. Pooley, and J. M. Yeomans. Scattering of low-reynolds-number swimmers. *Phys. Rev. E* **78**, 045302 (2008).
- [28] E. Lauga and T. R. Powers. The hydrodynamics of swimming microorganisms. *Rep. Prog. Phys.* **72**, 096601 (2009).
- [29] V. Kantsler, J. Dunkel, M. Polin, and R. E. Goldstein. Ciliary contact interactions dominate surface scattering of swimming eukaryotes. *Proc. Natl. Acad. Sci. U.S.A.* **110**, 1187 (2013).
- [30] B. M. Friedrich, I. H. Riedel-Kruse, J. Howard, and F. Jülicher. High-precision tracking of sperm swimming fine structure provides strong test of resistive force theory. *J. Exp. Biol.* **213**, 1226 (2010).

- [31] P. Denissenko, V. Kantsler, D. J. Smith, and J. Kirkman-Brown. Human spermatozoa migration in microchannels reveals boundary-following navigation. *Proc. Natl. Acad. Sci. U.S.A.* **109**, 8007 (2012).
- [32] L. Alvarez, B. M. Friedrich, G. Gompper, and U. B. Kaupp. The computational sperm cell. *Trends in Cell Biology* **24**, 189 (2014).
- [33] R. Ma, G. S. Klindt, I. H. Riedel-Kruse, F. Jülicher, and B. M. Friedrich. Active phase and amplitude fluctuations of flagellar beating. *Phys. Rev. Lett.* **113**, 048101 (2014).
- [34] J. Yuan, D. M. Raizen, and H. H. Bau. Gait synchronization in *Caenorhabditis elegans*. *Proc. Natl. Acad. Sci. U.S.A.* **111**, 6865 (2014).
- [35] M. Polin, I. Tuval, K. Drescher, J. P. Gollub, and R. E. Goldstein. Chlamydomonas swims with two "gears" in a eukaryotic version of run-and-tumble locomotion. *Science* **325**, 487 (2009).
- [36] J. S. Guasto, K. A. Johnson, and J. P. Gollub. Oscillatory flows induced by microorganisms swimming in two dimensions. *Phys. Rev. Lett.* **105**, 168102 (2010).
- [37] R. Dreyfus, J. Baudry, M. L. Roper, M. Fermigier, H. A. Stone, and J. Bibette. Microscopic artificial swimmers. *Nature* **437**, 862 (2005).
- [38] P. Tierno, R. Golestanian, I. Pagonabarraga, and F. F. Sagues. Magnetically actuated colloidal microswimmers. *J. Phys. Chem. B* **112**, 16525 (2008).
- [39] A. Ghosh and P. Fischer. Controlled propulsion of artificial magnetic nanostructured propellers. *Nano Lett.* **9**, 2243 (2009).
- [40] P. Romanczuk, M. Bär, W. Ebeling, B. Linder, and L. Schimansky-Geier. Active Brownian particles: From individual to collective stochastic dynamics. *Eur. Phys. J. Spec. Top.* **202**, 1 (2012).
- [41] J. L. Anderson. Colloid transport by interfacial forces. *Annual Review of Fluid Mechanics* **21**, 61 (1989).
- [42] B. Sabass and U. Seifert. Dynamics and efficiency of a self-propelled, diffusiophoretic swimmer. *J. Chem. Phys.* **136**, 064508 (2012).
- [43] S. Thakur and R. Kapral. Dynamics of self-propelled nanomotors in chemically active media. *J. Chem. Phys.* **135**, (2011).
- [44] R. Golestanian, T. B. Liverpool, and A. Ajdari. Propulsion of a molecular machine by asymmetric distribution of reaction products. *Phys. Rev. Lett.* **94**, 220801 (2005).
- [45] R. Golestanian. Anomalous diffusion of symmetric and asymmetric active colloids. *Phys. Rev. Lett.* **102**, 188305 (2009).
- [46] R. Kapral. Perspective: Nanomotors without moving parts that propel themselves in solution. *J. Chem. Phys.* **138**, (2013).
- [47] S. Fournier-Bidoz, A. C. Arsenault, I. Manners, and G. A. Ozin. Synthetic self-propelled nanorotors. *Chem. Commun.* , 441 (2005).

- [48] W. F. Paxton, A. Sen, and T. Mallouk. Motility of catalytic nanoparticles through self-generated forces. *Chemistry - A European Journal* **11**, 6462 (2005).
- [49] J. R. Howse, R. A. L. Jones, A. J. Ryan, T. Gough, R. Vafabakhsh, and R. Golestanian. Self-motile colloidal particles: From directed propulsion to random walk. *Phys. Rev. Lett.* **99**, 048102 (2007).
- [50] J. Palacci, C. Cottin-Bizonne, C. Ybert, and L. Bocquet. Sedimentation and effective temperature of active colloidal suspensions. *Phys. Rev. Lett.* **105**, 088304 (2010).
- [51] W. F. Paxton, P. T. Baker, T. R. Kline, Y. Wang, T. E. Mallouk, and A. Sen. Catalytically induced electrokinetics for motors and micropumps. *J. Am. Chem. Soc.* **128**, 14881 (2006).
- [52] W. F. Paxton, K. C. Kistler, C. C. Olmeda, A. Sen, S. K. St. Angelo, Y. Cao, T. E. Mallouk, P. E. Lammert, and V. H. Crespi. Catalytic nanomotors: autonomous movement of striped nanorods. *J. Am. Chem. Soc.* **126**, 13424 (2004).
- [53] S. Ebbens, M.-H. Tu, J. R. Howse, and R. Golestanian. Size dependence of the propulsion velocity for catalytic Janus-sphere swimmers. *Phys. Rev. E* **85**, 020401 (2012).
- [54] R. Golestanian, T. B. Liverpool, and A. Ajdari. Designing phoretic micro- and nano-swimmers. *New J. Phys.* **9**, 126 (2007).
- [55] W. Gao, S. Sattayasamitsathit, J. Orozco, and J. Wang. Highly efficient catalytic micro-engines: Template electrosynthesis of polyaniline/platinum microtubes. *J. Am. Chem. Soc.* **133**, 11862 (2011).
- [56] S. Sanchez, A. A. Solovev, S. M. Harazim, and O. G. Schmidt. Microbots swimming in the flowing streams of microfluidic channels. *J. Am. Chem. Soc.* **133**, 701 (2011).
- [57] H.-R. Jiang, N. Yoshinaga, and M. Sano. Active motion of a Janus particle by self-thermophoresis in a defocused laser beam. *Phys. Rev. Lett.* **105**, 268302 (2010).
- [58] G. Volpe, I. Buttinoni, D. Vogt, H.-J. Kümmerer, and C. Bechinger. Microswimmers in patterned environments. *Soft Matter* **7**, 8810 (2011).
- [59] F. Kümmel, B. ten Hagen, R. Wittkowski, I. Buttinoni, R. Eichhorn, G. Volpe, H. Löwen, and C. Bechinger. Circular motion of asymmetric self-propelling particles. *Phys. Rev. Lett.* **110**, 198302 (2013).
- [60] R. Brown. A brief account of microscopical observations made in the months of June, July and August, 1827, on the particles contained in the pollen of plants; and on the general existence of active molecules in organic and inorganic bodies. *Philosophical Mag.* **4**, 161 (1828).
- [61] J. Ingen-Housz. *Vermischte Schriften physisch-medicinischen Inhalts* (Christian Friedrich Wappler, Wien, 1784).
- [62] C. Wiener. Erklärung des atomistischen Wesens des tropfbar flüssigen Körperzustandes und Bestätigung desselben durch die sogenannten Molekularbewegungen. *Poggendorffs Annalen* **118**, 79 (1863).

- [63] A. Einstein. Über die von der molekularkinetischen Theorie der Wärme geforderte Bewegung von in ruhenden Flüssigkeiten suspendierten Teilchen. *Annal. Phys.* **17**, 549 (1905).
- [64] A. Einstein. Zur Theorie der Brownschen Bewegung. *Annal. Phys.* **324**, 371 (1906).
- [65] M. von Smoluchowski. Zur kinetischen Theorie der Brownschen Molekularbewegung und der Suspensionen. *Annal. Phys.* **326**, 756 (1906).
- [66] P. Langevin. Sur la théorie du mouvement brownien. *C. R. Acad. Sci.* **146**, 530 (1908).
- [67] G. E. Uhlenbeck and L. S. Ornstein. On the theory of Brownian motion. *Phys. Rev.* **36**, 823 (1930).
- [68] W. Sutherland. Dynamical theory of diffusion for non-electrolytes and the molecular mass of albumin. *Phil. Mag.* **9**, 781 (1905).
- [69] S. van Teeffelen and H. Löwen. Dynamics of a Brownian circle swimmer. *Phys. Rev. E* **78**, 020101 (2008).
- [70] S. van Teeffelen, U. Zimmermann, and H. Löwen. Clockwise-directional circle swimmer moves counter-clockwise in petri dish- and ring-like confinements. *Soft Matter* **5**, 4510 (2009).
- [71] A. Sokolov and I. S. Aranson. Physical properties of collective motion in suspensions of bacteria. *Phys. Rev. Lett.* **109**, 248109 (2012).
- [72] J. Tailleur and M. E. Cates. Statistical mechanics of interacting run-and-tumble bacteria. *Phys. Rev. Lett.* **100**, 218103 (2008).
- [73] K. Drescher, J. Dunkel, L. H. Cisneros, S. Ganguly, and R. E. Goldstein. Fluid dynamics and noise in bacterial cell-cell and cell-surface scattering. *Proc. Natl. Acad. Sci. U.S.A.* **108**, 10940 (2011).
- [74] M. P. Allen and D. Tildesley. *Computer Simulation of Liquids* (Clarendon Press, Oxford, 1996).
- [75] T. Kirchhoff, H. Löwen, and R. Klein. Dynamical correlations in suspensions of charged rodlike macromolecules. *Phys. Rev. E* **53**, 5011 (1996).
- [76] H. H. Wensink, J. Dunkel, S. Heidenreich, K. Drescher, R. E. Goldstein, H. Löwen, and J. M. Yeomans. Meso-scale turbulence in living fluids. *Proc. Natl. Acad. Sci. U.S.A.* **109**, 14308 (2012).
- [77] M. M. Tirado, C. L. Martinez, and J. G. de la Torre. Comparison of theories for the translational and rotational diffusion-coefficients of rod-like macromolecules - application to short DNA fragments. *J. Chem. Phys.* **81**, 2047 (1984).
- [78] H. Löwen. Interaction between charged rodlike colloidal particles. *Phys. Rev. Lett.* **72**, 424 (1994).
- [79] H. Löwen. Charged rod-like colloidal suspensions: an "ab initio" approach. *J. Chem. Phys.* **100**, 6738 (1994).

- [80] C. Martin, B. Weyerich, J. Biegel, R. Deike, C. Johner, R. Klein, and R. Weber. Electric-field light-scattering by rod-like polyelectrolytes in aqueous suspensions. *Journal de Physique II* **5**, 697 (1995).
- [81] H. Graf and H. Löwen. Phase diagram of tobacco mosaic virus solutions. *Phys. Rev. E* **59**, 1932 (1999).
- [82] M. Hagenbüchle, B. Weyerich, M. Deggelmann, C. Graf, R. Krause, E. Maier, S. Schulz, R. Klein, and R. Weber. Static light scattering by aqueous solutions of rodlike fd-virus particles. *Phys. A.* **169**, 29 (1990).
- [83] E. Allahyarov and H. Löwen. Effective interaction between helical biomolecules. *Phys. Rev. E* **62**, 5542 (2000).
- [84] Y. Yang, V. Marceau, and G. Gompper. Swarm behavior of self-propelled rods and swimming flagella. *Phys. Rev. E* **82**, 031904 (2010).
- [85] Y. Ishimoto and N. Kikuchi. Effect of interaction shape on the condensed toroid of the semiflexible chain. *J. Chem. Phys.* **128**, 134906 (2008).
- [86] H. H. Wensink and H. Löwen. Emergent states in dense systems of active rods: from swarming to turbulence. *J. Phys. Condens. Matter* **24**, 464130 (2012).
- [87] H. H. Wensink, V. Kantsler, R. E. Goldstein, and J. Dunkel. Controlling active self-assembly through broken particle-shape symmetry. *Phys. Rev. E* **89**, 010302 (2014).
- [88] M. Abkenar, K. Marx, T. Auth, and G. Gompper. Collective behavior of penetrable self-propelled rods in two dimensions. *Phys. Rev. E* **88**, 062314 (2013).
- [89] M. Doi and S. Edwards. *The Theory of Polymer Dynamics* (Clarendon Press, Oxford, 1986).
- [90] P. G. de Gennes. *Scaling concepts in polymer physics* (Cornell University Press, Ithaca, 1979).
- [91] P. J. Flory. *Principles of Polymer Chemistry* (Cornell Univ. Press, Ithaca, 1978).
- [92] J. L. Lebowitz, J. Descloiz, A. Isihara, J. L. Jackson, and M. Fisher. Discussion of statistics of long chains with repulsive interactions. *J. Phys. Soc. Japan* **S 26**, 44 (1969).
- [93] L. Schäfer. *Excluded Volume Effects in Polymer Solutions: As Explained by the Renormalization Group* (Springer, 1999).
- [94] M. E. Cates. Diffusive transport without detailed balance in motile bacteria: does microbiology need statistical physics? *Rep. Prog. Phys.* **75**, 042601 (2012).
- [95] M. C. Marchetti, J. F. Joanny, S. Ramaswamy, T. B. Liverpool, J. Prost, M. Rao, and R. A. Simha. Hydrodynamics of soft active matter. *Rev. Mod. Phys.* **85**, 1143 (2013).
- [96] T. Vicsek and A. Zafeiris. Collective motion. *Phys. Rep.* **517**, 71 (2012).
- [97] J. Toner, Y. H. Tu, and S. Ramaswamy. Hydrodynamics and phases of flocks. *Ann. Phys.* **318**, 170 (2005).

- [98] M. F. Copeland and D. B. Weibel. Bacterial swarming: a model system for studying dynamic self-assembly. *Soft Matter* **5**, 1174 (2009).
- [99] G. Subramanian, D. L. Koch, and S. R. Fitzgibbon. The stability of a homogeneous suspension of chemotactic bacteria. *Phys. Fluids* **23**, 170 (2011).
- [100] A. Sokolov and I. S. Aranson. Reduction of viscosity in suspension of swimming bacteria. *Phys. Rev. Lett.* **103**, 148101 (2009).
- [101] M. E. Cates, D. Marenduzzo, I. Pagonabarraga, and J. Tailleur. Arrested phase separation in reproducing bacteria creates a generic route to pattern formation. *Proc. Natl. Acad. Sci. U.S.A.* **107**, 11715 (2010).
- [102] D. B. Kearns. A field guide to bacterial swarming motility. *Nat. Rev. Microbiol.* **8**, 634 (2010).
- [103] S. Ramaswamy. The mechanics and statistics of active matter. *Annu. Rev. Condens. Matter Phys.* **1**, 323 (2010).
- [104] S. Thutupalli, R. Seemann, and S. Herminghaus. Swarming behavior of simple model squirmers. *New J. Phys.* **13**, 073021 (2011).
- [105] S. R. McCandlish, A. Baskaran, and M. F. Hagan. Spontaneous segregation of self-propelled particles with different motilities. *Soft Matter* **8**, 2527 (2012).
- [106] H. C. Berg. Create life from scratch? It's a matter of time. *Phys. Today* **53**, 11 (2000).
- [107] C. Dombrowski, L. Cisneros, S. Chatkaew, R. E. Goldstein, and J. O. Kessler. Self-concentration and large-scale coherence in bacterial dynamics. *Phys. Rev. Lett.* **93**, 098103 (2004).
- [108] A. Sokolov, I. S. Aranson, J. O. Kessler, and R. E. Goldstein. Concentration dependence of the collective dynamics of swimming bacteria. *Phys. Rev. Lett.* **98**, 158102 (2007).
- [109] I. H. Riedel, K. Kruse, and J. Howard. A self-organized vortex array of hydrodynamically entrained sperm cells. *Science* **309**, 300 (2005).
- [110] D. Saintillan and M. J. Shelley. Instabilities, pattern formation, and mixing in active suspensions. *Phys. Fluids* **20**, 123304 (2008).
- [111] X. Chen, X. Dong, A. Be'er, H. L. Swinney, and H. P. Zhang. Scale-invariant correlations in dynamic bacterial clusters. *Phys. Rev. Lett.* **108**, 148101 (2012).
- [112] A. Kudrolli, G. Lumay, D. Volfson, and L. S. Tsimring. Swarming and swirling in self-propelled polar granular rods. *Phys. Rev. Lett.* **100**, 058001 (2008).
- [113] V. Schaller, C. Weber, C. Semmrich, E. Frey, and A. R. Bausch. Polar patterns of driven filaments. *Nature* **467**, 73 (2010).
- [114] A. Czirók, E. Ben-Jacob, I. Cohen, and T. Vicsek. Formation of complex bacterial colonies via self-generated vortices. *Phys. Rev. E* **54**, 1791 (1996).
- [115] T. Vicsek, A. Czirók, E. Ben-Jacob, I. Cohen, and O. Shochet. Novel type of phase transition in a system of self-driven particles. *Phys. Rev. Lett.* **75**, 1226 (1995).

- [116] G. Miño, T. E. Mallouk, T. Darnige, M. Hoyos, J. Dauchet, J. Dunstan, R. Soto, Y. Wang, A. Rousselet, and E. Clement. Enhanced diffusion due to active swimmers at a solid surface. *Phys. Rev. Lett.* **106**, 048102 (2011).
- [117] T. Ishikawa, N. Yoshida, H. Ueno, M. Wiedeman, Y. Imai, and T. Yamaguchi. Energy transport in a concentrated suspension of bacteria. *Phys. Rev. Lett.* **107**, 028102 (2011).
- [118] F. G. Woodhouse and R. E. Goldstein. Spontaneous circulation of confined active suspensions. *Phys. Rev. Lett.* **109**, 168105 (2012).
- [119] J. Schwarz-Linek, C. Valeriani, A. Cacciuto, M. E. Cates, D. Marenduzzo, A. N. Morozov, and W. C. K. Poon. Phase separation and rotor self-assembly in active particle suspensions. *Proc. Natl. Acad. Sci. U.S.A.* **109**, 4052 (2012).
- [120] D. Volfson, A. Kudrolli, and L. S. Tsimring. Anisotropy-driven dynamics in vibrated granular rods. *Phys. Rev. E* **70**, 051312 (2004).
- [121] V. Narayan, S. Ramaswamy, and N. Menon. Long-lived giant number fluctuations in a swarming granular nematic. *Science* **317**, 5834 (2007).
- [122] M. Garcia, S. Berti, P. Peyla, and S. Rafai. Random walk of a swimmer in a low-Reynolds-number medium. *Phys. Rev. E* **83**, 035301 (2011).
- [123] A. Erbe, M. Zientara, L. Baraban, C. Kreidler, and P. Leiderer. Various driving mechanisms for generating motion of colloidal particles. *J. Phys. Condens. Matter* **20**, 404215 (2008).
- [124] I. Buttinoni, G. Volpe, F. Kümmel, G. Volpe, and C. Bechinger. Active Brownian motion tunable by light. *J. Phys. Condens. Matter* **24**, 284129 (2012).
- [125] A. Snezhko, M. Belkin, I. S. Aranson, and W.-K. Kwok. Self-assembled magnetic surface swimmers. *Phys. Rev. Lett.* **102**, 118103 (2009).
- [126] A. Snezhko and I. S. Aranson. Magnetic manipulation of self-assembled colloidal asters. *Nature Mat.* **10**, 698 (2011).
- [127] G. Rückner and R. Kapral. Chemically powered nanodimers. *Phys. Rev. Lett.* **98**, 150603 (2007).
- [128] M. N. Popescu, S. Dietrich, and G. Oshanin. Confinement effects on diffusiophoretic self-propellers. *J. Chem. Phys.* **130**, 194702 (2009).
- [129] F. Peruani, A. Deutsch, and M. Bär. Nonequilibrium clustering of self-propelled rods. *Phys. Rev. E* **74**, 030904 (2006).
- [130] H. H. Wensink and H. Löwen. Aggregation of self-propelled colloidal rods near confining walls. *Phys. Rev. E* **78**, 031409 (2008).
- [131] F. Ginelli, F. Peruani, M. Bär, and H. Chaté. Large-scale collective properties of self-propelled rods. *Phys. Rev. Lett.* **104**, 184502 (2010).
- [132] N. Sambelashvili, A. W. C. Lau, and D. Cai. Dynamics of bacterial flow: Emergence of spatiotemporal coherent structures. *Phys. Lett. A* **360**, 507 (2007).

- [133] A. M. Menzel. Collective motion of binary self-propelled particle mixtures. *Phys. Rev. E* **85**, 021912 (2012).
- [134] H. C. Berg and L. Turner. Chemotaxis of bacteria in glass capillary arrays. *Escherichia coli*, motility, microchannel plate, and light scattering. *Biophys. J.* **58**, 919 (1990).
- [135] W. R. DiLuzio, L. Turner, M. Mayer, P. Garstecki, D. B. Weibel, H. C. Berg, and G. M. Whitesides. *Escherichia coli* swim on the right-hand side. *Nature* **435**, 1271 (2005).
- [136] E. Lauga, W. R. DiLuzio, G. M. Whitesides, and H. A. Stone. Swimming in circles: Motion of bacteria near solid boundaries. *Biophys. J.* **90**, 400 (2006).
- [137] J. Hill, O. Kalkanci, J. L. McMurry, and H. Koser. Hydrodynamic surface interactions enable *Escherichia Coli* to seek efficient routes to swim upstream. *Phys. Rev. Lett.* **98**, 068101 (2007).
- [138] V. B. Shenoy, D. T. Tambe, A. Prasad, and J. A. Theriot. A kinematic description of the trajectories of *listeria monocytogenes* propelled by actin comet tails. *Proc. Natl. Acad. Sci. U.S.A.* **104**, 8229 (2007).
- [139] S. Schmidt, J. van der Gucht, P. M. Biesheuvel, R. Weinkamer, E. Helffer, and A. Frey. Non-Gaussian curvature distribution of actin-propelled biomimetic colloid trajectories. *Europ. Biophys. J.* **37**, 1361 (2008).
- [140] S. B. Babu and H. Stark. Modeling the locomotion of the african trypanosome using multi-particle collision dynamics. *New J. Phys.* **14**, 085012 (2012).
- [141] Y. Sumino, K. H. Nagai, Y. Shitaka, D. Tanaka, K. Yoshikawa, H. Chaté, and K. Oiwa. Large-scale vortex lattice emerging from collectively moving microtubules. *Nature* **48**, 448 (2012).
- [142] D. M. Woolley. Motility of spermatozoa at surfaces. *Reproduction* **216**, 259 (2003).
- [143] B. M. Friedrich and F. Jülicher. The stochastic dance of circling sperm cells: sperm chemotaxis in the plane. *New J. Phys.* **10**, 123035 (2008).
- [144] R. Mach and F. Schweitzer. Modeling vortex swarming in daphnia. *Bull. Math. Biol.* **69**, 539 (2007).
- [145] S. Nakata, Y. Iguchi, S. Ose, M. Kuboyama, T. Ishii, and K. Yoshikawa. Self-rotation of a camphor scraping on water: New insight into the old problem. *Langmuir* **13**, 4454 (1997).
- [146] T. Ohta and T. Ohkuma. Deformable self-propelled particles. *Phys. Rev. Lett.* **102**, 154101 (2009).
- [147] A. Reinmüller, H. J. Schöpe, and T. Palberg. Emergent self-propulsion at low Reynolds number. *Langmuir* **29**, 1738 (2013).
- [148] B. ten Hagen, S. van Teeffelen, and H. Löwen. Brownian motion of a self-propelled particle. *J. Phys. Condens. Matter* **23**, 194119 (2011).
- [149] P. K. Radtke and L. Schimansky-Geier. Directed transport of confined Brownian particles with torque. *Phys. Rev. E* **85**, 051110 (2012).

- [150] M. Tarama and T. Ohta. Spinning motion of a deformable self-propelled particle in two dimensions. *J. Phys. Condens. Matter* **24**, 464129 (2012).
- [151] J. Dunstan, G. Miño, E. Clement, and R. Soto. A two-sphere model for bacteria swimming near solid surfaces. *Phys. Fluids* **24**, 011901 (2012).
- [152] R. Ledesma-Aguilar, H. Löwen, and J. M. Yeomans. A circle swimmer at low Reynolds number. *Eur. Phys. J. E* **35**, 9746 (2012).
- [153] T. Si. The equation of motion for the trajectory of a circling particle with an overdamped circle center. *Phys. A* **391**, 3054 (2012).
- [154] R. Kirchhoff and H. Löwen. T-structured fluid and jamming in driven Brownian rotators. *Europhys. Lett.* **96**, 291 (2005).
- [155] R. Kirchhoff and H. Löwen. Tracer diffusion and cluster formation in mixtures of spheres and rotating rods. *J. Phys. Condens. Matter* **17**, 7805 (2005).
- [156] M. Sullivan, K. Zhao, C. Harrison, R. H. Austin, M. Megens, A. Hollingsworth, W. B. Russel, Z. Cheng, T. Mason, and P. M. Chaikin. Control of colloids with gravity, temperature gradients, and electric fields. *J. Phys. Condens. Matter* **15**, S11 (2003).
- [157] Z. Cheng, P. M. Chaikin, and T. G. Mason. Light streak tracking of optically trapped thin microdisks. *Phys. Rev. Lett.* **89**, 108303 (2002).
- [158] A. I. Bishop, T. A. Nieminen, N. R. Heckenberg, and H. Rubinsztein-Dunlop. Optical application and measurement of torque on microparticles of isotropic nonabsorbing material. *Phys. Rev. A* **68**, 033802 (2003).
- [159] Y. Fily, A. Baskaran, and M. C. Marchetti. Cooperative self-propulsion of active and passive rotors. *Soft Matter* **8**, 3002 (2012).
- [160] L. H. Cisneros, R. Cortez, C. Dombrowski, R. E. Goldstein, and J. O. Kessler. Fluid dynamics of self-propelled microorganisms, from individuals to concentrated populations. *Phys. Fluids* **43**, 737 (2007).
- [161] C. W. Wolgemuth. Collective swimming and the dynamics of bacterial turbulence. *Biophys. J.* **95**, 1564 (2008).
- [162] M. Marechal, R. J. Kortschot, A. F. Demirörs, A. Imhof, and M. Dijkstra. Phase behavior and structure of a new colloidal model system of bowl-shaped particles. *Nano Lett.* **10**, 1907 (2010).
- [163] R. Wittkowski and H. Löwen. Self-propelled Brownian spinning top: Dynamics of a biaxial swimmer at low Reynolds numbers. *Phys. Rev. E* **85**, 021406 (2012).
- [164] M. Rex, H. H. Wensink, and H. Löwen. Dynamical density functional theory for anisotropic colloidal particles. *Phys. Rev. E* **76**, 021403 (2007).
- [165] R. Wittkowski and H. Löwen. Dynamical density functional theory for colloidal particles with arbitrary shape. *Mol. Phys.* **109**, 2935 (2011).
- [166] W. Radcliffe. *Fishing from the Earliest Times* (John Murray, London, 1926).

- [167] X. Garcia, S. Rapaia, and P. Peyla. Light control of the flow of phototactic microswimmer suspensions. *Phys. Rev. Lett.* **110**, 138106 (2013).
- [168] B. Kaehr and J. B. Shear. High-throughput design of microfluidics based on directed bacterial motility. *Lab Chip* **9**, 2632 (2009).
- [169] J. Palacci, S. Sacanna, A. P. Steinberg, D. J. Pine, and P. M. Chaikin. Living crystals of light-activated colloidal surfers. *Science* **339**, 936 (2013).
- [170] O. Raz and A. M. Leshansky. Efficiency of cargo towing by a microswimmer. *Phys. Rev. E* **77**, 055305 (2008).
- [171] W. Gao, D. Kagan, O. S. Pak, C. Clawson, S. Campuzano, E. Chuluun-Erdene, E. Ship-ton, E. E. Fullerton, L. Zhang, E. Lauga, and J. Wang. Cargo-towing fuel-free magnetic nanoswimmers for targeted drug delivery. *Small* **8**, 460 (2011).
- [172] L. Baraban, M. Tasinkevych, M. N. Popescu, S. Sanchez, S. Dietrich, and O. G. Schmidt. Transport of cargo by catalytic Janus micro-motors. *Soft Matter* **8**, 48 (2012).
- [173] M. N. Popescu, M. Tasinkevych, and S. Dietrich. Pulling and pushing a cargo with a catalytically active carrier. *Europhys. Lett.* **95**, 28004 (2011).
- [174] L. Angelani and R. D. Leonardo. Geometrically biased random walks in bacteria-driven micro-shuttles. *New J. Phys.* **12**, 113017 (2010).
- [175] E. C. Redmond and C. J. Griffith. Consumer food handling in the home: A review of food safety studies. *J. Food Protection* **66**, 130 (2003).
- [176] J. Taylor, K. Lai, M. Davies, D. Clifton, I. Ridley, and P. Biddulph. Flood management: Prediction of microbial contamination in large-scale floods in urban environments. *Environ. Int.* **37**, 1019 (2011).
- [177] B. ten Hagen, R. Wittkowski, and H. Löwen. Brownian dynamics of a self-propelled particle in shear flow. *Phys. Rev. E* **84**, 031105 (2011).
- [178] M. Grzelczak, J. Vermant, E. M. Furst, and L. M. Liz-Marzán. Directed self-assembly of nanoparticles. *ACS Nano* **4**, 3591 (2010).
- [179] P. Galajda, J. Keymer, P. Chaikin, and R. Austin. A wall of funnels concentrates swimming bacteria. *J. Bacteriol.* **189**, 8704 (2007).
- [180] J. Tailleur and M. E. Cates. Sedimentation, trapping, and rectification of dilute bacteria. *Europhys. Lett.* **86**, 60002 (2009).
- [181] M. B. Wan, C. J. Olson Reichhardt, Z. Nussinov, and C. Reichhardt. Rectification of swimming bacteria and self-driven particle systems by arrays of asymmetric barriers. *Phys. Rev. Lett.* **101**, 018102 (2008).
- [182] J. A. Drocco, C. J. Olson Reichhardt, and C. Reichhardt. Bidirectional sorting of flocking particles in the presence of asymmetric barriers. *Phys. Rev. E* **85**, 056102 (2012).
- [183] M.-B. Wan and Y. Jho. Directed motion of elongated active polymers. *Soft Matter* **9**, 3255 (2013).

- [184] P. K. Ghosh, V. R. Misko, F. Marchesoni, and F. Nori. Self-propelled Janus particles in a ratchet: Numerical simulations. *Phys. Rev. Lett.* **110**, 268301 (2013).
- [185] A. Guidobaldi, Y. Jeyaram, I. Berdakin, V. V. Moshchalkov, C. A. Condat, V. I. Marconi, L. Giojalas, and A. V. Silhanek. Geometrical guidance and trapping transition of human sperm cells. *Phys. Rev. E* **89**, 032720 (2014).
- [186] L. Restrepo-Pérez, L. Soler, C. Martínez-Cisneros, S. Sanchez, and O. G. Schmidt. Trapping self-propelled micromotors with microfabricated chevron and heart-shaped chips. *Lab Chip* **14**, 1515 (2014).
- [187] O. Chepizhko and F. Peruani. Diffusion, subdiffusion, and trapping of active particles in heterogeneous media. *Phys. Rev. Lett.* **111**, 160604 (2013).
- [188] R. DiLeonardo, L. Angelani, D. DellArciprete, G. Ruocco, V. Iebba, S. Schippa, M. P. Conte, F. Mecarini, F. D. Angelis, and E. D. Fabrizio. Bacterial ratchet motors. *Proc. Natl. Acad. Sci. U.S.A.* **107**, 9541 (2010).
- [189] A. Sokolov, M. M. Apodaca, B. A. Grzybowski, and I. S. Aranson. Swimming bacteria power microscopic gears. *Proc. Natl. Acad. Sci. U.S.A.* **107**, 969 (2010).
- [190] I. S. Aranson and L. S. Tsimring. Patterns and collective behavior in granular media: Theoretical concepts. *Rev. Mod. Phys.* **78**, 641 (2006).
- [191] D. L. Englert, M. D. Manson, and A. Jayaraman. Investigation of bacterial chemotaxis in flow-based microfluidic devices. *Nature Protocols* **5**, 864 (2010).
- [192] G. V. Kolmakov, A. Schaefer, I. Aranson, and A. C. Balazs. Designing mechano-responsive microcapsules that undergo self-propelled motion. *Soft Matter* **8**, 180 (2012).
- [193] H. Löwen and G. P. Hoffmann. Melting of polydisperse colloidal crystals in nonequilibrium. *Phys. Rev. E* **60**, 3009 (1999).
- [194] V. Narayan, S. Ramaswamy, and N. Menon. Long-lived giant number fluctuations in a swarming granular nematic. *Science* **317**, 105 (2007).
- [195] E. S. Muthukumar. Screening of hydrodynamic interaction in a solution of rodlike macromolecules. *Macromolecules* **16**, 1475 (1983).
- [196] C. Reichhardt and C. J. O. Reichhardt. Dynamics and separation of circularly moving particles in asymmetrically patterned arrays. *Phys. Rev. E* **88**, 042306 (2013).
- [197] M. Mijalkov and G. Volpe. Sorting of chiral microswimmers. *Soft Matter* **9**, 6376 (2013).
- [198] T. Ishikawa and T. J. Pedley. Coherent structures in monolayers of swimming particles. *Phys. Rev. Lett.* **100**, 088103 (2008).
- [199] M. T. Downton and H. Stark. Simulation of a model microswimmer. *J. Phys. Condens. Matter* **20**, 204101 (2009).
- [200] I. O. Götze and G. Gompper. Mesoscale simulations of hydrodynamic squirmer interactions. *Phys. Rev. E* **82**, 041921 (2010).

- [201] J. K. G. Dhont. *An Introduction to the Dynamics of Colloids* (Elsevier, Amsterdam, 1996).
- [202] L. Cisneros, C. Dombrowski, R. E. Goldstein, and J. O. Kessler. Reversal of bacterial locomotion at an obstacle. *Phys. Rev. E* **73**, 030901 (2006).
- [203] F. D. C. Farrell, M. C. Marchetti, D. Marenduzzo, and J. Tailleur. Pattern formation in self-propelled particles with density-dependent motility. *Phys. Rev. Lett.* **108**, 248101 (2012).
- [204] O. J. Dammone, I. Zacharoudiou, R. P. A. Dullens, J. M. Yeomans, M. P. Lettinga, and D. G. A. L. Aarts. Confinement induced splay-to-bend transition of colloidal rods. *Phys. Rev. Lett.* **109**, 108303 (2012).
- [205] N. M. Silvestre, Z. Eskandari, P. Patrício, J. M. Romero-Enrique, and M. M. Telo da Gama. Nematic wetting and filling of crenellated surfaces. *Phys. Rev. E* **86**, 011703 (2012).
- [206] A. O. Parry, C. Rascón, E. A. G. Jamie, and D. G. A. L. Aarts. Capillary emptying and short-range wetting. *Phys. Rev. Lett.* **108**, 246101 (2012).
- [207] H. Zhang, A. Be'er, R. Smith, E.-L. Florin, and H. Swinney. Swarming dynamics in bacterial colonies. *Europhys. Lett.* **7**, 48011 (2009).
- [208] K.-A. Liu and L. I. Bacterial turbulence reduction by passive magnetic particle chains. *Phys. Rev. E* **88**, 033004 (2013).
- [209] I. Aranson. The aquatic dance of bacteria. *Physics* **6**, 61 (2013).
- [210] H. Wioland, F. G. Woodhouse, J. Dunkel, J. O. Kessler, and R. E. Goldstein. Confinement stabilizes a bacterial suspension into a spiral vortex. *Phys. Rev. Lett.* **110**, 268102 (2013).
- [211] S. Zhou, A. Sokolov, O. D. Lavrentovich, and I. S. Aranson. Living liquid crystals. *Proc. Natl. Acad. Sci. U.S.A.* **111**, 1265 (2014).
- [212] L. Angelani, R. DiLeonardo, and G. Ruocco. Self-starting micromotors in a bacterial bath. *Phys. Rev. Lett.* **102**, 048104 (2009).
- [213] D. Wong, E. E. Beattie, E. B. Steager, and V. Kumar. Effect of surface interactions and geometry on the motion of micro bio robots. *Appl. Phys. Lett.* **103**, (2013).
- [214] H. Li and H. P. Zhang. Asymmetric gear rectifies random robot motion. *Europhys. Lett.* **102**, 50007 (2013).
- [215] G. Li and J. X. Tang. Accumulation of microswimmers near a surface mediated by collision and rotational Brownian motion. *Phys. Rev. Lett.* **103**, 078101 (2009).
- [216] E. Calzavarini, M. Cencini, D. Lohse, and F. Toschi. Quantifying turbulence-induced segregation of inertial particles. *Phys. Rev. Lett.* **101**, 084504 (2008).
- [217] J. Gachelin, G. Miño, H. Berthet, A. Lindner, A. Rousselet, and E. Clément. Non-newtonian viscosity of *Escherichia coli* suspensions. *Phys. Rev. Lett.* **110**, 268103 (2013).

- [218] A. Sokolov, R. E. Goldstein, F. I. Feldchtein, and I. S. Aranson. Enhanced mixing and spatial instability in concentrated bacterial suspensions. *Phys. Rev. E* **80**, 031903 (2009).
- [219] I. S. Aranson, A. Sokolov, J. O. Kessler, and R. E. Goldstein. Model for dynamical coherence in thin films of self-propelled microorganisms. *Phys. Rev. E* **75**, 040901 (2007).
- [220] J. Garcia de la Torre, S. Navarro, M. C. Lopez Martinez, F. G. Diaz, and J. J. Lopez Cascales. Hydro: a computer program for the prediction of hydrodynamic properties of macromolecules. *Biophys. J.* **67**, 530 (1994).
- [221] B. Carrasco and J. Garcia de la Torre. Improved hydrodynamic interaction in macromolecular bead models. *J. Chem. Phys.* **111**, 4817 (1999).
- [222] I. S. M. Khalil, H. C. Dijkslag, L. Abelmann, and S. Misra. Magnetosperm: A micro-robot that navigates using weak magnetic fields. *Appl. Phys. Lett.* **104**, (2014).
- [223] S. Thakur and R. Kapral. Self-propelled nanodimer bound state pairs. *J. Chem. Phys.* **133**, 204505 (2010).
- [224] J. Palacci, S. Sacanna, A. Vatchinsky, P. M. Chaikin, and D. J. Pine. Photoactivated colloidal dockers for cargo transportation. *J. Am. Chem. Soc.* **135**, 15978 (2013).
- [225] A. Bricard, J.-B. Caussin, N. Desreumaux, O. Dauchot, and D. Bartolo. Emergence of macroscopic directed motion in populations of motile colloids. *Nature* **503**, 95 (2013).
- [226] A. M. Menzel and T. Ohta. Soft deformable self-propelled particles. *Europhys. Lett.* **99**, 58001 (2012).
- [227] J. Gachelin, A. Rousselet, A. Lindner, and E. Clement. Collective motion in an active suspension of *Escherichia coli* bacteria. *New J. Phys.* **16**, 025003 (2014).
- [228] J. A. Cohen and R. Golestanian. Emergent cometlike swarming of optically driven thermally active colloids. *Phys. Rev. Lett.* **112**, 068302 (2014).
- [229] I. Buttinoni, J. Bialké, F. Kümmel, H. Löwen, C. Bechinger, and T. Speck. Dynamical clustering and phase separation in suspensions of self-propelled colloidal particles. *Phys. Rev. Lett.* **110**, 238301 (2013).
- [230] G. S. Redner, M. F. Hagan, and A. Baskaran. Structure and dynamics of a phase-separating active colloidal fluid. *Phys. Rev. Lett.* **110**, 055701 (2013).
- [231] Y. Fily and M. C. Marchetti. Athermal phase separation of self-propelled particles with no alignment. *Phys. Rev. Lett.* **108**, 235702 (2012).
- [232] A. Zöttl and H. Stark. Hydrodynamics determines collective motion and phase behavior of active colloids in quasi-two-dimensional confinement. *Phys. Rev. Lett.* **112**, 118101 (2014).
- [233] S. K. Das, S. A. Egorov, B. Trefz, P. Virnau, and K. Binder. Phase behavior of active swimmers in depletants: Molecular dynamics and integral equation theory. *Phys. Rev. Lett.* **112**, 198301 (2014).

- [234] E. Lushi, H. Wioland, and R. E. Goldstein. Fluid flows created by swimming bacteria drive self-organization in confined suspensions. *Proc. Natl. Acad. Sci. U.S.A.* , 201405698 (2014).
- [235] I. Berdakin, Y. Jeyaram, V. V. Moshchalkov, L. Venken, S. Dierckx, S. J. Vanderleyden, A. V. Silhanek, C. A. Condat, and V. I. Marconi. Influence of swimming strategy on microorganism separation by asymmetric obstacles. *Phys. Rev. E* **87**, 052702 (2013).
- [236] J. Elgeti and G. Gompper. Wall accumulation of self-propelled spheres. *Europhys. Lett.* **101**, 48003 (2013).
- [237] A. Costanzo, R. Di Leonardo, G. Ruocco, and L. Angelani. Transport of self-propelling bacteria in micro-channel flow. *J. Phys. Condens. Matter* **24**, 065101 (2012).
- [238] C. F. Lee. Active particles under confinement: aggregation at the wall and gradient formation inside a channel. *New J. Phys.* **15**, 055007 (2013).
- [239] Y. Fily, A. Baskaran, and M. F. Hagan. Dynamics of self-propelled particles under strong confinement. *Soft Matter* **10**, 5609 (2014).
- [240] J. C. F. Schulz, L. Schmidt, R. B. Best, J. Dzubiella, and R. R. Netz. Peptide chain dynamics in light and heavy water: Zooming in on internal friction. *J. Am. Chem. Soc.* **134**, 6273 (2012).
- [241] R. G. Winkler. Semiflexible polymers in shear flow. *Phys. Rev. Lett.* **97**, 128301 (2006).
- [242] S. Liu, B. Ashok, and M. Muthukumar. Brownian dynamics simulations of bead-rod-chain in simple shear flow and elongational flow. *Polymer* **45**, 1383 (2004).
- [243] L. Cannavacciuolo, R. G. Winkler, and G. Gompper. Mesoscale simulations of polymer dynamics in microchannel flows. *Europhys. Lett.* **83**, 34007 (2008).
- [244] R. Ledesma-Aguilar and J. M. Yeomans. Enhanced motility of a microswimmer in rigid and elastic confinement. *Phys. Rev. Lett.* **111**, 138101 (2013).
- [245] S. Kjelleberg, B. A. Humphrey, and K. C. Marshall. Effect of interfaces on small, starved marine bacteria. *Appl. Environ. Microbiol.* **43**, 1166 (1982).
- [246] W. G. Pitt, M. O. McBride, A. J. Barton, and R. D. Sagers. Air-water interface displaces adsorbed bacteria. *Biomaterials* **14**, 605 (1993).
- [247] C. Gómez-Suárez, H. J. Busscher, and H. C. van der Mei. Analysis of bacterial detachment from substratum surfaces by the passage of air-liquid interfaces. *Appl. Environ. Microbiol.* **67**, 2531 (2001).
- [248] D. K. Powelson and A. L. Mills. Bacterial enrichment at the gas-water interface of a laboratory apparatus. *Appl. Environ. Microbiol.* **62**, 2593 (1996).
- [249] C. Meel, N. Kouzel, E. R. Oldewurtel, and B. Maier. Three-dimensional obstacles for bacterial surface motility. *Small* **8**, 530 (2012).
- [250] A. Shklarsh, A. Finkelshtein, G. Ariel, O. Kalisman, C. Ingham, and E. Ben-Jacob. Collective navigation of cargo-carrying swarms. *Interface Focus* **2**, 689 (2012).

- [251] S. Sacanna, W. T. M. Irvine, P. M. Chaikin, and D. J. Pine. Lock and key colloids. *Nature* **464**, 575 (2010).
- [252] W. Wang, W. Duan, A. Sen, and T. E. Mallouk. Catalytically powered dynamic assembly of rod-shaped nanomotors and passive tracer particles. *Proc. Natl. Acad. Sci. U.S.A.* **110**, 17744 (2013).
- [253] D. Wu, K. Hui, and D. Chandler. Monte Carlo study of polymers in equilibrium with random obstacles. *J. Chem. Phys.* **96**, 835 (1992).
- [254] K. Leung and D. Chandler. Statistics of simple chains in a sea of blockers. *J. Chem. Phys.* **102**, 1405 (1995).
- [255] K. Kremer and G. S. Grest. Dynamics of entangled linear polymer melts: a molecular dynamics simulation. *J. Chem. Phys.* **92**, 5057 (1990).
- [256] J. Bialké, T. Speck, and H. Löwen. Crystallization in a dense suspension of self-propelled particles. *Phys. Rev. Lett.* **108**, 168301 (2012).
- [257] J.-L. Barrat and F. Joanny. *Theory of Polyelectrolyte Solutions*, pages 1–66. John Wiley & Sons, Inc., (2007).
- [258] M. Hinczewski, X. Schlagberger, M. Rubinstein, O. Krichevsky, and R. R. Netz. End-monomer dynamics in semiflexible polymers. *Macromolecules* **42**, 860 (2009).
- [259] K. C. Leptos, J. S. Guasto, J. P. Gollub, A. I. Pesci, and R. E. Goldstein. Dynamics of enhanced tracer diffusion in suspensions of swimming eukaryotic microorganisms. *Phys. Rev. Lett.* **103**, 198103 (2009).
- [260] G. Miño, J. Dunstan, A. Rousselet, E. Clement, and R. Soto. Induced diffusion of tracers in a bacterial suspension: theory and experiments. *J. Fluid Mech.* **729**, 423 (2013).
- [261] X.-L. Wu and A. Libchaber. Particle diffusion in a quasi-two-dimensional bacterial bath. *Phys. Rev. Lett.* **84**, 3017 (2000).
- [262] J. Deseigne, O. Dauchot, and H. Chaté. Collective motion of vibrated polar disks. *Phys. Rev. Lett.* **105**, 098001 (2010).
- [263] I. Theurkauff, C. Cottin-Bizonne, J. Palacci, C. Ybert, and L. Bocquet. Dynamic clustering in active colloidal suspensions with chemical signaling. *Phys. Rev. Lett.* **108**, 268303 (2012).
- [264] J. Bialké, H. Löwen, and T. Speck. Microscopic theory for the phase separation of self-propelled repulsive disks. *Europhys. Lett.* **103**, 30008 (2013).
- [265] H. Sillescu. Heterogeneity at the glass transition: a review. *J. Non-Cryst. Solids* **243**, 81 (1999).
- [266] Y. Yang, F. Qiu, and G. Gompper. Self-organized vortices of circling self-propelled particles and curved active flagella. *Phys. Rev. E* **89**, 012720 (2014).
- [267] N. H. P. Nguyen, D. Klotsa, M. Engel, and S. C. Glotzer. Emergent collective phenomena in a mixture of hard shapes through active rotation. *Phys. Rev. Lett.* **112**, 075701 (2014).

- [268] M. P. Magiera and L. Brendel. Trapping of photophoretic particles. arXiv , 1407.0983 (2014).
- [269] C. Reichhardt and C. J. O. Reichhardt. Active matter ratchets with an external drift. Phys. Rev. E **88**, 062310 (2013).
- [270] G. Volpe, S. Gigan, and G. Volpe. Simulation of the active Brownian motion of a microswimmer. Am. J. Phys. **82**, 659 (2014).
- [271] F. Q. Potiguar, G. A. Farias, and W. P. Ferreira. Self-propelled particle transport in regular arrays of rigid asymmetric obstacles. Phys. Rev. E **90**, 012307 (2014).
- [272] S. A. Mallory, C. Valeriani, and A. Cacciuto. Curvature induced activation of a passive tracer in an active bath. arXiv , 1407.3418 (2014).
- [273] R. Großmann, P. Romanczuk, M. Bär, and L. Schimansky-Geier. Vortex arrays and meso-scale turbulence of self-propelled particles. arXiv , 1404.7111 (2014).
- [274] B. ten Hagen, S. van Teeffelen, and H. Löwen. Non-Gaussian behaviour of a self-propelled particle on a substrate. Condens. Matter Phys. **12**, 725 (2009).

Eidesstattliche Versicherung

Ich versichere an Eides Statt, dass die Dissertation von mir selbständig und ohne unzulässige fremde Hilfe unter Beachtung der „Grundsätze zur Sicherung guter wissenschaftlicher Praxis an der Heinrich-Heine-Universität Düsseldorf“ erstellt worden ist.

Düsseldorf,